



---

# SCANNING TUNNELING MICROSCOPY STUDY OF IRON OXIDE BASED MODEL CATALYSTS

vorgelegt von

**MIKOŁAJ LEWANDOWSKI**

geboren am 01.02.1983 in Poznań, Polen

Von der Fakultät III – Prozesswissenschaften  
Technischen Universität Berlin

zur Erlangung des akademischen Grades

**Doktor der Ingenieurwissenschaften**

**Dr.-Ing.**

im Fach Werkstoffwissenschaften

**genehmigte Dissertation**

**Promotionsausschuss:**

Vorsitzender: Prof. Dr. rer. nat. Lothar Kroh

Gutachter: Prof. Dr. rer. nat. Hans-Joachim Freund

Gutachter: Prof. Dr. rer. nat. Helmut Schubert

Tag der wissenschaftlichen Aussprache: 23.08.2011

Berlin 2011

D 83

Diese Arbeit wurde im Zeitraum von September 2007 bis Dezember 2010 am Fritz-Haber-Institut der Max-Planck-Gesellschaft, Berlin, Deutschland, Abteilung Chemische Physik, unter der Leitung von Herrn Prof. Hans-Joachim Freund angefertigt.

**DEDICATED TO MY BELOVED WIFE AGATA**

# Acknowledgments

I would like to thank

**Prof. Hans-Joachim Freund**, my supervisor, for giving me a PhD position in his laboratory, thus creating an opportunity to work with best of the best scientists on state-of-the-art equipment. I greatly appreciate his supervision and trust.

**Prof. Helmut Schubert** from Technische Universität Berlin for kindly agreeing to be the co-supervisor and reviewing my thesis.

**Prof. Lothar Kroh** from Technische Universität Berlin for kindly agreeing to be the chairman of the defense examination committee.

**Prof. Ernst Bauer**: I am proud that I had the opportunity to work with Prof. Bauer on his Humboldt Research Award 2008 project. I would also like to express my gratitude for his comments on the  $\text{Fe}_2\text{O}_3$  part of my PhD thesis.

**Dr. Shamil Shaikhutdinov**, my group leader and scientific advisor, for accepting me as a member of “Structure and Reactivity” research group, giving an interesting research topic and the years of successful cooperation. I am also very grateful for his valuable comments on my PhD thesis.

**Max-Planck-Gesellschaft** (Stipendium).

**My co-workers**, especially **Dr. Zihui Qin**, **Yingna Sun** and **Dr. Irene M. N. Groot**.

“**Structure and Reactivity**” research group.

**Dr. Livia Giordano** from the group of **Prof. Gianfranco Pacchioni** and **Dr. Jacek Goniakowski** from the group of **Prof. Claudine Noguera** for theoretical DFT calculations.

**Björn Pieper** and **Wiebke Ludwig** for help in title and abstract translation from English to German.

**Manuela Misch** and **Gabriele Mehnert** for administrative work.

**Klaus Peter Vogelgesang**, **Uwe Härtel** and **Walter Wachsmann** for interesting discussions and technical support.

**BESSY-II** team.

My **Office-Mates**.

**Friends** at Fritz-Haber-Institut der Max-Planck-Gesellschaft, Berlin.

**FHI football** group.

My **Family**, especially my **Parents**, **Sister**, **Brother**, my beloved **Wife** and **Daughter** - for their love and support.

My **Aunt Brygida** for all the help.

# Abstract

## Scanning Tunneling Microscopy study of iron oxide based model catalysts

Iron oxide films, such as FeO(111), Fe<sub>3</sub>O<sub>4</sub>(111) and  $\alpha$ -Fe<sub>2</sub>O<sub>3</sub>(0001) grown on Pt(111), have been shown as suitable systems for modeling iron oxide based catalysts. In this work we studied the morphology of iron oxide films as well as nucleation, growth and thermal stability of Pt and Au nanoparticles supported on these films. In particular, the studies are focused on deeper understanding of structure-reactivity relationships for these systems in low temperature CO oxidation reaction in the mbar pressure range. Structural characterization was performed using primarily Scanning Tunneling Microscopy (STM) in combination with Low Energy Electron Diffraction (LEED), Auger Electron Spectroscopy (AES) and Temperature Programmed Desorption (TPD).

On Fe<sub>3</sub>O<sub>4</sub>(111) films Pt nucleates randomly forming 2-dimensional islands which coalesce with increasing coverage. These islands seem to adopt to the structure of the supporting oxide which strongly influence their CO adsorption capabilities. Annealing in UHV causes particles sintering and formation of well-faceted 3-dimensional particles. We show that high temperature treatments under reducing conditions lead to encapsulation of Pt particles by an iron oxide film as a result of the so-called Strong Metal-Support Interaction (SMSI). Atomic resolution STM images revealed that the encapsulating layer is a monolayer FeO(111) film in nature.

For ultrathin FeO(111) films on Pt(111), which were found to exhibit greatly enhanced reactivity in the CO oxidation reaction, we provide STM evidence for oxygen induced transformation of the bilayer O-Fe film into the catalytically active, trilayer O-Fe-O film. In addition, STM images revealed surface reconstruction of oxygen-rich films which is tentatively explained by relaxation within the Fe sublattice. The results show that the CO oxidation reaction over this film proceeds via the Mars-van Krevelen type mechanism. Replacing O<sub>2</sub> with NO as an oxidative agent leads to the formation of virtually identical oxygen-rich films. However, the CO + NO reaction over these films does not show sustained reactivity. It is, therefore, suggested that the replenishment of oxygen vacancies formed as a result of CO<sub>2</sub> formation and desorption is the rate-limiting step. We show that basically the

same picture holds true for the encapsulated Pt / Fe<sub>3</sub>O<sub>4</sub>(111) system, which showed enhanced reactivity in CO + O<sub>2</sub> reaction as compared to clean Pt particles.

The α-Fe<sub>2</sub>O<sub>3</sub>(0001) films can be prepared as unreconstructed (1x1) as well as the so-called “biphase” surfaces. The results indicate that the stability of the (1x1) surface may be related to the surface contamination. “Biphase”-terminated α-Fe<sub>2</sub>O<sub>3</sub> surfaces are shown to be an excellent template for the growth of monodispersed Au nanoparticles with a narrow particle size distribution. The particles are resistant towards sintering up to 700 K in UHV. The effect of hydroxylation of “biphase” α-Fe<sub>2</sub>O<sub>3</sub> films was examined by exposure to high pressures of H<sub>2</sub>O. Preliminary studies on the thermal stability of Pt particles supported on α-Fe<sub>2</sub>O<sub>3</sub>(0001)-(1x1) films are also reported.

# Zusammenfassung

## Eine Rastertunnelmikroskopie-Studie von eisenoxidbasierten Modellkatalysatoren

Eisenoxidfilme, wie FeO(111), Fe<sub>3</sub>O<sub>4</sub>(111) und α-Fe<sub>2</sub>O<sub>3</sub>(0001) auf Platin(111)-Oberflächen, haben sich als geeignete Modellsysteme für eisenoxidbasierte Katalysatoren erwiesen. In der vorliegenden Arbeit wurde deren Morphologie charakterisiert. Außerdem wurden Bildung, Wachstum und thermische Stabilität von Pt- und Au-Nanopartikeln auf derartigen Oberflächen untersucht. Im Fokus stand insbesondere ein besseres Verständnis der wechselseitigen Beziehung von Struktur und Reaktivität im Fall der Tieftemperatur-CO-Oxidation im Millibar Bereich. Strukturuntersuchungen wurden primär mit Hilfe eines STM (Rastertunnelmikroskop) in Kombination mit LEED- (engl.: Low Energy Electron Diffraction), AES- (Auger-Elektronen-Spektroskopie) und TPD-Messungen (Temperatur-programmierte Desorption) durchgeführt.

Auf Fe<sub>3</sub>O<sub>4</sub>(111)-Oberflächen nukleiert Pt ungeordnet unter Ausbildung zweidimensionaler Inseln, die mit zunehmender Bedeckung miteinander verschmelzen. Diese Inseln scheinen die Struktur der unterliegenden Oxidschicht zu adaptieren, was deren CO-Adsorptionsvermögen stark beeinflusst. Ein Ausheilen unter UHV-Bedingungen führt zum Sintern der Partikel und der Bildung wohldefinierter, dreidimensionaler Partikel. Es konnte gezeigt werden, dass eine Hochtemperaturbehandlungen unter Reduktionsbedingungen zu einer Ummantelung der Pt-Partikel mit einem Eisenoxidfilm führt. Ursache ist eine sogenannten Starke Metall-Träger Wechselwirkung (engl.: Strong Metal-Support Interaction; SMSI). Atomar-aufgelöste STM-Aufnahmen zeigen, dass es sich bei dieser Schicht um eine FeO(111)-Monolage handelt.

Ultradünne FeO(111)-Filme auf Pt(111)-Oberflächen zeigen eine stark erhöhte Reaktivität für die CO-Oxidationsreaktion. Mittels STM-Untersuchungen konnte gezeigt werden, dass dies auf die sauerstoffinduzierte Umwandlung der O-Fe-Doppelschicht in die katalytisch aktive O-Fe-O-Dreischichtstruktur zurückzuführen ist. Zudem offenbarten die STM-Aufnahmen eine Oberflächenrekonstruktion der sauerstoffreichen Filme, was vermutlich auf den Abbau von Spannungen innerhalb des Fe-Untergitters zurückzuführen ist.



Die Ergebnisse lassen erkennen, dass die CO-Oxidation auf diesen Filmen nach dem Mars-van Krevelen Mechanismus abläuft. Ersetzt man den Sauerstofflieferanten  $O_2$  durch NO führt dies zur Bildung nahezu identischer sauerstoffreicher Filme. Allerdings weist die Reaktion  $CO + NO$  über diesen Filmen keine anhaltende Reaktivität auf. Aus diesem Grund wird vermutet, dass das Wiederauffüllen der durch die  $CO_2$ -Bildung und -Desorption erzeugten Sauerstoffstellen, der geschwindigkeitsbestimmende Schritt ist. Es konnte gezeigt werden, dass prinzipiell das gleiche Verhalten auch für das ummantelte Pt/ $Fe_3O_4(111)$ -System beobachtet wird, welches im Vergleich zu den sauberen Pt-Partikeln eine erhöhte Reaktivität für die Reaktion  $CO + O_2$  zeigt.

Die  $\alpha-Fe_2O_3(0001)$ -Filme können sowohl mit einer unrekonstruierten  $(1 \times 1)$ -Oberfläche, als auch mit einer sogenannten „biphase“- („zwei-phasigen“) Oberfläche präpariert werden. Die Ergebnisse deuten darauf hin, dass die Stabilität der  $(1 \times 1)$ -Oberfläche auf Verunreinigungen auf der Oberfläche zurückzuführen ist. „Biphase“-terminierte  $\alpha-Fe_2O_3$ -Oberflächen erweisen sich als ausgezeichnete Unterlagen für das Wachstum monodisperser Au-Nanopartikel mit geringer Streuung der Partikelgröße. Diese Partikel sind gegenüber Sintern bis zu 700 K im UHV beständig. Der Effekt der Hydroxylierung „biphase“  $\alpha-Fe_2O_3$ -Filme wurde untersucht, indem diese hohen  $H_2O$ -Drücken ausgesetzt wurden. Zudem werden erste Ergebnisse zur Wärmebeständigkeit von Pt-Partikel auf  $\alpha-Fe_2O_3(0001)$ - $(1 \times 1)$ -gestützten Filmen präsentiert.

# Contents

## 1. Introduction

1.1 Catalysis & model systems .....	1
1.2 Strong Metal-Support Interaction (SMSI) .....	6
1.3 CO oxidation reaction.....	9
1.4 Iron oxides: FeO, Fe <sub>3</sub> O <sub>4</sub> & α-Fe <sub>2</sub> O <sub>3</sub> .....	11

## 2. Experimental

2.1 Apparatus .....	17
2.2 Methods:	
2.2.1 Scanning Tunneling Microscopy (STM) .....	23
2.2.2 Low Energy Electron Diffraction (LEED) .....	30
2.2.3 Auger Electron Spectroscopy (AES).....	34
2.2.4 Temperature Programmed Desorption (TPD).....	37

## 3. Morphology of Pt nanoparticles on Fe<sub>3</sub>O<sub>4</sub>(111) / Pt(111)

3.1 Introduction.....	43
3.2 Samples preparation .....	44
3.3 Results & Discussion	
3.3.1 Nucleation and growth .....	46
3.3.2 Thermal stability.....	47

## 4. Ultrathin FeO(111) films on Pt(111) in CO oxidation reaction

4.1 Introduction.....	61
4.2 Samples preparation .....	63
4.3 Results & Discussion	
4.3.1 FeO(111) / Pt(111) vs. Pt(111) .....	64

4.3.2 O-lean conditions .....	66
4.3.3 O-rich conditions .....	70
4.3.4 Reaction mechanism .....	81
4.3.5 CO + O <sub>2</sub> vs. CO + NO .....	85
4.3.6 Encapsulated Pt / Fe <sub>3</sub> O <sub>4</sub> (111) in CO oxidation reaction .....	90

## **5. Au & Pt nanoparticles supported on $\alpha$ -Fe<sub>2</sub>O<sub>3</sub>(0001) films**

5.1 Introduction.....	96
5.2 Samples preparation .....	97
5.3 Results & Discussion	
5.3.1 Au / $\alpha$ -Fe <sub>2</sub> O <sub>3</sub> -“biphase” .....	99
5.3.2 Pt / $\alpha$ -Fe <sub>2</sub> O <sub>3</sub> -(1x1) .....	105

## **6. Summary .....**

109

## Literature .....

112

List of abbreviations

List of figures

Appendix A: Curriculum Vitae (CV)

Appendix B: List of publications & conference appearances

Erklärung

*“This is a new power to produce chemical activity  
belonging to both inorganic and organic nature,  
which is surely more widespread than we have hitherto believed  
and the nature of which is still concealed from us.”*

Jöns Jakob Berzelius

# Chapter 1

## Introduction

### 1.1 Catalysis & model systems

“A *catalyst* is a material that converts reactants into products through a series of elementary steps, in which the catalyst participates while being regenerated to its original form at the end of each cycle during its lifetime” [1]. The process in which the rate of a chemical reaction is changed by a catalyst is called *catalysis*. The catalyst can be in the same state of matter as the reactants (*homogeneous catalysis*) or they can be in different phases (*heterogeneous catalysis*). A catalyst can be characterized by various parameters, such as the *turnover frequency (TOF)* which is the number of molecules of a given product made per catalytic site per unit time [2], *selectivity* of the catalyst towards specific reaction(s) and not other side-reactions and the *catalyst lifetime* which is determined by systematical poisoning of the catalyst in every catalytic cycle by side products, which leads to catalyst’s deactivation. The TOF strongly depends on the so called *rate-limiting step* of the reaction which is the most time-consuming *elementary step*.

The history of catalysis dates back to antiquity when it was observed as an experimental fact, there are also some writings from medieval ages, but the first explanations of catalytic processes come from XIXth century from the works of Berzelius [3]. XXth century brought great discoveries in solid-gas heterogeneous catalysis, which resulted in the Nobel Prize in Chemistry granted to Fritz Haber in 1918 for ammonia synthesis [4]. From a certain point in time it was rather clear that the catalytic reactions take place on a surface of a catalytic material and are not much influenced by the bulk. Until 1950s the catalytic processes were mainly described from a macroscopic point of view. With development of surface science and invention of surface science instruments and techniques, the preparation, as well as microscopic characterization, of well defined atomically clean catalytic surfaces was made possible. In addition, simulations of physical effects and chemical reactions in ideal conditions could be made due to advances in

computational theoretical modeling. All this led to increasing understanding of catalytic processes and made catalyst optimization, i.e. increasing the reaction rate and / or selectivity of a catalyst, possible. In 2007 Gerhard Ertl, one of the key persons in the field of applying surface science techniques to the study of catalytic processes, was awarded the Nobel Prize in Chemistry [5] which emphasized the importance of surface science studies on catalytic materials. A very elegant introduction to the historical timeline of catalysis and surface science is given in various books on the topic [6-7].

First catalysts were rather simple, mainly single crystals and foils. Modern heterogeneous catalysts are complex, multi-component materials. Most commonly, oxide supported metal particles are used. The properties of such catalysts strongly depend on their structural details. Parameters like particle size, number of plane / edge sites, crystallographic orientations of particles planes and edges, number / type of defects and the nature of the interface between the particles and the oxide support can play a decisive role on reactivity. In addition, thermal / high pressure stability and electronic properties of the metal-oxide system have to be taken into account when explaining the catalytic activity of such material. In order to study the effect of all the aspects mentioned, clean and well-defined experiments have to be performed in ultra-high vacuum. For this reason, usually thin oxide films are grown on metal single crystals. Typically: (i) metal single metal crystal is cleaned and (ii) subsequently oxidized at high temperatures in order to form an oxide layer on top, or (alternatively) (iii) different (the same) metal is deposited onto the metal single crystal and oxidized. The oxide layer can be directly involved in catalytic reactions or stabilize the structure of catalytically active metal particles (or both). In the latter case (iv) metal particles are deposited on top of the oxide. Sometimes oxide single crystals are used instead of performing steps (i) and (ii), however, the metal single crystal which is used as a support for the oxide film growth can influence oxide's and particles properties. That is why metal particles supported on oxide single crystal and the particles of the same metal supported on oxide film grown on metal single crystal should be considered as different catalytic systems. The most important aspect is a perfect control over the catalyst's preparation procedure and the cleanness of the experiments. Well-defined atomically clean metal-oxide systems can act as ideal models for observations how the specific surface sites (particle planes / edges / steps / kinks, oxide support, defects, etc.) influence catalytic reactions (see [8, 9] and

---

reference therein). Typical *model systems* are schematically shown in Figs. 1.1(a)-(c):

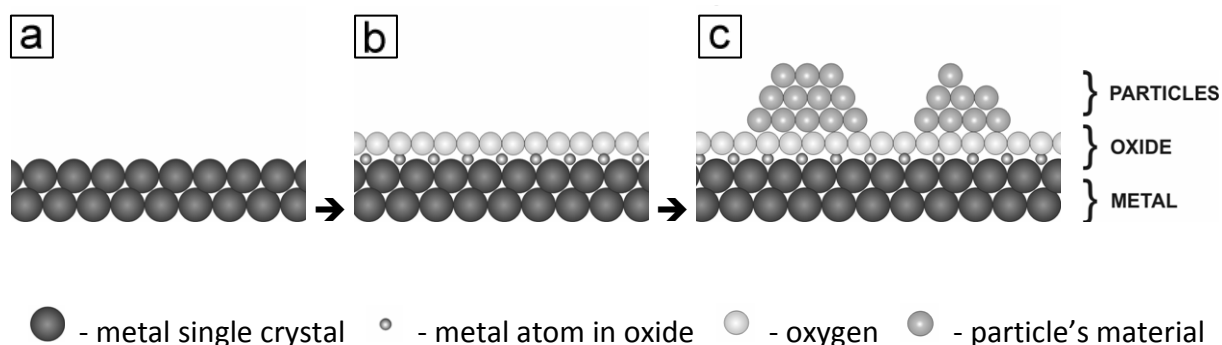


**Fig. 1.1** Model systems with increasing level of complexity:  
metal single crystal (a), oxide film (b) & oxide supported metal particles (c)

With modern experimental tools it is possible to perform detailed structural studies of catalytic materials before, after and even during catalytic reactions on the atomic level. By monitoring the changes in morphology and chemical composition of the system one can often determine the reaction mechanism: identify the intermediate steps and the reaction byproducts. The UHV results have to be then linked to real (industrial) reaction conditions which include high temperatures, high pressures of gases and the presence of contaminations (such as  $\text{H}_2\text{O}$ ), as these can influence the course of catalytic reaction.

The preparation of well-defined metal-oxide systems is not trivial. To find a proper oxide preparation procedure is often a try-and-error process. The atoms of some metals can exist in various oxidation states and thus form oxides of different stoichiometry. The formation of a specific oxide depends on oxidation conditions, i.e. temperature and  $\text{O}_2$  pressure, which are often difficult to optimize. In addition, in case of metal oxide films grown on single crystals of different metals, similarity in lattice constants between the oxide and the support is important in order to form a well-ordered oxide layer. Nevertheless, many preparation procedures for different oxide thin films have been successfully established [10-13]. It is also unknown and difficult to predict how the particles of different metals will grow on top of a particular oxide. Particles can nucleate randomly or on specific oxide sites such as terraces, step edges, defects or other energetically favorable positions. During deposition the particles can coalesce (small particles combine and form larger ones). Substrate

temperature is also an important factor as it determines surface diffusion. High temperatures result in particles sintering in a process called Ostwald ripening [14].

The surface always exhibits different properties than the bulk of the material because of different bonds configuration. The disruption of bonds on the surface produces an excess of energy which is called the *surface energy* ( $\gamma$ ) [15]. The bonding characteristics of metals to oxides are mainly determined by their surface energies and the energy of the interface between them. These energies influence the growth mode and wetting or non-wetting of the surface. The possible growth modes of thin films have been systematically classified by Ernst Bauer [16]:

In *Volmer-Webber type of growth* the deposits nucleate on the surface forming particles which grow in height with increasing coverage (Fig. 1.2(a)). The deposits do not tend to wet the surface. This takes place when the bonding strength between the atoms of the deposited material is stronger than the bonding between the deposits and the support. An example are metal particles grown on oxide surfaces.

In *Frank-van der Merwe type of growth* the deposits do not form high particles, but grow in a layer-by-layer mode, wetting the surface (Fig. 1.2(b)). This happens in case of strong bonding between the deposited atoms and the support. It is a typical growth mode for metals grown on metals.

*Stransky-Krastanov type of growth* is a specific case: first a full layer is formed and then particles / islands grow on top of the layer (Fig. 1.2(c)).

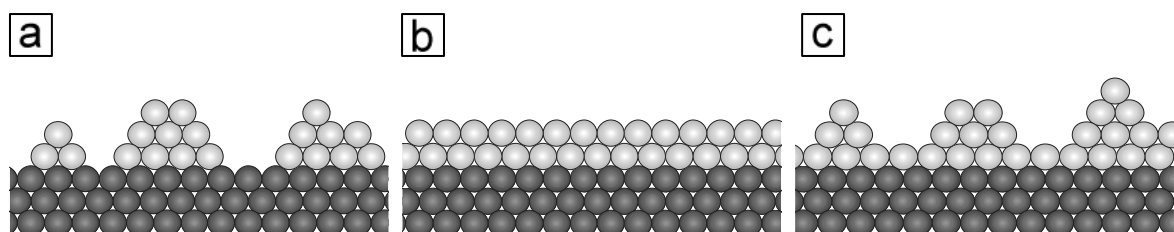


**Fig. 1.2** Graphical comparison of thin film growth modes: Volmer-Webber (a), Frank-van der Merwe (b) and Stransky-Krastanov (c)



A metal particle supported on oxide film can be, in equilibrium state, described by Young's equation [17] which includes the surface energy of the particle, the surface energy of the support and the energy of the interface between the particle and the support:

$$\gamma_{oxide} = \gamma_{metal} \cos \theta + \gamma_{interface} \quad (1)$$

where  $\theta$  is the contact angle between  $\gamma_{metal}$  and  $\gamma_{interface}$ . A schematic drawing of a metal particle on oxide support (system in thermodynamic equilibrium) is shown in Fig. 1.3:

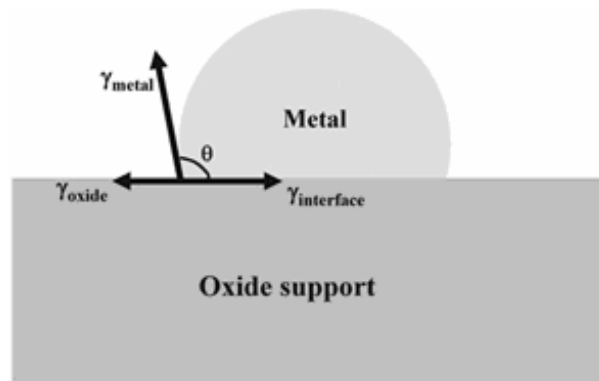


**Fig. 1.3** Schematic drawing of a metal particle on oxide support: system in thermodynamic equilibrium [17]

The interface energy cannot be experimentally measured. To extract the value of the interface energy the *work of adhesion*, defined as the strength of bonding of the particle to the oxide, is being calculated from Dupré equation:

$$W_{adh} = \gamma_{metal} + \gamma_{oxide} - \gamma_{interface} \quad (2)$$

Knowing the structural parameters of a supported particle that reached the equilibrium shape, such as height, width and lengths of edges running along specific crystallographic directions, the work of adhesion can be calculated using the modified *Wulff construction* [18, 19]. Fig. 1.4 shows a schematic drawing of a supported particle exhibiting (111) top facet and

(111) / (100) side facets. The structural parameters are indicated.

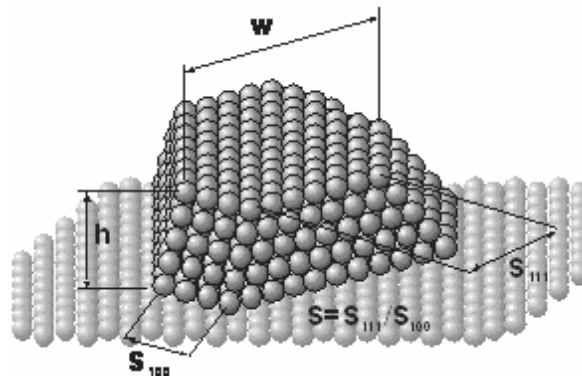


**Fig. 1.4** Schematic drawing of a supported particle exhibiting (111) top facet and (111) / (100) side facets: structural parameters indicated (provided by S. Shaikhutdinov)

The work of adhesion can be calculated from the following equation:

$$W_{adh} = \gamma_{111} \left( 2 - \frac{3}{\sqrt{2}} \frac{h}{w} \frac{s+1}{2s+1} \right) \quad (3)$$

where  $h$  is the height of the particle,  $s$  is the width and  $\gamma_{111}$  is the surface energy of a (111) plane of a specific particle's material.

It is important to mention that under reaction conditions, i.e. high gas pressures and high temperatures, significant changes in particles morphology may occur: sintering, reshaping, surface reconstructions and other effects, such as Strong Metal-Support Interaction (SMSI), can take place.

## 1.2 Strong Metal-Support Interaction (SMSI)

The term *Strong Metal-Support Interaction (SMSI)* was first introduced by Tauster et al. in 1978 [20]. The authors studied group 8 noble metals supported on  $\text{TiO}_2$ . The discovery was that upon reducing treatments, such as heating the sample to high temperatures in UHV, the chemisorption properties of noble metal particles are strongly altered. TEM

(Transmission Electron Microscopy), XPS (X-ray Photoelectron Spectroscopy) and TPD (Temperature Programmed Desorption) results gave clear evidence that the near zero sorption of H<sub>2</sub> and CO could not be only explained by agglomeration of metal particles upon annealing but also by “metal-support interactions of a type not previously recognized”. The proposed explanation for the unusual behavior was the formation of chemical bonds between the noble metals and the Ti cations / atoms or, alternatively, a formation of intermetallic compounds. The metals studied were: ruthenium, rhodium, palladium, osmium, iridium and platinum.

In 1993 Pan and Madey reported the SMSI effect for Fe on TiO<sub>2</sub>(110) [21]. XPS and LEIS (Low Energy Ion Scattering) results revealed that iron clusters were covered by a thick layer of titanium suboxide TiO<sub>x</sub>. Such “encapsulation” was yet another explanation of the SMSI. In addition, it was the first time when the effect was reported for a non-noble metal. Studies of the same group also gave evidence for the encapsulation of Pt particles supported on the same support [22] and revealed no SMSI for titania supported Au [23]. This indicated that the nature of metal deposit also plays an important role in the effect.

In 1999 Dulub, Hebenstreit and Diebold studied Pt particles supported on TiO<sub>2</sub>(110) with STM, STS (Scanning Tunneling Spectroscopy) and LEIS. They published atomically resolved STM images of TiO<sub>x</sub> overlayer that formed on top of Pt particles upon high temperature annealing [24]. The structure of the overlayer was later described in detail in the paper by Jennison [25].

The same year Suzuki and Souda showed that in case of Pd / TiO<sub>2</sub>(110) the encapsulating material migrates onto the particles via a mass transport along the surface and not through the metal particles [26]. The main experimental technique used was CAICISS (Coaxial Impact-Collision Ion Scattering Spectroscopy). The conclusion was based on the investigation of changes in interatomic and interlayer spacings within the particles during the encapsulation. The results revealed that the crystal structure of Pd islands and the metal-oxide interface remained unchanged throughout the process.

Two years later Mullins and Zhang reported the SMSI for Pt supported on partially reduced cerium oxide CeO<sub>2-x</sub> [27]. The studies were based on SXPS (Soft X-ray Photoelectron Spectroscopy) and TPD results. Interestingly, the effect was not observed for fully oxidized ceria. The results raised a discussion whether the SMSI is somehow related to a reducibility

---

of the oxide which acts as a support. Surprisingly, the group of Mullins did not observe the encapsulation of Pd particles on the same support [28].

Studies of Gao et al. on Pt supported on  $\text{TiO}_2(100)$  and Nb-doped  $\text{TiO}_2(100)$  films revealed that high oxygen vacancy defects density in the oxide's bulk may be essential for the encapsulation, as the process involves defects diffusion to the particle-oxide interface [29]. The encapsulation phenomenon was also addressed by Fu et al. who studied the influence of the electronic structure of  $\text{TiO}_2(110)$  on the encapsulation of metal particles supported on this oxide [17, 30]. The conclusion was that, in favorable cases, an electron transfer from the oxide to the metal may occur resulting in a formation of positive space charges at the oxide's surface and a negatively charged metal cluster – a situation which promotes oxide material migration onto the metal particles. This may occur in case of a metal with relatively high surface energy supported on an oxide with a relatively low surface energy [31].

Great contribution to the subject was made by the group of Bowker. Using STM they studied encapsulated Pd particles supported on  $\text{TiO}_2(110)$  and found different  $\text{TiO}_x$  structures on top of annealed Pd clusters [32-35]. Some of these structures were quite similar to the structure observed by Diebold et al. on Pt particles. However, it was not clear whether the encapsulating overlayers are intermetallic-like alloys or complete titania layers. Titanium oxide overlayers were also observed by Silly and Castell on top of Pd particles supported on  $\text{SrTiO}_3(001)$  [36] and by Majzik et al. on Rh nanoparticles supported on  $\text{TiO}_2(110)$  [37]. Various  $\text{TiO}_x$  structures were described by Sedona et al. in a kind of “inverted” experiment where titanium oxide thin films were grown on Pt(111) single crystal [38]. Similar studies were performed by the group of Castell using Au(111) surface as a substrate for the oxide growth [39]. The observed structures were similar to the  $\text{TiO}_x$  overlayers observed on top of encapsulated Pt and Pd particles.

To the best of today's knowledge SMSI is observed for metal particles supported on reducible oxides after reducing treatment (such as high temperature annealing in UHV). It is generally accepted that the effect occurs between metals with high surface energy supported on oxides having relatively low surface energy.

### 1.3 CO oxidation reaction

Carbon monoxide (CO) is a colorless, odorless, flammable gas which is highly toxic to all live beings [40]. It is formed in a process of incomplete oxidative conversion of carbon and carbon-containing compounds to carbon dioxide (CO<sub>2</sub>). CO oxidation, especially CO oxidation over platinum group metals, is one of the most important and widely studied reactions in catalysis (see [41-45] and references therein). CO and NO<sub>x</sub> (nitrogen oxides) are the main pollutants emitted from gasoline and diesel engines, that is why "neutralization" of CO by conversion to less toxic CO<sub>2</sub> is critical [46]. The reaction basically follows the following chemical equation:



CO oxidation can take place on metal or oxide surfaces. In case of reaction taking place on metals, one of the critical steps is the O<sub>2</sub> dissociation on the metal surface. In case of reaction on oxides the oxygen atom is taken from the oxide directly. There are three mechanisms proposed for CO oxidation:

*Langmuir-Hinshelwood mechanism* is proposed for CO oxidation over metal surfaces. It includes co-adsorption of O<sub>2</sub> and CO on the surface, dissociation of O<sub>2</sub>, formation and desorption of CO<sub>2</sub> to the gas phase (Fig. 1.5).

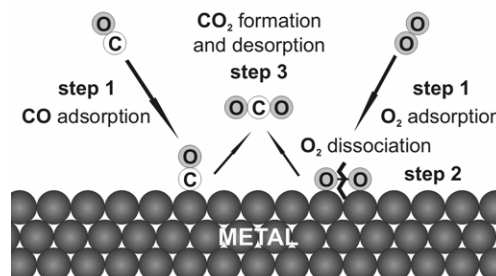


**Fig. 1.5** Langmuir-Hinshelwood CO oxidation reaction mechanism

The adsorption of CO on metals follows the *Blyholder model* [47]. The bond formation includes a donation of electrons from the highest filled bonding molecular orbital of the CO ( $\sigma$ ) to the unoccupied orbitals of the metal and a back-donation from the occupied orbitals of the metal to the lowest filled antibonding molecular orbital of the CO ( $\pi^*$ ).

*Eley-Rideal mechanism* is yet another model proposed for CO oxidation over metal surfaces. It proceeds via adsorption of  $O_2$  on the surface and direct reaction with the gas phase CO through a collision of the two species which leads to  $O_2$  dissociation and  $CO_2$  formation (Fig. 1.6).

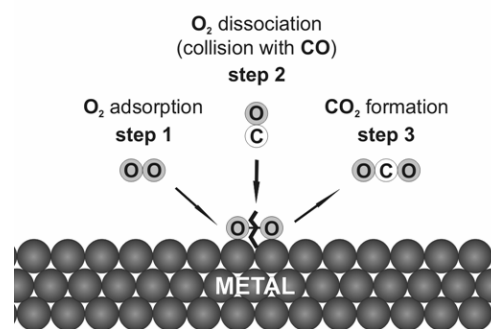


**Fig. 1.6** Eley-Rideal CO oxidation reaction mechanism

*Mars-van Krevelen mechanism* is proposed for CO oxidation over oxide surfaces. CO reacts with a lattice oxygen atom of the oxide forming  $CO_2$  which desorbs leaving an oxygen vacancy, and the vacancy is replenished by  $O_2$  from the gas phase (Fig. 1.7).

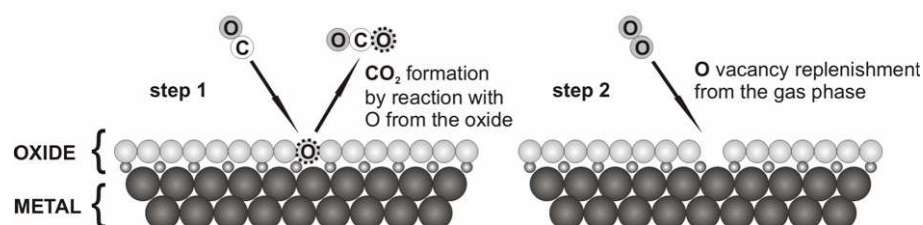


**Fig. 1.7** Mars-van Krevelen CO oxidation reaction mechanism

#### 1.4 Iron oxides: FeO, Fe<sub>3</sub>O<sub>4</sub> & α-Fe<sub>2</sub>O<sub>3</sub>

Metallic iron and iron oxides are used in many industrial catalytic processes, such as dehydrogenation of ethylbenzene to styrene in the presence of steam [48]. Iron has its noble place in the history of catalysis as it was the catalyst used by Fritz Haber for ammonia synthesis [4]. Nowadays mainly K-promoted iron oxides are industrially used. Iron oxides occur naturally, e.g. they are the main component of rust. For catalytic studies, iron oxide single crystals or well-ordered thin (nanometer thick) iron oxide films, grown on metal single crystals by iron deposition and oxidation at high temperatures, are used. At different oxygen pressures and oxidation temperatures, Fe and O can form crystal structures of different stoichiometry, where Fe can be <sup>2+</sup> or <sup>3+</sup> coordinated. The calculated temperature-pressure phase diagram for the iron-oxygen system is shown in Fig. 1.8. As illustrated, three stable iron oxide structures can be formed: FeO, Fe<sub>3</sub>O<sub>4</sub> and Fe<sub>2</sub>O<sub>3</sub>. These are also the three which occur naturally. In our experiments iron oxide films were grown on Pt(111) single crystal. Pt(111) was found to be a suitable support for the growth of iron oxide films (see [10] and references therein): it has a lattice constant of 2.77 Å (close to 3.04 Å which is the surface lattice constant of bulk FeO(111)) and a hexagonal surface unit cell (also similarly to FeO(111)). Additionally, as we will illustrate in the experimental chapters, there is a high adhesion energy and good epitaxial relationship between platinum and iron oxides.

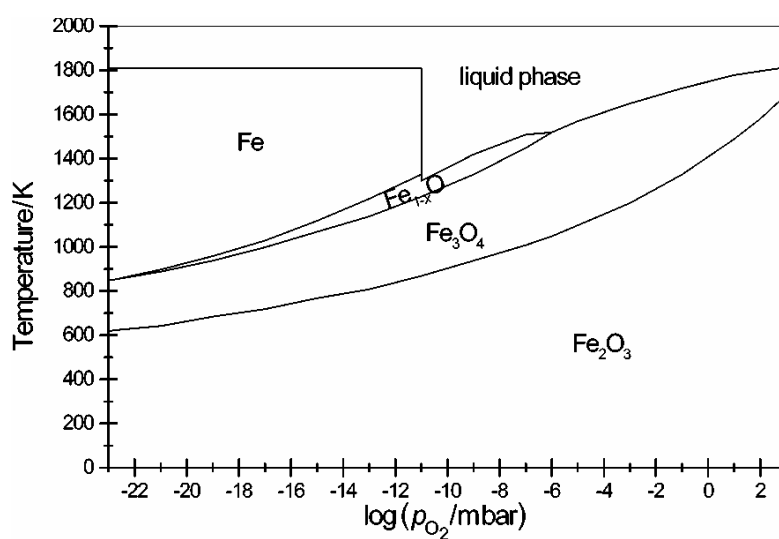
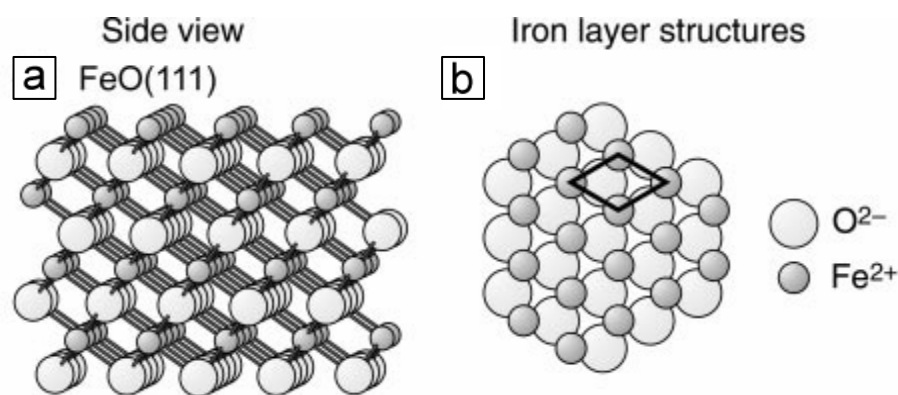


Fig. 1.8 Calculated temperature-pressure phase diagram for the iron-oxygen system [49]

*FeO (wüstite)*

FeO is the most simple iron oxide which crystallizes in the rock-salt structure [10]. A cubic unit cell includes four formula units and has a lattice constant of 4.3 Å. Oxygen  $O^{2-}$  anions form a close-packed fcc sublattice while  $Fe^{2+}$  cations are located underneath in the interstitial sites [50]. All iron atoms are octahedrally coordinated to oxygen. FeO(111) films can be grown on Pt(111) up to 2.5 ML. A monolayer (ML) FeO(111) film consists of one atomic layer of iron and one atomic layer of oxygen. Both O and Fe planes have an atomic periodicity of 3.09 Å (3.04 Å in the bulk). This periodicity can be observed on atomic resolution STM images. The height of 1 ML FeO(111) / Pt(111) is  $\sim 2.5$  Å. The Pt–Fe and Fe–O interlayer distances are 1.89 Å and 0.62 Å, respectively (Fe–O distance in bulk FeO is 1.25 Å). The step height is  $\sim 2.3$  Å which corresponds to the step height in Pt(111). The film is O-terminated which determines its inertness. The model structure of FeO(111) is presented in Fig. 1.9. FeO(111) ultrathin films grown on Pt(111) exhibit a Moiré pattern [51] which has a periodicity of  $\sim 25$  Å and a corrugation amplitude of  $\sim 0.1$  Å. The Moiré derives from  $\sim 12\%$  lattice mismatch between platinum and iron oxide. The superstructure can be seen in STM. The LEED pattern of FeO(111) / Pt(111) consists of six hexagonally arranged (1x1) spots characteristic for substrate Pt(111), six hexagonally arranged (1x1) spots corresponding to FeO(111) film and additional satellite spots, located around FeO(111) spots, which represent the Moiré superstructure. Typical LEED pattern and STM images of FeO(111) film grown on Pt(111) are shown in Fig. 1.10.



**Fig. 1.9** Model structure of FeO(111): side view (a) & top view (b) [49]



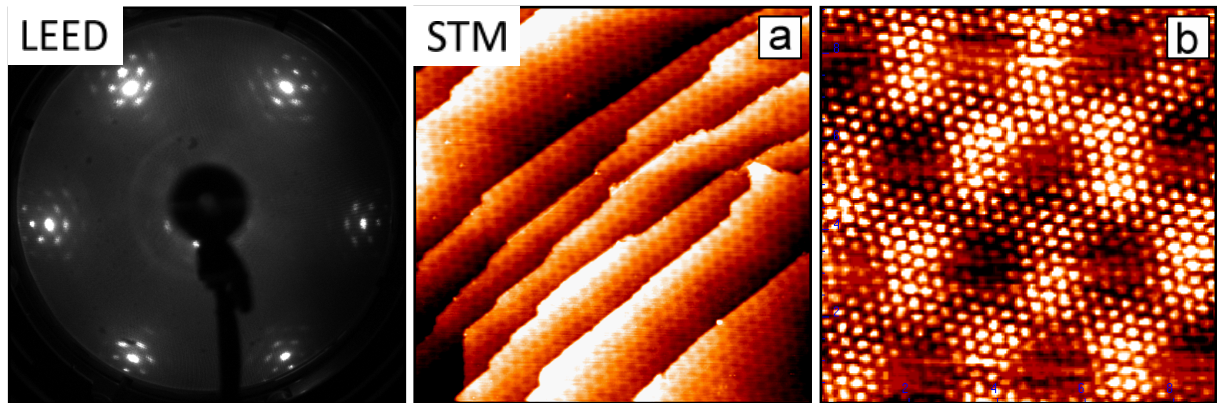


**Fig. 1.10** FeO(111) / Pt(111): LEED pattern & STM images

(LEED: 64 eV; STM: 100 x 100 nm<sup>2</sup>, 0.7 V, 0.4 nA (a) and 9 x 9 nm<sup>2</sup>, 1.6 V, 0.7 nA (b))

Three high symmetry regions can be distinguished within the Moiré: “top”, “fcc” and “hcp” [52]. The acronyms stem from positions of Fe and O atoms with respect to substrate Pt atoms. In “top” regions the interface O atoms are in hollow positions with respect to Pt and Fe atoms are on-top of Pt atoms, in “fcc” regions both Fe and interface O atoms are in threefold hollow positions with respect to Pt atoms and in “hcp” regions O atoms are located on-top of the surface Pt atoms, while Fe atoms are in hollow positions. STM image of FeO(111) / Pt(111) with indicated high symmetry regions within the Moiré unit cell is shown in Fig. 1.11:

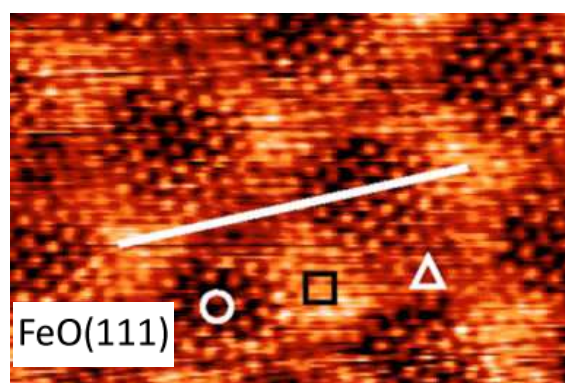


**Fig. 1.11** High symmetry regions within the FeO(111) / Pt(111) Moiré unit cell:

“top” (circle), “fcc” (square) & “hcp” (triangle) [52]

*Fe<sub>3</sub>O<sub>4</sub> (magnetite)*

$\text{Fe}_3\text{O}_4$  crystallizes in the inverse spinel structure [10]. A cubic unit cell includes eight formula units  $(\text{Fe}^{3+})_{\text{tet}}[\text{Fe}^{2+}\text{Fe}^{3+}]_{\text{oct}}\text{O}^{2-}_4$  and has a lattice constant of 8.396 Å. Oxygen  $\text{O}^{2-}$  anions form hexagonal close-packed fcc sublattices with ABC stacking, while iron cations are located in the interstitial sites forming either Kagomé-type or mixtrigonal layers. Kagomé layers consist of octahedrally coordinated  $\text{Fe}^{2+}$  and  $\text{Fe}^{3+}$  ions while the mixtrigonal layers consist of tetrahedrally and octahedrally coordinated  $\text{Fe}^{3+}$  ions. Unoccupied sites within each Kagomé layer form a hexagonal lattice with a periodicity of 5.94 Å. The same periodicity is observed for iron ions in mixtrigonal layers. This is also the periodicity seen on atomic resolution STM images of unreconstructed  $\text{Fe}_3\text{O}_4(111)$ . The nearest neighbour distance in oxygen sublattices is 2.97 Å. The surface terminations of  $\text{Fe}_3\text{O}_4(111)$  are still a matter of discussion [10, 53, 54], although the oxide in its unreconstructed form is believed to be terminated by 1/4 ML of  $\text{Fe}^{3+}_{\text{tet}}$  on top of a closed-packed oxygen layer in single crystal and  $\text{Fe}^{2+}_{\text{oct}}$  on top of 1/4 ML of  $\text{Fe}^{3+}_{\text{tet}}$  in film on Pt(111). Naturally grown crystals exhibit octahedral shapes which is a proof for the stability of (111) surface plane. The step height is 4.85 Å which corresponds to a distance between equivalent (111) terminations. The model structure of  $\text{Fe}_3\text{O}_4(111)$  is shown in Fig. 1.12. The LEED pattern of  $\text{Fe}_3\text{O}_4(111)$  / Pt(111) consists of (1x1) spots characteristic for Pt(111) and (2x2) spots which derive from above mentioned 5.94 Å periodicity in  $\text{Fe}_3\text{O}_4(111)$ . Typical LEED pattern and STM images of  $\text{Fe}_3\text{O}_4(111)$  / Pt(111) are presented in Fig. 1.13.

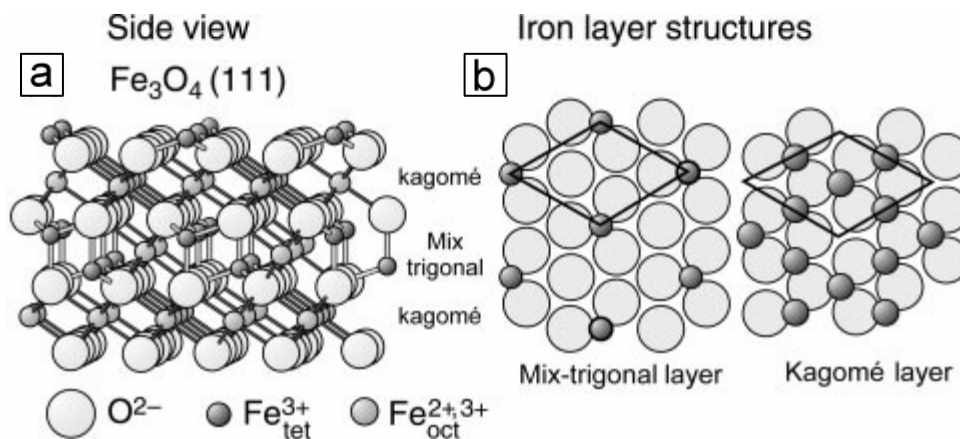


**Fig. 1.12** Model structure of  $\text{Fe}_3\text{O}_4(111)$ : side view (a) & top view (b) [49]

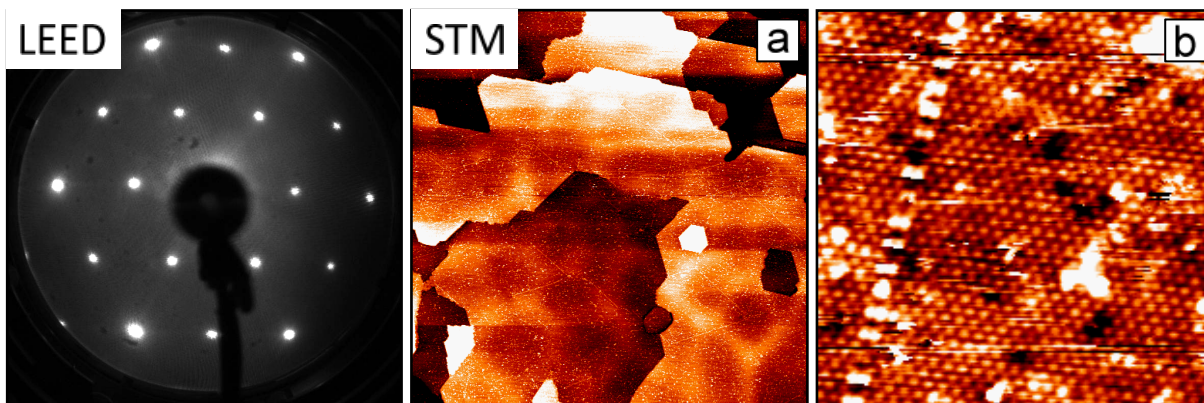


**Fig. 1.13**  $\text{Fe}_3\text{O}_4(111)$  /  $\text{Pt}(111)$ : LEED pattern & STM images

(LEED: 64 eV; STM:  $500 \times 500 \text{ nm}^2$ , 1.4 V, 0.7 nA (a) and  $20 \times 20 \text{ nm}^2$ , 1.4 V, 0.7 nA (b))

### $\alpha\text{-Fe}_2\text{O}_3$ (hematite)

$\alpha\text{-Fe}_2\text{O}_3$  is the only iron oxide phase that is stable at room temperature in ambient conditions. It crystallizes in the corundum structure [10]. The prefix “alfa” is used to distinguish this naturally occurring phase with other synthesized artificially (such as  $\gamma$  (so called maghemite)). A hexagonal unit cell includes six formula units and has lattice constants of  $a = 5.035 \text{ \AA}$  and  $c = 13.72 \text{ \AA}$ . Oxygen  $\text{O}^{2-}$  anions form hcp sublattices in ABAB stacking, while iron  $\text{Fe}^{3+}$  cations are located in the interstitial sites, arranged in a distorted octahedra. The O-O distance in oxygen sublattices is  $2.91 \text{ \AA}$ . Iron ions form two sublayers with interatomic distances of  $5.03 \text{ \AA}$ . This is also the surface lattice constant of unreconstructed (0001) plane and the periodicity seen on atomic resolution STM images. The step height is  $2.29 \text{ \AA}$  which corresponds to a distance between two O planes. The model structure of  $\alpha\text{-Fe}_2\text{O}_3(0001)$  is shown in Fig. 1.14. Surface terminations are still a matter of debate (for details please refer to Chapter 5). On  $\text{Pt}(111)$   $\alpha\text{-Fe}_2\text{O}_3(0001)$  films can grow as unreconstructed (1x1) as well as the so-called “biphase” surfaces. The LEED pattern of the unreconstructed (1x1) surface is a  $(\sqrt{3}\times\sqrt{3})R30^\circ$  with respect to  $\text{Pt}(111)$ -(1x1) spots. The LEED pattern of the “biphase”-terminated surface has additional satellite spots around all of the  $\alpha\text{-Fe}_2\text{O}_3(0001)$ -(1x1) spots. STM images of the “biphase” show complicated superstructure with long-range periodicity of  $\sim 45 \text{ \AA}$ . Typical LEED patterns and STM images of “biphase”- and (1x1)-terminated  $\alpha\text{-Fe}_2\text{O}_3(0001)$  films on  $\text{Pt}(111)$  are presented in Fig. 1.15.

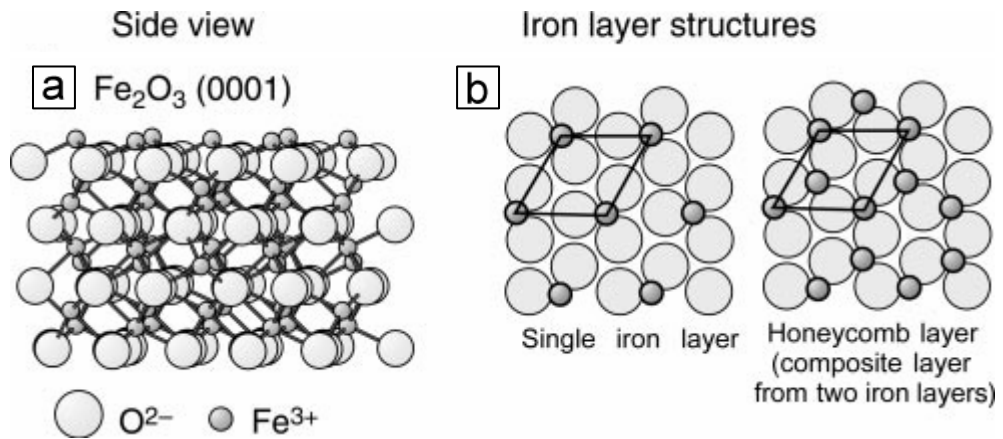


**Fig. 1.14** Model structure of  $\alpha\text{-Fe}_2\text{O}_3(0001)$ : side view (a) & top view (b) [49]

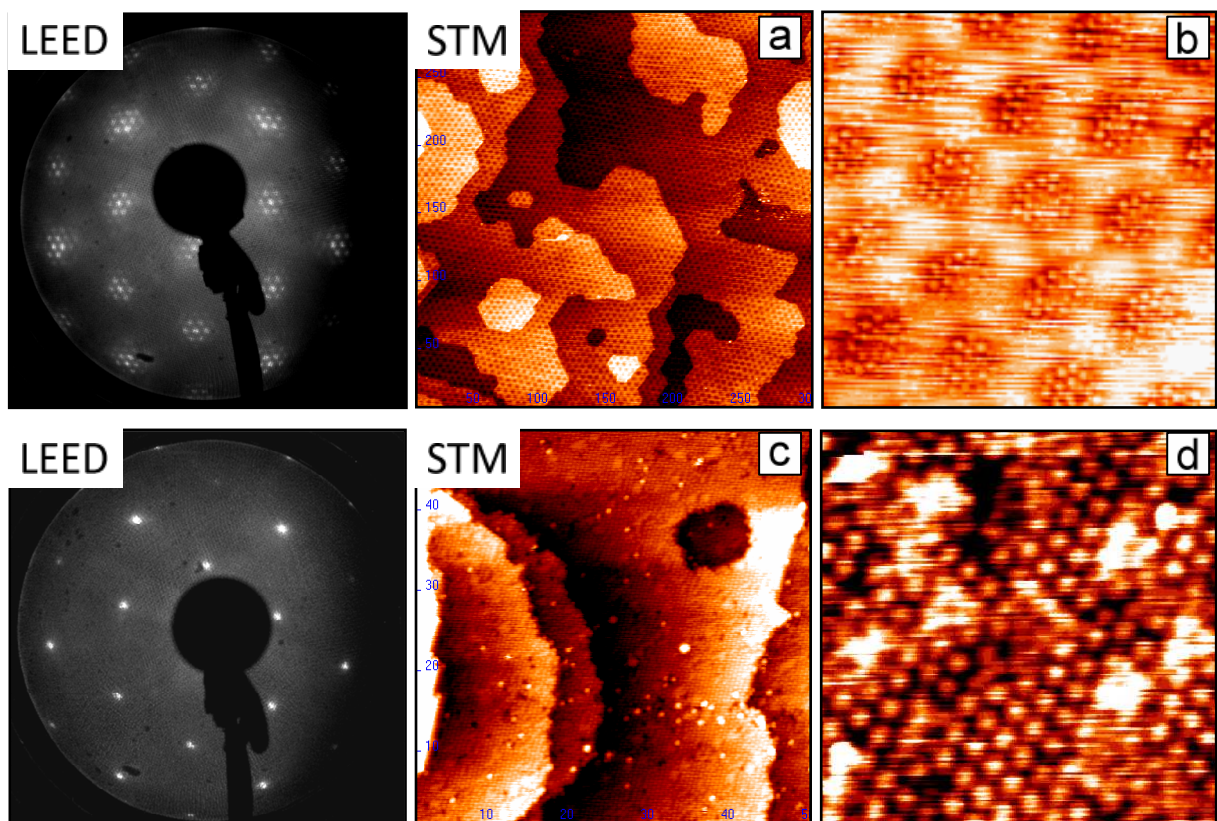


**Fig. 1.15**  $\alpha\text{-Fe}_2\text{O}_3(0001)$  / Pt(111): LEED patterns & STM images; the “biphase”- (top) and the (1x1)- (bottom) (LEED: 64 eV; STM: 300 x 300 nm<sup>2</sup>, 1.4 V, 1.0 nA (a); 20 x 20 nm<sup>2</sup>, 1.4 V, 0.7 nA (b); 50 x 50 nm<sup>2</sup>, 1.4 V, 0.7 nA (c) and 8 x 8 nm<sup>2</sup>; 1.4 V, 0.7 nA (d))

## Chapter 2

### Experimental

#### 2.1 Apparatus

The experiments were performed in Ultra-High Vacuum (UHV) chamber made by Omicron GmbH and modified at Fritz-Haber-Institut, Berlin. UHV means a pressure lower than  $10^{-9}$  mbar (millibar). In that pressure range the influence of the residual gases, which are present in the chamber, on the experimental results can be ignored. The experimental setup consisted of three chambers: the “*main chamber*” (sample preparation chamber), the “*STM chamber*” and the *high pressure cell* (“*HP cell*”). In addition, the *gas line system* was connected to all the chambers. Manipulators of different type were cross-mounted to move the sample between the chambers, these were: main manipulator to position the sample in the main chamber, magnetic transfer rod to transfer the sample between the main chamber and the high pressure cell, and the wobble stick to move the sample between the main chamber and the STM chamber. Two rotary pumps (*BOC Edwards*) were used to maintain the initial vacuum in the whole system. Two turbomolecular pumps (big one and small one, *Pfeiffer Vacuum*) and heating the chamber to  $150^{\circ}\text{C}$  for several hours (so called “*baking*”) were used to remove water and other contaminants from the chamber and maintain the UHV regime. In order to keep the pressure lower than  $10^{-9}$  mbar, the big turbopump was used to continuously pump the main chamber and the STM chamber, while the small turbopump was used to pump the high pressure cell and the gas line. In addition, an ion pump (*Varian*) and titanium sublimation pump (TSP, *Varian*), mounted in the main chamber, were used from time to time to improve the vacuum. The base pressure in the main chamber and in the STM chamber during the experiments was in the  $10^{-10}$  mbar range as measured by high quality pressure gauges, such as the ion gauge (*Omicron*), MKS Baratron<sup>®</sup> gauge (*MKS Instruments*) and cold cathode gauges (*Varian*). The base pressure in the high pressure cell was in the  $10^{-8}$  mbar range (measured by cold cathode).

The *main chamber* was made in a form of a sphere with the main manipulator mounted on the horizontal diagonal of the sphere (Fig. 2.1). The sample, which was a Pt(111) single crystal (platinum cut along (111) crystallographic direction; purity: 99.95 %, *MaTeck*), was spot-welded to a platinum sample holder (home-made in a shape of a standard Omicron sample holder) using Pt wires and inserted into the main manipulator (Fig. 2.2). All the crystals used had a shape of a circle with a diameter of  $\sim 10$  mm and thickness of  $\sim 1.5$  mm. Prior to mounting, the crystals were polished and cleaned with ethanol in a supersonic bath.

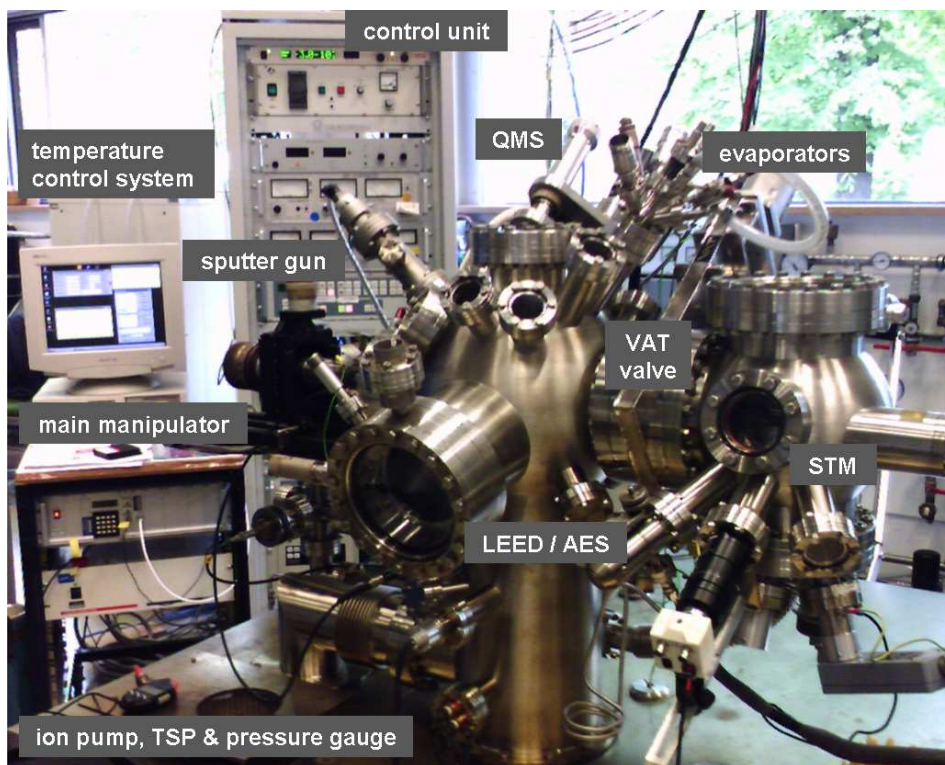


**Fig. 2.1** The main experimental UHV chamber

The sample stage was made of ceramics (alumina) in order to avoid sample contamination. The ceramics were placed on a copper block cooled with air which prevented the sample stage to get hot during sample heating and allowed sample cooling. The air was supplied through a special metal coil connected to the outside of the chamber. For sample cooling to low temperatures ( $< RT$ ) the air could be replaced with nitrogen cooled with liquid nitrogen which allowed reaching sample temperature of  $\sim 100$  K. Holding clips, made of molybdenum, prevented the sample from moving. Thermocouple connection (NiCr and NiAl clips; type K)

was used to read the sample temperature (in Kelvin, [K]). The thermocouple clips were mounted both on the sample holder and on the main manipulator. The sample could be heated up to 1300 K by radiation and electron bombardment from the back side by applying current and high voltage to the tungsten filament. A temperature control system (*Schlichting Physical Instruments*) allowed to keep the heating rate constant.

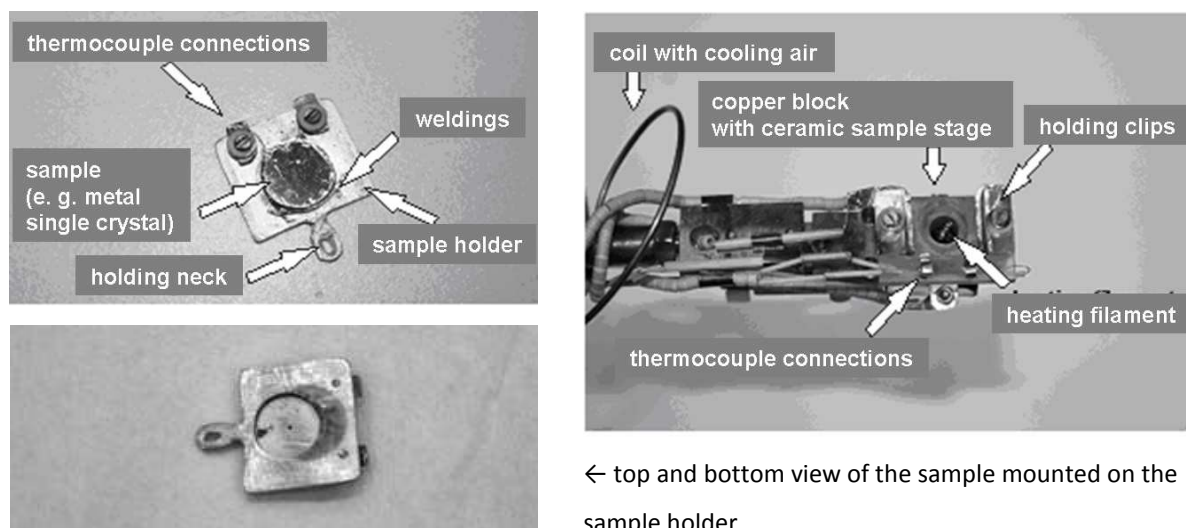


**Fig. 2.2** Single crystal mounted on the sample holder (left) & the sample stage on the main manipulator (right)

The main manipulator could be moved in  $x$ ,  $y$  and  $z$  directions with respect to the horizontal diagonal of the main chamber. In that way the sample could be positioned at any point on the diagonal and close to the diagonal. Additional control of the manipulator's rotation angle ( $\phi$ ) gave opportunity to position the sample so that it could face almost any of the main chamber's-sphere points. The scientific instruments and chamber windows were mounted on different points of the sphere in a way that all of them were pointing near the horizontal diagonal. The chamber was equipped with state-of-the-art sample cleaning, preparation and quality-check instruments: sputter gun (bombardment with  $\text{Ar}^+$  ions, *Omicron*), three Physical Vapor Deposition (PVD) evaporators (EFM3, *Omicron*) which allowed the deposition of metals (Fe and Pt by electron bombardment heating of high purity metal rods and Au by heating the material located in a crucible container; materials purity: 99.95 %, *Goodfellow*), Low Energy Electron Diffraction (LEED, *SPECS*) equipped with a photo camera for recording

the acquired patterns, Auger Electron Spectroscopy (AES, *SPECS*) and a differentially pumped Quadruple Mass Spectrometer (QMS, *VG*) for Residential Gas Analysis (RGA) and Temperature Programmed Desorption (TPD) studies. The AES and TPD data were processed using Origin software (*OriginLab*).

The *STM chamber* was directly connected to the main chamber (see Fig. 2.1). It was possible to separate them using a standard *VAT* valve in order to perform in-situ high pressure STM studies. Separate pressure reading gauges (cold cathode, Baratron<sup>®</sup>) and gas inlet system were provided. The microscope (Fig. 2.3) was Omicron GmbH MICRO H high pressure STM working in constant current mode under the operation of SCALA Pro 5.0 software. The tip was Pt-Ir (*LOT-Oriel GmbH*). The sample was inserted upside-down into the STM and the tip was approaching the sample from the bottom. The sample stage was placed on three ball-bearing piezo carriers which allowed the stage / sample movement in x and y directions. A tube geometry piezoelement was responsible for precise adjustment of the tip z position and for the tip scanning x / y movement.

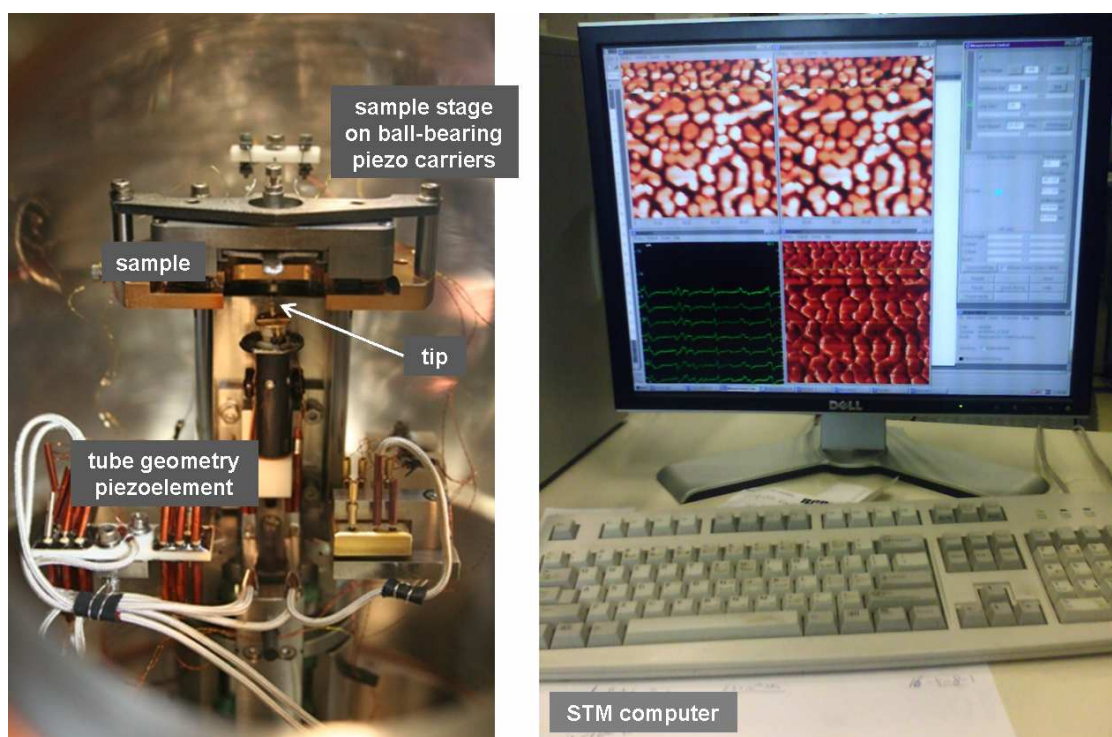


**Fig. 2.3** Omicron MICRO H STM (left) & measuring computer with SCALA PRO software (right)



Data processing was performed using SCALA Pro 5.0, WSxM [55] and Gwyddion [56] PC computer programs. The whole experimental chamber (main chamber, STM chamber, HP cell) was placed on electronic vibration isolation system (*Herzan*) in order to reduce the influence of mechanical noise on STM measurements.

The *high pressure cell* (Fig. 2.4) was constructed for sample treatment in reaction conditions. Sample stage, similar to that on the main manipulator, was made from ceramics (alumina) and titanium in order to avoid sample contamination. Gas inlet and pumping valves were located below and above the sample stage, respectively. The pressure reading instruments (cold cathode, Baratron®) were located in various positions. Heating was provided by a commercial 150 W halogen lamp (*OSRAM*) mounted under the sample stage. The walls of the high pressure cell were cooled by water running through a special metal coil wrapped around the cell from the outside. The reaction time was measured by a commercial stopwatch. Gas composition in the HP cell could be monitored at any time due to direct connection to QMS.

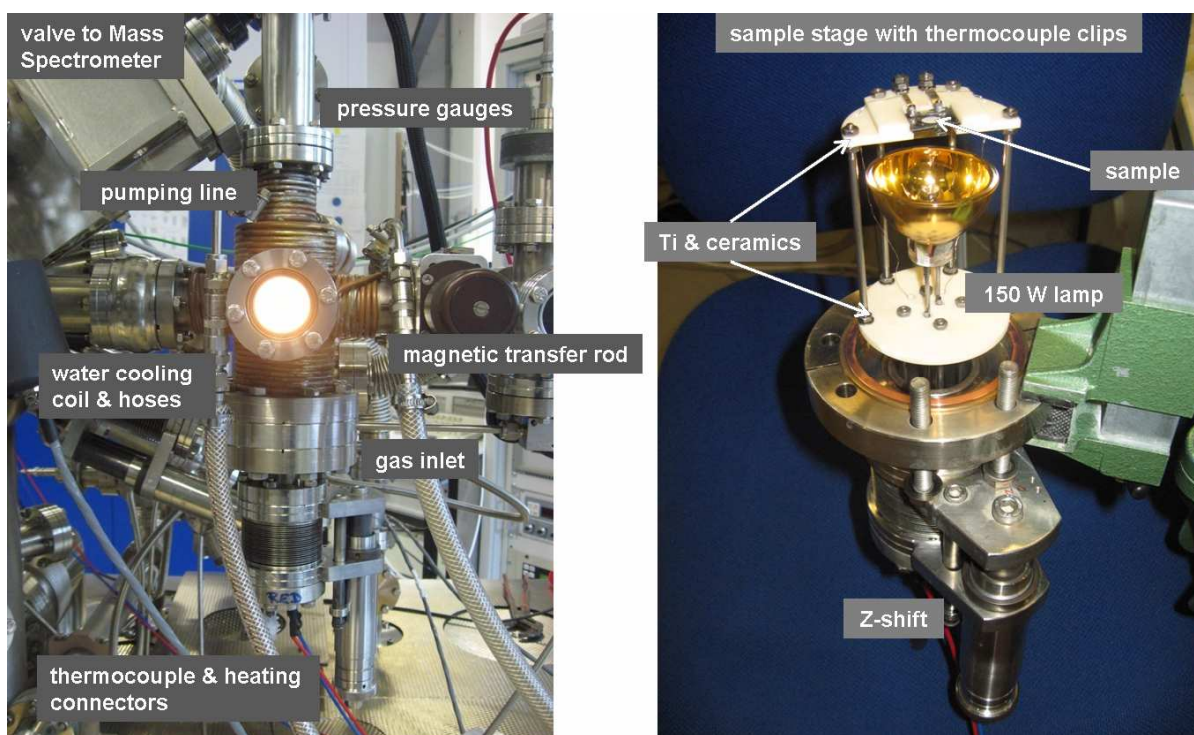


**Fig. 2.4** The high pressure cell: side view (left) & the sample stage of the high pressure cell (right)

The *gas line system* (Fig. 2.5) consisted of high purity (> 99.9 %) gas bottles (Ar (*Linde Gas*), O<sub>2</sub> (*AGA GmbH*), CO (*Linde Gas*), NO (*Messer*), H<sub>2</sub> (*Linde Gas*) and He (*Westfalen*)), gas mixing volume, pressure reading gauges (cold cathode, Baratron®), gas connections to all the experimental chambers and direct pumping connection to turbo- and rotary pumps. One of the connections to the main chamber was made through a directional gas doser. O<sub>2</sub>, CO and NO were cleaned by alcohol-based cold traps (ethanol kept at constant temperature of -120°C). CO was additionally cleaned by a special filter. H<sub>2</sub> was cleaned using liquid nitrogen cold trap.

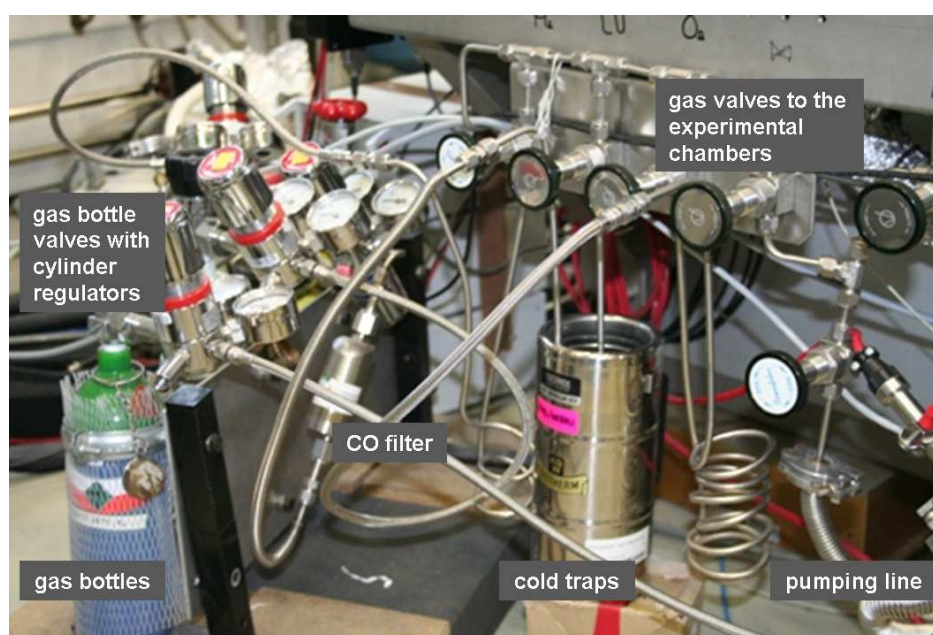


**Fig. 2.5** The gas line system

*Reactivity experiments* were performed by Yingna Sun in a separate UHV chamber (for details please refer to [57]). The chamber was equipped with similar sample cleaning, preparation and quality-check instruments (sputter gun, evaporators, LEED, AES, QMS, temperature control system) and a gas line system (Ar, O<sub>2</sub>, CO, NO, H<sub>2</sub>, He). The sample was spot-welded to the manipulator and heated resistively. It was possible to cool the sample to ~100 K by filling the manipulator with liquid nitrogen. The temperature was measured using type K thermocouple. The main part of the chamber was a high pressure cell connected to Gas Chromatography (GC, *Agilent*) system for reactivity measurements.

## 2.2 Methods:

### 2.2.1 Scanning Tunneling Microscopy (STM)

*Scanning Tunneling Microscope (STM)* was invented by Gerd Binnig and Heinrich Rohrer at IBM Zürich in 1981 [58, 59]. The discovery was awarded the Nobel Prize in Physics in 1986 [60]. The microscope is a part of Scanning Probe Microscopy (SPM) family in which a physical probe scans the surface in an ordered manner, recording the probe-surface interactions (for example the tunneling current in case of STM and van der Waals forces in case of AFM (Atomic Force Microscope)), thus creating an image (topography, current map, etc.) of the surface.

#### Theory: quantum tunneling

The microscope bases on a tunneling effect. Tunneling is a concept that arises from quantum mechanics. In classical mechanics an electron moving in a potential  $U$  can be described by equation [61]:

$$\frac{p_z}{2m} + U(z) = E \quad (5),$$

where  $p_z$  is the electron's momentum,  $m$  is the electron's mass,  $U(z)$  is the potential value at position  $z$  and  $E$  is the electron's energy. The equation is true only for  $E > U(z)$  because only then the electron has a non-zero momentum. It means that the electron cannot move to a region where  $E < U(z)$ . This forbidden region is called the potential barrier. In quantum mechanics any particle, such as the electron, has wave-like characteristics. The state of the particle is described by a wavefunction  $\psi(z)$ . Assuming 1-dimensional case in the presence of a potential  $U(z)$  the energy levels  $\psi_n(z)$  of the electron are given by solutions to Schrödinger's equation [62]:

---

$$-\frac{\hbar^2}{2m} \frac{\partial^2 \psi(z)}{\partial z^2} + U(z)\psi(z) = E\psi(z) \quad (6),$$

where  $\hbar$  is the reduced Planck's constant. In the classically allowed region the solutions are:

$$\psi(z) = \psi(0)e^{\pm i\kappa z} \quad (7),$$

where

$$\kappa = \frac{\sqrt{2m(E - U)}}{\hbar} \quad (8)$$

is the wave vector. In the classically forbidden region quantum mechanics predicts an exponential decaying solution for the electron wave function, which, for a rectangular barrier, has a form of:

$$\psi(z) = \psi(0)e^{\pm \kappa z} \quad (9),$$

where

$$\kappa = \frac{\sqrt{2m(U - E)}}{\hbar} \quad (10)$$

is the decay constant. In special cases the electron can penetrate through the barrier in a process referred to as tunneling. This can take place in case of a very small barrier width, when a bias between two sides of the barrier is applied. Then, for the barrier width  $W$ , there is a finite probability  $P$  to find an electron which moved from  $z=0$  (left edge of barrier) to  $z=W$  (right edge of barrier). The probability is proportional to the wave function squared [61]:

$$P \propto |\psi_n(0)|^2 e^{-2\kappa W} \quad (11),$$

where  $\psi_n$  is a wavefunction of an electron with energy  $E_n$  lying between  $E_f - eV$  and  $E_f$ . Experimentally, the effect can be observed between conductors (for example metals) separated by a very small area of isolator (e.g. vacuum) when a bias  $V$  is applied between the conductors. In STM the effect occurs between the scanning probe ("tip") and the conducting sample. The tip has a form of sharp metal needle. The separating potential barrier is typically an area of vacuum (or air, liquid, etc.). A schematic drawing of a 1-dimensional metal-vacuum-metal tunneling junction on the example of STM is shown in Fig. 2.6:

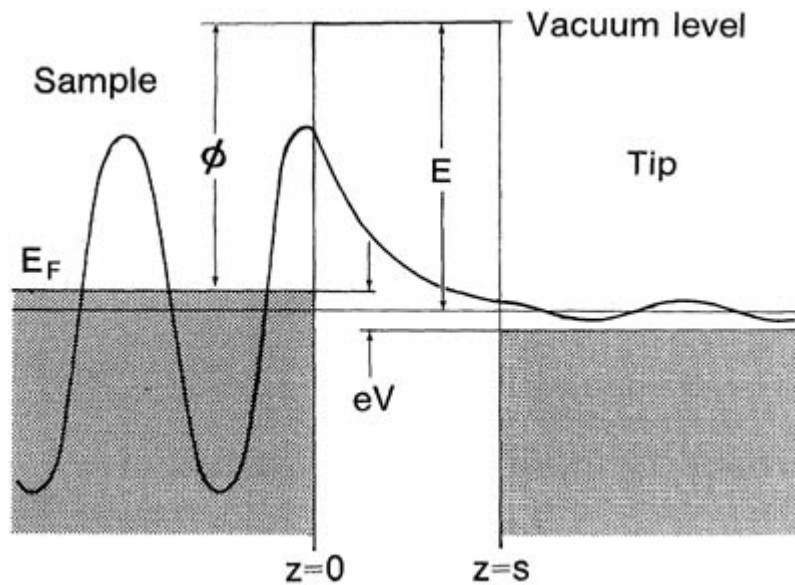


**Fig. 2.6** Schematic drawing of a 1-dimensional metal-vacuum-metal tunneling junction on the example of STM [61]

Tunneling does require that there is an empty energy level of the same energy as the energy of the tunneling electron on the other side of the barrier. Due to that the tunneling current depends not only on the number of electrons between  $E_f - eV$  and  $E_f$  in the tip, but also on the number among them which have corresponding free states to tunnel into on the sample (the tunneling can also occur from the sample to the tip, depending on the voltage's polarity). The higher the density of available states, the greater the tunneling current.

Mathematically the tunneling current can be expressed as the sum of all the electrons which have empty states to tunnel into available [61]:

$$I \propto \sum_{E_F - eV}^{E_F} |\psi_n(0)|^2 e^{-2\kappa W} \quad (12).$$

For very small  $V$  values the density of electronic states does not vary significantly within it and the above given sum can be written in terms of local density of states (LDOS) of the sample near the Fermi level ( $\rho_S(z, E)$ ). The LDOS is the number of electrons per unit volume per unit energy at a given point in space and at a given energy [61]. The local density of states near the energy  $E$  in an interval  $\mathcal{E}$  is given by [63]:

$$\rho_S(z, E) = \frac{1}{\mathcal{E}} \sum_{E-\mathcal{E}}^E |\psi_n(z)|^2 \quad (13),$$

where  $z$  is the point in space. The tunneling current can be then written as:

$$I \propto V \rho_S(0, E_f) e^{-2\kappa W} \approx V \rho_S(0, E_f) e^{-1.025\sqrt{\phi}W} \quad (14),$$

where the barrier height  $\Phi$  can be roughly approximated as:

$$\phi = \frac{1}{2} (\phi_{tip} + \phi_{sample}) \quad (15),$$

which is an average of the tip's and sample's workfunctions given in eV. However, the tunneling current value does not only depend on the LDOS but also on the barrier's width (the distance between the tip and the sample). Therefore, it can be written that [62]:

$$I \propto V \rho_S(W, E_F) \quad (16),$$

which means that the tunneling current is proportional to the local density of states of the sample at the Fermi level  $E_F$ , at a tip-sample distance  $W$ . The width of the barrier is in a size of few Å. For a typical barrier height of 5 eV, which corresponds to the work function of Au (gold), the tunneling current decays by an order of magnitude for the vacuum gap change of 1 Å [64]. This results in a very high vertical (depth) resolution of the STM which is in a range of 0.01 nm.

### The microscope

A schematic drawing of Scanning Tunneling Microscope (STM) is shown in Fig. 2.7:

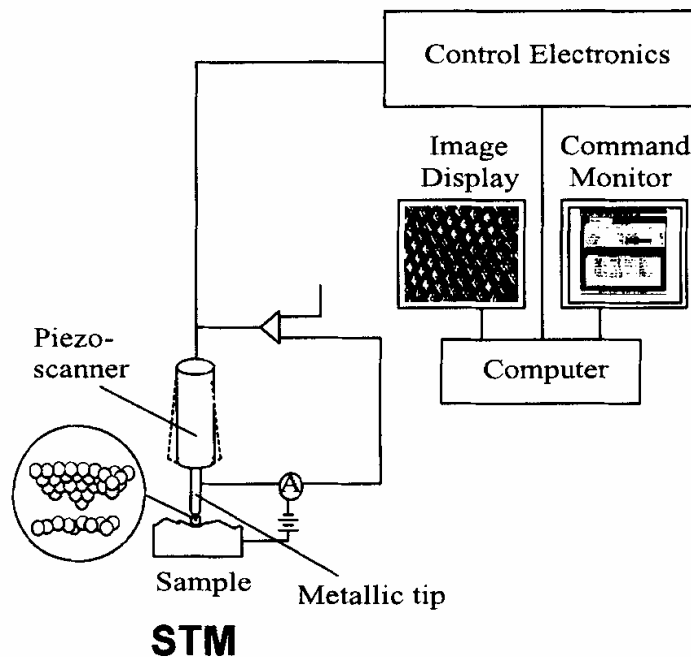


**Fig. 2.7** Schematic drawing of a Scanning Tunneling Microscope (STM) [65]

The working principle is as follows: the tip, usually made of W or Pt-Ir alloy wire (cut and / or electrochemically etched), is being approached to the sample in a distance of 0.5-1 nm and a voltage, typically of few mV up to few V, is applied between them. Because of very small distance and the applied potential difference, the electrons can tunnel from the tip to the sample (or vice versa, depending on the voltage's polarity), which results in a flow of

tunneling current. The tip is attached to a scanner made of piezoelectric elements (ferroelectrics with perovskite structure  $ABO_3$ , for example  $PbTiO_3$ ). The specificity of these materials is that the length of the element changes, if voltage is applied to its walls (due to polarization of the dipoles inside the material). By adjusting the voltage on the piezo element, the distance between the tip and the sample can be adjusted (the tip z position). The combination of three piezo elements makes it possible to move the STM tip also in x and y directions. This kind of tip position control results in a very high lateral resolution of 0.1 nm. Most modern STMs use tube geometry piezo elements with one inner electrode and four outer. If the voltage is applied to the inner and outer electrodes, the length of the element is changed. If the voltage is applied to the opposite outer electrodes, the element is bended. Typical piezo elements used in STMs are shown in Fig. 2.8:

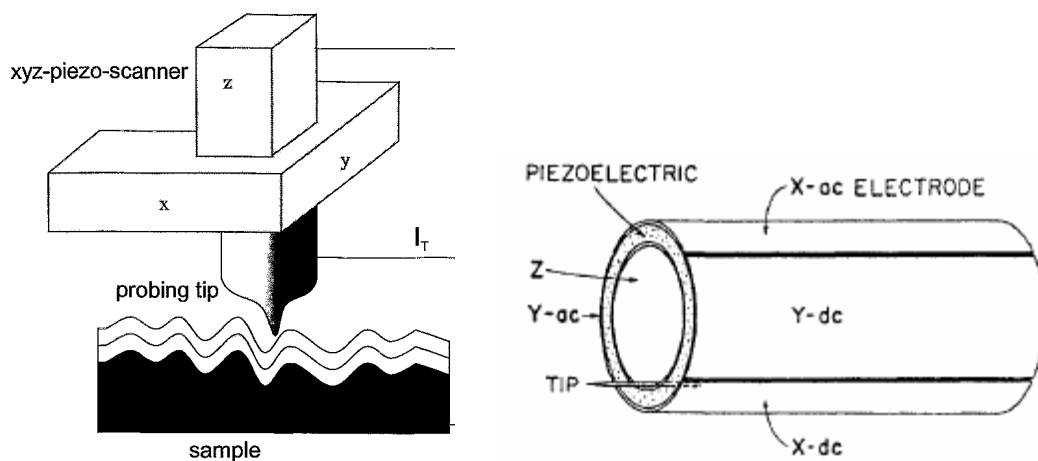


**Fig. 2.8** Typical piezo elements used in STMs: combination of three elements (left) [64] & tube geometry (right) [66]

The tip moves across the sample's surface in the x-y plane. The changes in surface height (and the corresponding tip-sample distance), as well as the changes in the density of electron states in different regions of the sample, result in changes in the tunneling current [63].



Scanning tunneling microscopes typically operate in one of two modes:

In *constant current mode* the deviations of the tunneling current with respect to the preset value are continuously measured and the feedback electronics adjust the tip's  $z$  position (tip-surface distance) to keep the tunneling current value constant. The changes in the  $z$  and the deviations of the tunneling current are being recorded by a computer. In that way a topographic image of the surface, as well as the corresponding current map, are created.

In *constant height mode* the scanner moves the tip in plane only, so that the changes in the tunneling current visualize the sample relief. This mode can be only applied if the sample's surface is very flat (high surface corrugation would cause tip crash).

The acquired data is being saved by a computer in a form of a raster image with a typical resolution of 256 x 256 or 512 x 512 pixels (measurement points). The image is created in a line-by-line manner, with a scanning direction up or down, from left to right or from right to left. Very important thing are the tunneling parameters. These are the scanning parameters which are controlled by the user. The operation is performed on the STM measuring computer running special software. The *gap voltage* ( $V$ ; in [V]) sets the voltage bias which is applied between the tip and the sample and gives possibility to define the direction of the tunneling current flow (negative vs. positive voltage values). The *tunneling current feedback setpoint* ( $I$ ; in [nA]) allows the definition of the tunneling current setpoint for the feedback loop. The *scan area*, which is in a form of a square, can be defined in [nm]. The acquired STM images can be processed using computer software (applying image filters, measuring the distances, height profiles, performing statistical analyses, performing Fast Fourier Transform (FFT), etc). Typical STM images (topography image & the corresponding current image) are shown in Fig. 2.9:

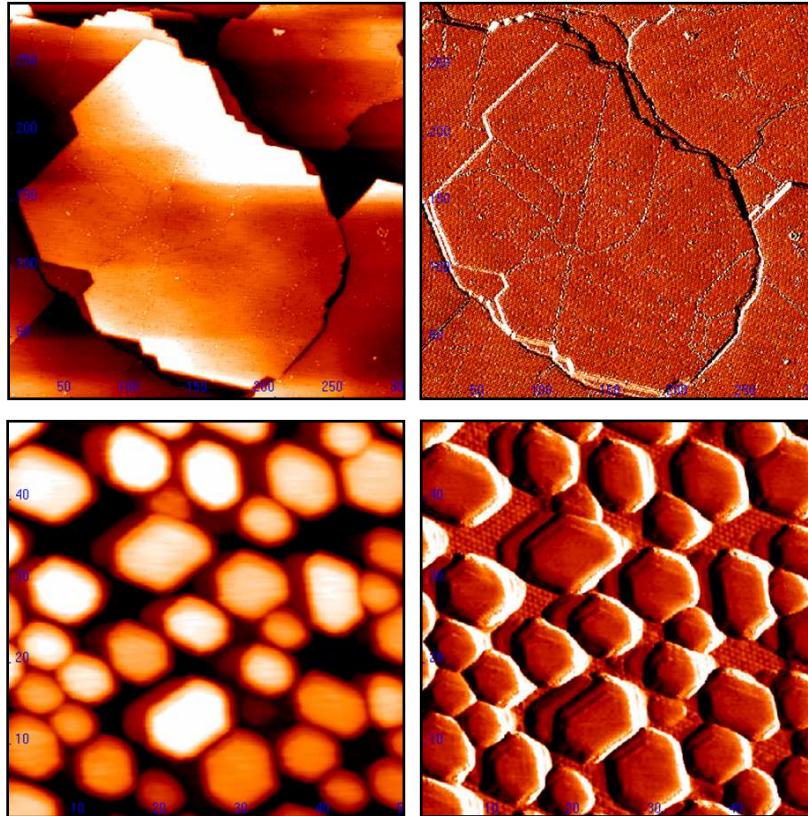


**Fig. 2.9** Typical STM images: topography (left) & current (right)  
(samples: Fe<sub>3</sub>O<sub>4</sub>(111) / Pt(111) (top) and Pt / Fe<sub>3</sub>O<sub>4</sub>(111) / Pt(111) (bottom);  
STM: 300 x 300 nm<sup>2</sup>, 1.4 V, 0.7 nA (top) and 50 x 50 nm<sup>2</sup>, 1.4 V, 0.7 nA (bottom))

### 2.2.2 Low Energy Electron Diffraction (LEED)

*Low Energy Electron Diffraction (LEED)* is an experimental technique which bases on the wave-like nature of electrons and the associated effects: diffraction and interference. It allows to distinguish different crystal structures by monitoring the angular dependence of the electrons which are backscattered from the atoms in the crystal.

#### **Theory: wave-like nature of particles**

In 1924 Louis de Broglie in his PhD thesis formulated a theory that every moving particle has a wave-like nature. This means that the particles, e.g. the electrons, undergo the effects associated with waves, such as diffraction or interference. The hypothesis, based on

Albert Einstein's and Max Planck's works, was awarded the Nobel Price in Physics in 1929 [67]. De Broglie's theoretical work started a series of experiments on particles diffraction and interference. In 1927 Davisson and Germer discovered that a monochromatic beam of low energy electrons shot onto a crystal surface is elastically backscattered on the high electron density regions, namely the surface atoms, and the intensity of the backscattered electrons have an angular dependence, forming a diffraction pattern [68].

The theoretical explanation for the formation of diffraction patterns from crystal structures is as follows: Coming from de Broglie's equation for the electron's wavelength, the wavelength's dependence on the electron's kinetic energy (determined by the electron beam energy) can be derived:

$$\lambda = \frac{\hbar}{p} = \frac{\hbar}{\sqrt{2mE_k}} = \frac{\hbar}{\sqrt{2meV}} \quad (17),$$

where  $\lambda$  is the wavelength,  $\hbar$  is the Planck's constant,  $p$  is the electron's momentum,  $E_k$  is the electron's kinetic energy,  $m$  is the electron mass,  $e$  is the electron charge and  $V$  is the beam energy. This means that a beam of low energy electrons ( $V = 10\text{-}200\text{ eV}$ ) results in a small wavelength  $\lambda$  which is of a size of interatomic distances in a crystal lattice ( $< 3\text{ \AA}$ ). The process of electron scattering at the crystal surface is schematically shown in Fig. 2.10. The elastically scattered electrons undergo a constructive interference following the Bragg's law if the path difference between the electrons coming from different atoms is equal to the multiplicity of the wavelength [69]:

$$2d \sin \theta = n\lambda \quad (18),$$

where  $d$  is the interplanar distance in the crystal lattice,  $\theta$  is the angle between the beam and the sample plane,  $n$  is an integer and  $\lambda$  is the wavelength. Due to different interatomic and interplanar distances in different crystalline materials, the electron diffraction patterns are characteristic for a specific crystallographic structure and can be used to distinguish the structures. That is how an experimental technique called Low Energy Electron Diffraction

(LEED) was born.

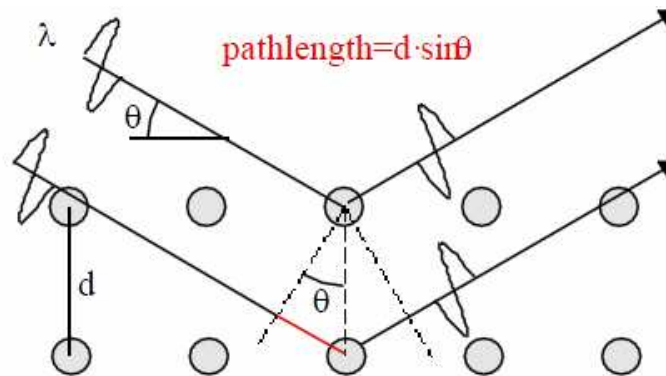


**Fig. 2.10** Schematic drawing of electron scattering at the crystal surface [70]

Sharp and uniform diffraction patterns can be archived only from high-symmetry regions of the surface (crystals, highly organized adsorbates). Due to a low energy of the electrons only the first few atomic layers of the sample are penetrated, before the electron loses its energy due to inelastic events (the penetration distance is called the inelastic mean free path). UHV conditions are highly demanded for electron diffraction experiments because in air the electrons can be scattered on gas-phase molecules before reaching the surface. Due to this for many years LEED was not considered as a useful experimental technique. With a development of vacuum surface science, electron-based surface sensitive tools, such as LEED, became popular.

### The diffractometer

A schematic drawing of Low Energy Electron Diffractometer (LEED) is shown in Fig. 2.11. The working principle of LEED is as follows: the sample is placed in front of the filament (cathode; so called electron gun). The current is applied to the filament which results in emission of electrons with given energy. The electrons are accelerated towards the sample and the beam hits the sample surface. The sample is grounded in order to prevent charging. The electrons are scattered on the surface atoms and the backscattered electrons are collected on a hemispherical fluorescent screen causing illumination. High voltage (~6000

eV) is applied to the screen in order to accelerate the electrons towards it. A diffraction pattern is formed which can be observed directly (by eye) or recorded with a photo camera.

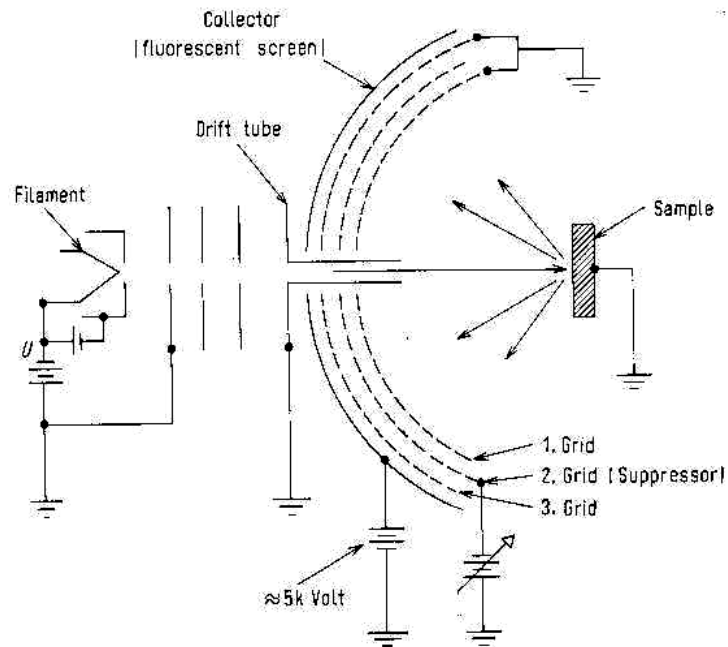


**Fig. 2.11** Schematic drawing of a Low Energy Electron Diffractometer (LEED) [71]

The LEED patterns are in a form of bright diffraction spots on a dark background. The positions and distances between the spots are characteristic for a specific crystallographic structure and the intensities of the spots and the background reflect the quality of the structure. It is important to note that the observed pattern is a reciprocal space representation and not a real space image of the crystal structure. The spots are named in a matrix notation with respect to the middle spot (so called [00] spot): [01], [10], [-11], etc. A typical LEED image is shown in Fig. 2.12. Only the elastically scattered electrons contribute to the pattern. In order to eliminate the inelastically scattered electrons (which contribute to the background illumination of the screen and weaken the pattern), a system of grids with a retarding potential is positioned on the electrons way to the screen so that only the electrons with a given energy can pass the grids.

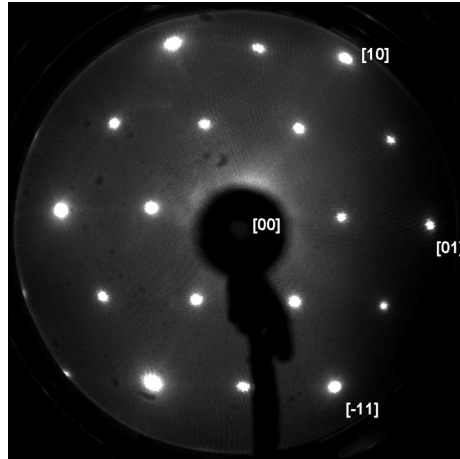


**Fig. 2.12** A typical LEED image  
(sample:  $\text{Fe}_3\text{O}_4(111)$  /  $\text{Pt}(111)$ ; LEED: 90 eV)

### 2.2.3 Auger Electron Spectroscopy (AES)

*Auger Electron Spectroscopy (AES)* is an experimental technique which bases on the so called Auger effect. The technique allows the determination of chemical composition of the sample's surface by investigating the energies of the Auger electrons emitted from the sample upon electron bombardment.

#### Theory: Auger effect

The Auger effect was discovered by Lise Meitner and Pierre Auger independently [72, 73]. It was first described by Meitner in 1922, however, Pierre Auger was a scientist who was mostly credited for it. The discovery was that exciting an atom by removing an electron from one of the atom's core shells, forces an electron from the closest outer shell to fill the remaining hole and the energy difference from the transition to a lower energy level causes an electron from the second closest outer shell to be emitted from the atom. This emitted electron is called the Auger electron. Graphical illustration of the Auger effect is shown in Fig. 2.13:

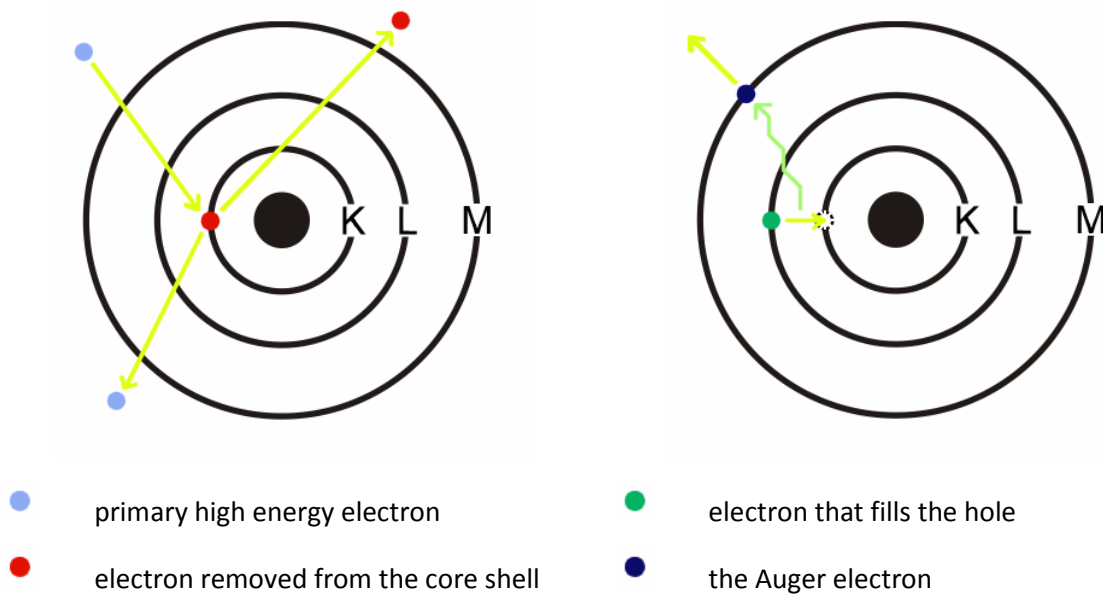


**Fig. 2.13** Graphical illustration of the Auger effect

The kinetic energy of the Auger electron is given by equation:

$$E_k = E_{core} - E_{1st-outer} - E_{2nd-outer} \quad (19),$$

where  $E_{core}$  is the binding energy of the electron removed from the core shell,  $E_{1st-outer}$  is the energy of the electron which fills the hole and  $E_{2nd-outer}$  is the binding energy of the emitted Auger electron. The energies of the Auger electrons are in the range of 50 to 3000 eV and are characteristic for atoms of a specific element due to unique orbital energies. This allows spectroscopic investigation of the material which is in the basis of the Auger Electron Spectroscopy (AES). UHV conditions are necessary in order to avoid electron scattering on the gas phase molecules and to prevent their adsorption on the sample's surface. That is why, similarly to LEED, AES became popular in 1950s with a development of vacuum surface science.

## The spectrometer

The AES often bases on the same setup as LEED. Electron gun is placed in front of the sample and current is applied to the filament. Emitted electrons hit the sample initiating the Auger process. A set of grids with a retarding potential allows only the Auger electrons with a given energy to pass to the detector. The potential increases in steps, for example 1 eV / 1 sec, which allows to collect all the electrons with energies in a given range. The electrons are collected by a cylindrical mirror analyzer. The multiplier strengthens the signal which is then recorded by a computer in a form of energy vs. Auger electron intensity plot (derivative). The energies of the Auger electrons emitted from different elements are unique so the chemical composition of the surface can be determined from the acquired spectrum. The technique is surface sensitive due to low energy of the electrons (short mean free path). A typical AES spectrum is shown in Fig. 2.14:

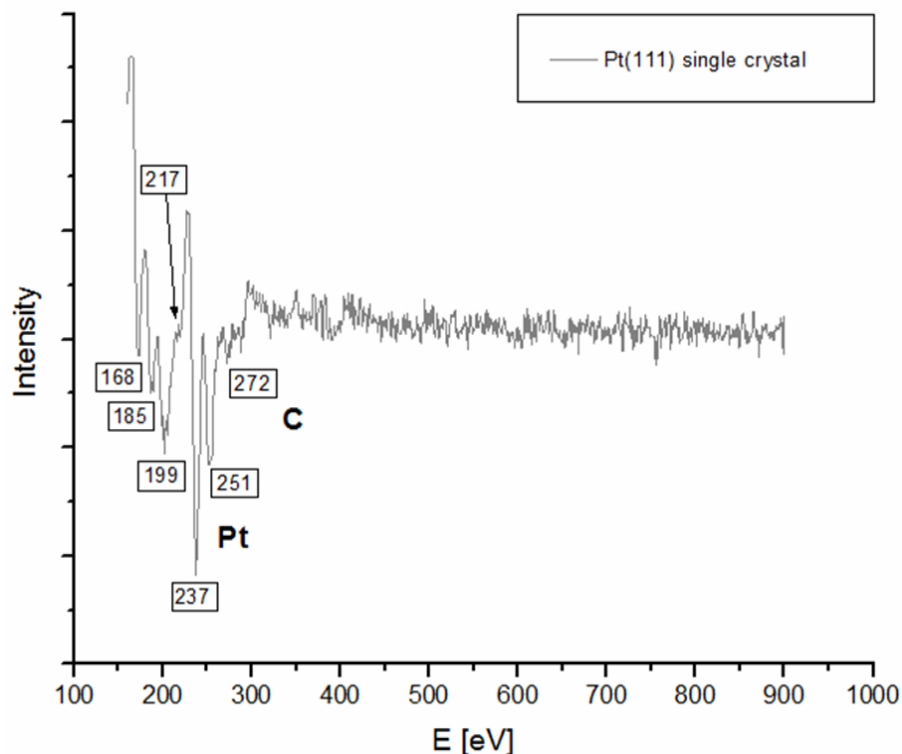


**Fig. 2.14** A typical AES spectrum  
(sample: Pt(111) single crystal contaminated with carbon)



### 2.2.4 Temperature Programmed Desorption (TPD)

*Temperature Programmed Desorption (TPD)*, also called Thermal Desorption Spectroscopy (TDS), is an experimental technique based on mass spectrometry, that allows analysis of atoms and molecules which desorb from the surface upon linear temperature increase. It provides qualitative and quantitative information on the adsorbates, such as their atomic masses, bonding energies and the amount. Alternatively, the sample can be exposed to a certain gas, for example CO, which acts as a probe molecule that helps to determine the adsorption properties of the sample and thus provides information on sample's morphology. The technique also allows the analysis of chemical composition of the surface itself, however, it is a destructive method because it involves thermal decomposition.

### Mass Spectrometry

Every atom has an atomic mass which is given in atomic mass units (amu) [74]. Similarly, every molecule has an atomic mass which is the sum of the atomic masses of atoms which form the molecule. The instrument which is able to detect the atomic masses of gas phase / vaporized atoms and molecules is called Mass Spectrometer (J. J. Thompson, 1911). The working principle is based on the ionization of atoms by electrons emitted from the cathode in the ionizer, separation of ions by mass-to-charge ( $m/e$ ) ratio in electric and magnetic fields and detection of ions in the detector. The signal is recorded by a computer in the form of intensity vs. mass-to-charge ratio spectrum. The analysis provides qualitative (chemical composition), as well as quantitative (amount of a given chemical compound, ratio between different compounds) information [75]. There are different types of Mass Spectrometers. One of the most commonly used is the Quadrupole Mass Spectrometer (QMS), where the ion separation system consists of four parallel metal rods. The rods are connected in pairs and voltages (+) and (-) are applied to these pairs. Because of the applied voltages, an electric field is formed between the rods and, depending on the voltages, only ions with certain mass-to-charge ratio will be able to pass the rods and reach the detector. A schematic drawing of Quadrupole Mass Spectrometer is given in Fig. 2.15. The QMS can

---

operate in two modes: the Residual Gas Analysis (RGA) mode which allows real-time identification of gas phase atoms and molecules which are present in the system and, in combination with a temperature control system, the Temperature Programmed Desorption (TPD) mode which allows studies of adsorption / desorption processes on surfaces. For TPD measurements UHV conditions are necessary.

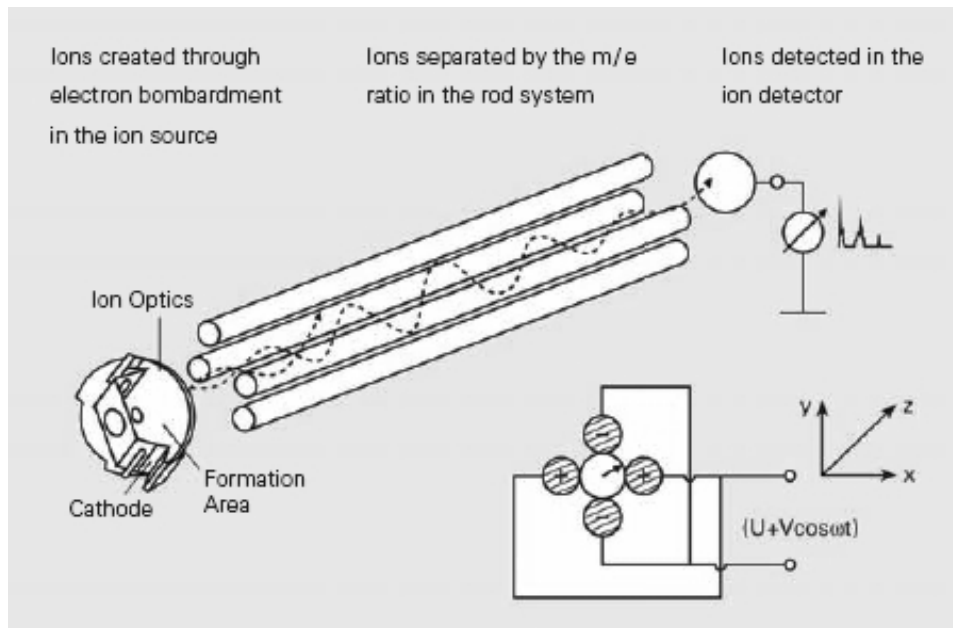


**Fig. 2.15** Schematic drawing of a Quadrupole Mass Spectrometer (QMS) [76]

### Adsorption / desorption processes

Atoms and molecules can adsorb on the surface from the gas phase and bind through chemical bonds. To desorb the adsorbates a sufficient energy has to be supplied to the system in order to break the bonds. This can be done by heating. Because the energy of the bonds depends both on the nature of the adsorbate and the surface, different adsorbates desorb from different surfaces at different temperatures. In addition, the position within the substrate where the molecule adsorbs (terrace, step edge, defect, etc.) plays an important role. Adsorption of molecules on surfaces can be described by the Langmuir model [77] in which the molecules adsorb on empty sites on the surface and the relative coverage  $\theta$  is defined as the ratio between occupied and available surface sites. The molecule can adsorb

on the surface directly (first-order process) or the adsorption can be accompanied by molecule's dissociation (second-order). Sufficient energy is necessary for the molecule to adsorb (the energy of chemical bonds creation). This energy is called the activation energy of adsorption  $E_a$ . The adsorption energy is even higher in case of the adsorption accompanied by molecule's dissociation, because it includes additional activation energy of dissociation. An energy necessary to desorb the molecule is called the activation energy of desorption  $E_d$  and equals the energy of adsorption (or adsorption + dissociation). Again, a molecule can desorb from the surface directly (first-order process), or two atoms or molecules from neighbouring sites may form a molecule and desorb together (second-order). The desorption rate  $r$ , defined as the number of molecules desorbing in time, is given by the Polanyi-Wigner equation [78]:

$$r = -\frac{d\theta}{dt} = \nu\theta^n e^{-E_d/RT} \quad (20),$$

where  $R$  is the gas constant,  $T$  is the temperature,  $t$  is the time and  $\nu$  is the pre-exponential Arrhenius factor. For the first-order process the desorption rate is proportional to the initial coverage  $\theta$  ( $n = 1$ ) and for the second-order to the  $\theta^2$  ( $n = 2$ ). For the zero-order desorption ( $n = 0$ ), which is a special case for multilayers of adsorbates, the desorption rate does not depend on the initial coverage at all.

## TPD

The sample is positioned in front of a differentially pumped Mass Spectrometer and heated with a constant heating rate (e.g. a ramp of 3 K/s). At certain temperatures certain adsorbates desorb to the gas phase. The desorbing species are monitored by MS. The computer records the spectrum of a given atomic mass as a function of sample's temperature. Several different masses can be monitored simultaneously. In case of probe molecule desorption studies, the sample is positioned in front of the directional gas doser and exposed to the probe gas before positioning in front of the MS. A typical TPD spectrum of CO adsorbed ("CO TPD"), showing two peaks corresponding to desorption from two

energetically different surface sites, is shown in Fig. 2.16:

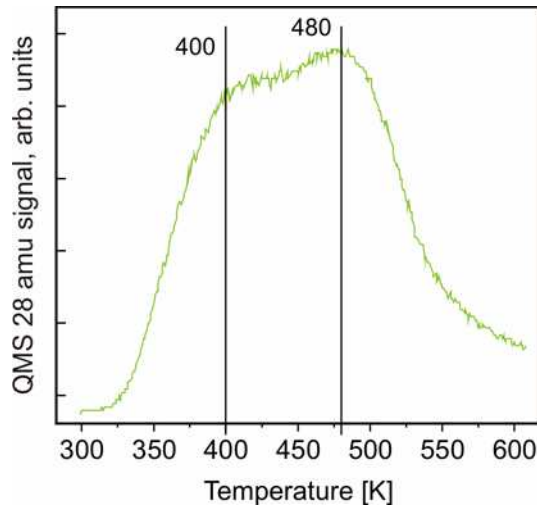


**Fig. 2.16** A typical TPD spectrum of CO adsorbed (sample: Pt / Fe<sub>3</sub>O<sub>4</sub>(111) / Pt(111) flashed to 600 K)

Qualitative data analysis is performed on the basis of the so called Redhead formalism [78, 79]. To measure the desorption rate  $r$  the increase of the partial pressure  $p_{\text{partial}}$  in time has to be monitored. For this, two important conditions have to be fulfilled [77]:

1) Sufficient pumping speed has to be supplied to the system, so that:

$$r = -\frac{d\theta}{dt} \propto p_{\text{partial}} \quad (21),$$

2) The temperature of the sample has to be linearly increased in time. For a constant heating rate the temperature of the sample during heating is given by equation:

$$T = T_0 + \beta t \quad (22),$$

where  $T_0$  is the starting temperature and  $\beta$  is the heating rate. With these assumptions, the Polanyi-Wigner equation (20) will have the form:

$$r = -\frac{d\theta}{dt} = \frac{\nu}{\beta} \theta^n e^{-E_d/RT} \quad (23),$$

In practice, what is calculated is the activation energy of desorption  $E_d$  which, in a simplified form, can be written as:

$$E_d = RT_{\max} \left[ \ln \frac{\nu T_{\max}}{\beta} - 3.46 \right] \quad (24),$$

where  $T_{\max}$  is the temperature at which the desorption peak reaches the maximum value. This equation is the most commonly used approximation given by Redhead [78, 79] and is only true for first-order desorption. For higher desorption orders more complicated calculations are necessary. The temperature  $T_{\max}$  as well as other important information about the desorption process can be obtained by analyzing the TPD line. The order of desorption can be deduced from the shape of the desorption curve [78]. For the first-order processes the peaks are asymmetric and the maximum desorption temperature does not depend on the initial coverage (Fig. 2.17(a)). This is typical for non-recombinative desorption. For the second-order processes the peaks are symmetric and the maximum desorption temperature depends on the initial coverage (decreasing with increasing coverage) (Fig. 2.17(b)). This is typical for recombinative desorption.

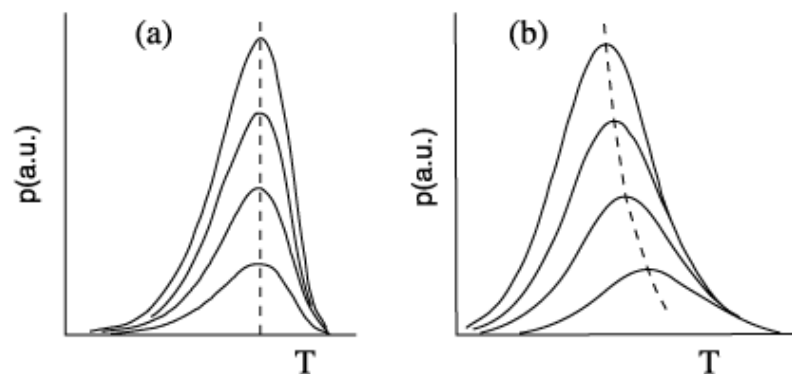


**Fig. 2.17** Typical sets of first- (a) and second-order desorption (b) curves for different initial coverages

[77]

For the zero-order processes the peaks are asymmetric, have the same leading edge independently on coverage, the desorption rate increases exponentially with temperature and the maximum temperature shifts to higher values with increasing coverage (Fig. 2.18). In addition, a dramatic drop in peak's intensity is observed after all the molecules have desorbed from the surface. This is typical for multilayers of adsorbates.

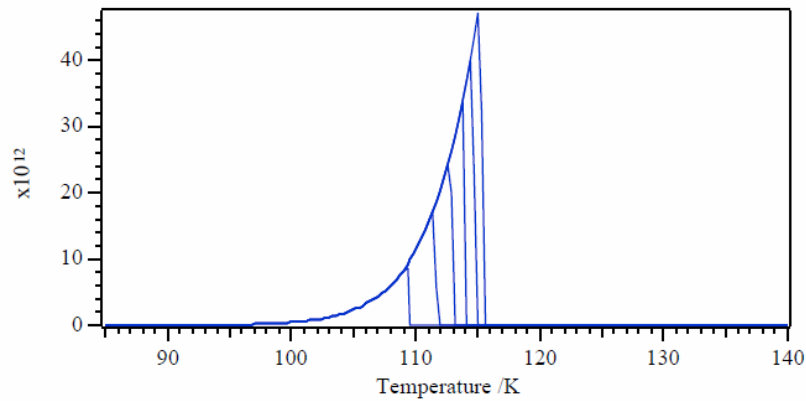


**Fig. 2.18** Typical set of zero-order desorption curves for different initial coverages [70]

The quantitative information is acquired by analyzing the intensity of the desorption signal (area under individual peaks) which corresponds to the amount of desorbing species.

# Chapter 3

## Morphology of Pt nanoparticles on Fe<sub>3</sub>O<sub>4</sub>(111) / Pt(111)

based on published results:

[80] Z.-H. Qin, M. Lewandowski, Y.-N. Sun, S. Shaikhutdinov, and H.-J. Freund, *Encapsulation of Pt Nanoparticles as a Result of Strong Metal-support Interaction with Fe<sub>3</sub>O<sub>4</sub>(111)*, *The Journal of Physical Chemistry C* 112 (2008), p. 10209-10213.

[81] Z.-H. Qin, M. Lewandowski, Y.-N. Sun, S. Shaikhutdinov, and H.-J. Freund, *Morphology and CO adsorption on platinum supported on thin Fe<sub>3</sub>O<sub>4</sub>(111) films*, *Journal of Physics: Condensed Matter* 21 (2009), p. 134019-1-134019-6.

[82] Y.-N. Sun, Z.-H. Qin, M. Lewandowski, S. Shaikhutdinov, and H.-J. Freund, *CO Adsorption and Dissociation on Iron Oxide Supported Pt Particles*, *Surface Science* 603 (2009), p. 3099-3103.

### 3.1 Introduction

Noble metal particles supported on oxide surfaces are well-established systems in catalysis. However, the details of catalytic processes that take place on these systems are often unknown. To gain better understanding of these processes, model studies in UHV conditions are being performed (see [8, 9] and references therein). Among the noble metals most widely used are gold, silver, platinum and palladium. Examples of Pt and Pd particles supported on TiO<sub>2</sub> and CeO<sub>2</sub> were given in Chapter 1.2. As mentioned there, in many cases such systems undergo the so called Strong Metal-Support Interaction (SMSI) which manifests itself by the encapsulation of metal particles by the supporting oxide. Among the variety of oxide supports the studies on iron oxide based model catalysts are quite rare. It was shown that thin (nm thick) iron oxide films can be grown on Pt(111) ([10] and references therein). These films are promising supports for the growth of catalytically active metal particles. The Moiré pattern of FeO(111) film on Pt(111) was found to act as a template for the growth of Au nanoparticles [83]. Pd particles on the same support were shown to diffuse into the film upon annealing at 600 K [84-86]. Au, Ag and Pt particles deposited onto unreconstructed Fe<sub>3</sub>O<sub>4</sub>(111) films (for termination details please refer to Chapter 1.4) were investigated using Reflection High-Energy Electron Diffraction (RHEED) and Transmission Electron Microscopy,

and an epitaxial relationship was found between the deposited metals and the oxide support [87, 88]. Nucleation, growth, thermal stability and reactivity of Pd nanoparticles supported on Fe<sub>3</sub>O<sub>4</sub>(111) were recently studied in Fritz-Haber-Institut, Berlin [89-92]. It was found that an interface oxide layer forms between the particles and the oxide support upon oxidation at 500-550 K. This layer was shown to affect the activity of Pd particles in CO oxidation reaction.

In this chapter we report the results of Pt nanoparticles supported on Fe<sub>3</sub>O<sub>4</sub>(111) films grown on Pt(111). We studied nucleation, growth and thermal stability of the particles using STM in combination with LEED, AES and CO TPD.

### 3.2 Samples preparation

Pt(111) single crystal was sputtered with argon Ar<sup>+</sup> ions with energy of 1 keV using the sputtering current of 24  $\mu$ A. The sputtering was performed for several hours at different temperatures: 300, 500 and 700 K – in cycles of 1 h each. After each sputtering hour the sample was annealed at 1100 K for 5 min in UHV and after the final sputtering cycle it was annealed at 1200 K for 10 min. In that way extended flat Pt(111) terraces were obtained as judged by LEED, STM (Fig. 3.1) and CO TPD. In addition, between some of the sputtering cycles the crystal was oxidized at 800 K in  $1 \times 10^{-6}$  mbar oxygen and subsequently annealed at 1100-1200 K, in order to remove carbon and bulk iron which tends to diffuse into the crystal during iron oxide experiments [93]. The cleanness of the crystal was additionally checked with AES.

The preparation procedure of thin Fe<sub>3</sub>O<sub>4</sub>(111) films on Pt(111) was based on [10] and optimized in our laboratories. First an FeO(111) layer was grown. 1 ML of Fe was deposited onto Pt(111) single crystal. During Fe deposition the sample was always biased with a retarding potential to prevent metal ions from being accelerated towards the sample. Fe coverage was calibrated using STM images and WSxM processing software. 1 ML corresponds here to the amount of iron which would cover the surface entirely with a thickness of a single monatomic layer. The sample was then oxidized in  $1 \times 10^{-6}$  mbar O<sub>2</sub> at 1000 K for 2 min and cooled down in oxygen to T < 500 K in order to avoid the loss of surface oxygen. The quality of the film was checked with LEED and STM. Next, three cycles of 8 ML

---



Fe deposition and oxidation in  $1 \times 10^{-6}$  mbar O<sub>2</sub> at 880 K for 5 min were performed, plus an additional one cycle with final oxidation at 1000 K for 10 min. In that way a few-nanometer-thick Fe<sub>3</sub>O<sub>4</sub>(111) film was grown. Again, for all the oxidation steps the sample was cooled down in O<sub>2</sub> to  $T < 500$  K after the oxidation (except the final oxidation when the oxygen was pumped at  $T = 1000$  K and the sample was cooled down instantly). Prior to experiments, the Fe<sub>3</sub>O<sub>4</sub>(111) films were additionally flashed to 900 K in UHV in order to desorb any molecules that could adsorb from the background pressure of residual gases. A high heating rate ( $> 5$  K/s) was used in order to avoid the loss of surface oxygen. The quality of the films was checked with LEED, AES and STM. For the films prepared in that way a single-terminated surface, which is believed to be the unreconstructed Fe<sub>3</sub>O<sub>4</sub>(111) surface (for termination details please refer to Chapter 1.4), was obtained.

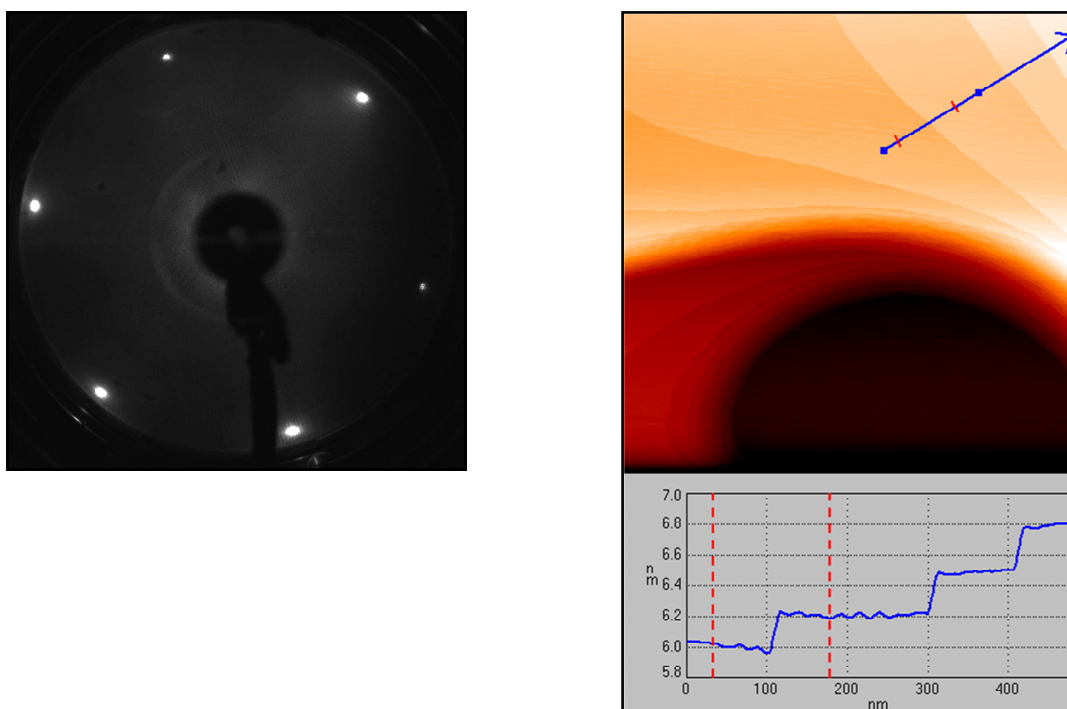


**Fig. 3.1** Pt(111) single crystal: LEED pattern & STM image with profile line showing monatomic steps (LEED: 64 eV; STM:  $1000 \times 1000$  nm<sup>2</sup>, 0.7 V, 0.4 nA)

Pt particles were deposited at  $\sim 100$  K and RT at different coverages. Again, a retarding potential was applied to the samples during depositions. The samples were annealed to different temperatures as described in the experimental section (Chapter 3.3)

and post-characterized using LEED, AES and STM. The deposition rate of Pt, as well as the height of monatomic Pt layer, were calibrated by Pt deposition onto a clean Pt(111) single crystal and STM / WSxM analysis. Pt forms 1 ML thick islands on Pt(111) single crystal which makes an accurate calibration possible.

CO TPD experiments were performed by exposing the samples to CO using a directional gas doser placed in a distance of ~1 mm to the sample and subsequent heating in front of the QMS positioned in a distance at which the spectrometer was almost touching the surface of the sample. In that way any desorption signals coming from the sample holder, thermocouple wires etc. could be neglected. The heating rate was 3 K/s.

### 3.3 Results & Discussion

#### 3.3.1 Nucleation and growth

We studied nucleation and growth of Pt nanoparticles on Fe<sub>3</sub>O<sub>4</sub>(111). The particles were deposited at  $T = \sim 100$  K onto freshly prepared magnetite films and subsequently heated to RT for STM studies. Different coverages studied were: 0.08 ML, 0.6 ML, 1 ML and 2 ML. Pt nucleated randomly on the regular terrace sites of Fe<sub>3</sub>O<sub>4</sub>(111), forming particles of different sizes. There was no nucleation on the step edges observed. For the lowest studied coverage of 0.08 ML most of the particles were  $\sim 3$  Å in height (Fig. 3.2(a)), a value which is quite similar to the height of a single atomic layer of Pt in Pt(111) ( $\sim 2.3$  Å). By increasing the coverage to 0.6 ML the particle density increased, but the average particle size remained unchanged (Fig. 3.2(b)). At the coverage of 1 ML the particles additionally coalesced which resulted in irregularly shaped extended 2D islands covering 2/3 of the oxide support (Fig. 3.2(c)). The fraction of 2 ML high particles was found to increase with increasing Pt coverage, but still 1 ML high particles were the dominating species. 2-dimensional structure of the particles (1 & 2 ML high) even at relatively high coverage indicated strong adhesion energy between Pt and Fe<sub>3</sub>O<sub>4</sub>(111). For the coverage of 2 ML, which was the highest coverage studied, the oxide surface was almost completely covered with 2 ML high particles ( $\sim 5$  Å in height) with some additional 3-dimensional (mainly 4 ML high) particles appearing (Fig. 3.2(d)). The insets in Figs. 3.2(a)-(d) show coverage dependent changes in particle height

---

distribution. It can be seen that the fraction of multilayer particles increases with increasing Pt coverage.

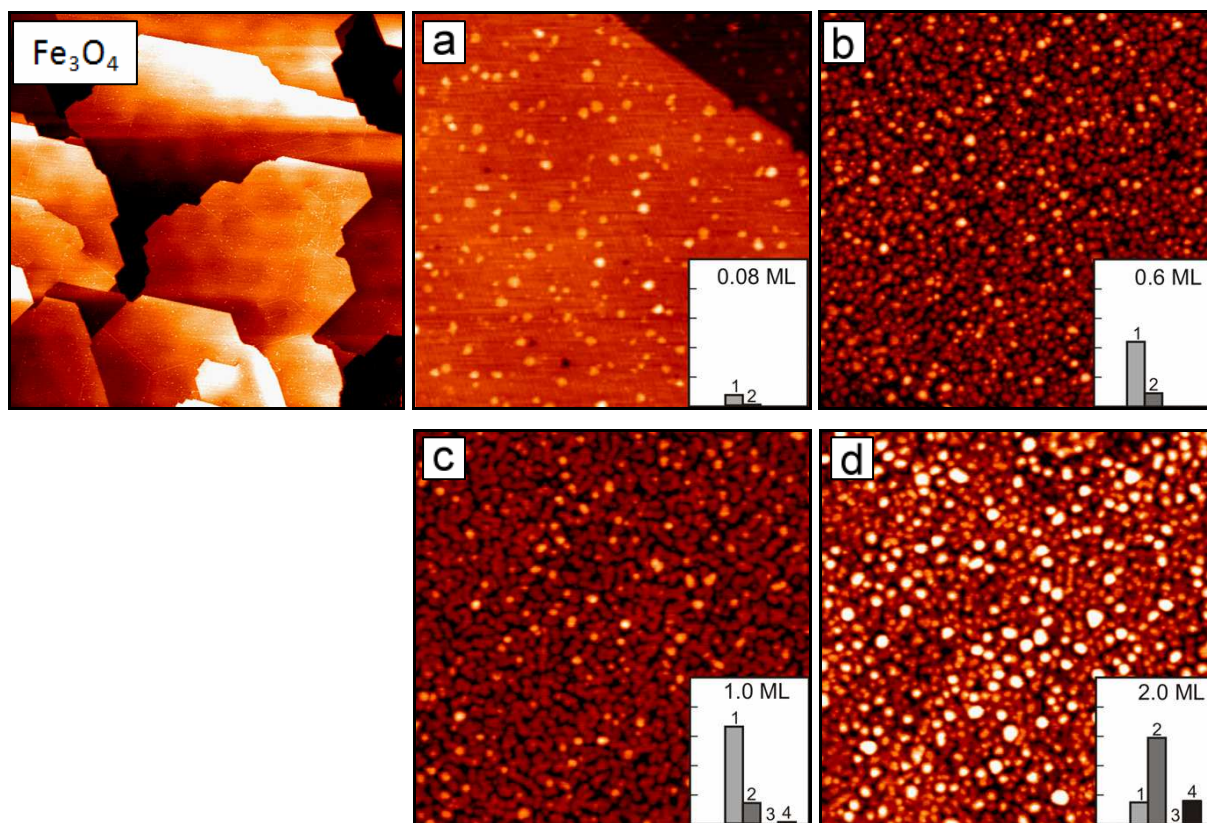


**Fig. 3.2** STM images of Pt / Fe<sub>3</sub>O<sub>4</sub>(111) at different coverages: 0.08 ML (a), 0.6 ML (b), 1.0 ML (c) and 2.0 ML (d); insets show coverage dependent changes in particle height distribution; STM image of Fe<sub>3</sub>O<sub>4</sub>(111) film as prepared is shown for comparison (STM: 500 x 500 nm<sup>2</sup>, 1.4 V, 0.7 nA (Fe<sub>3</sub>O<sub>4</sub>); 100 x 100 nm<sup>2</sup>, 1.4 V, 0.7 nA (a); 100 x 100 nm<sup>2</sup>, 1.0 V, 1.0 nA (b); 100 x 100 nm<sup>2</sup>, 1.4 V, 0.7 nA (c) and 100 x 100 nm<sup>2</sup>, 1.0 V, 0.7 nA (d))

### 3.3.2 Thermal stability

2-dimensional growth of Pt on Fe<sub>3</sub>O<sub>4</sub>(111) indicated high adhesion energy between the metal and the support. However, due to the fact that the particles were deposited at T = ~100 K (and then heated to 300 K for STM studies) it was not clear if this kind of treatment resulted in equilibrium particles' size and shape. In order to investigate if the high adhesion energy really determines the formation of 1- and 2-monolayer high islands, the samples

were additionally annealed at 600 K for 1 min. STM images of the samples after annealing are presented in Figs. 3.3(a)-(d). Profile lines show selected particles' heights and Fig. 3.3(e) summarizes the particle height distribution for the annealed samples.

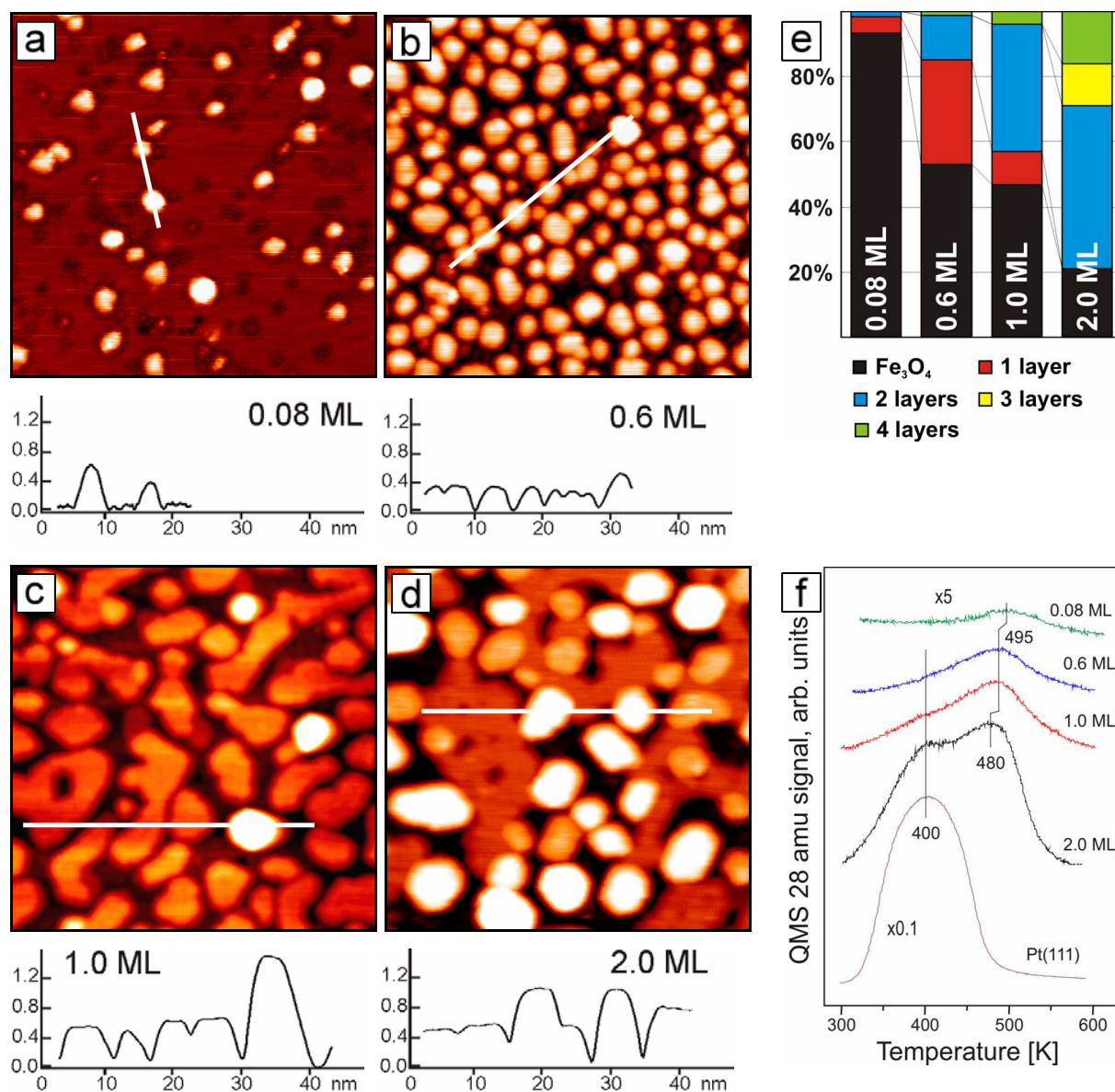


**Fig. 3.3** STM images of Pt / Fe<sub>3</sub>O<sub>4</sub>(111) at different coverages annealed at 600 K for 1 min: 0.08 ML (a), 0.6 ML (b), 1.0 ML (c) and 2.0 ML (d); profile lines show particles height; the diagram (e) shows coverage dependent changes in particle height distribution; corresponding CO TPD results compared with clean Pt(111) single crystal are shown in (f) (STM: 50 x 50 nm<sup>2</sup>, 1.0 V, 0.6 nA (a); 1.0 V, 1.0 nA (b); 1.4 V, 0.7 nA (c) and 1.4 V, 0.7 nA (d))

For the lowest studied coverage of 0.08 ML no significant changes in particles morphology were observed (Fig. 3.3(a)). At the 0.6 ML coverage the particles sintered which resulted in significant lateral size increase (by a factor of two on average) (Fig. 3.3(b)), but the particles' height remained 1 ML. For the coverage of 1 ML annealing resulted in a formation of 2 ML high Pt islands (Fig. 3.3(c)). The islands exhibited mainly irregular shapes, however, some preferential orientation of the edges could be seen. At the highest studied coverage of 2 ML 3-dimensional particles (up to 1 nm in height) were formed in addition to 2-dimensional islands (Fig. 3.3(d)). Based on the structural information provided by STM, namely the particles' height, width and the orientation of planes and edges, a modified Wulff construction could be applied to calculate the work of adhesion between Pt and Fe<sub>3</sub>O<sub>4</sub>(111) (for details please refer to Chapter 1.2). However, because of the irregular shape of the particles it was difficult to determine their exact width. Also, as we will show below, extended Pt islands transform into 3-dimensional particles upon annealing at 800 K which indicates that annealing at 600 K does not results in equilibrium particles' shape. Nevertheless, with some assumptions, Wulff construction can be used, even though the approximations result in some uncertainty. As mentioned above, upon annealing at 600 K larger, irregularly-shaped Pt islands are formed by coalescence of smaller, better-shaped ones. As an approximation, the structural parameters of the latter ones could be used for the analysis. According to the literature results, the crystallographic orientations of the top facets and edges of Pt particles on Fe<sub>3</sub>O<sub>4</sub>(111) are (111) and (111) / (100) respectively [87, 88]. Based on this, we assigned  $s_{100} / s_{111}$  as the ratio of the top facet side length, which is the parameter  $s$  in the formula (3) given in Chapter 1.2. The symmetry of the edge planes of Pt particles annealed at 600 K is quite complicate, however, for the small height / width ratios the work of adhesion value is rather insensitive to the variations in  $s$ . Using these assumptions, we calculated the approximate values of work of adhesion. In addition, we calculated the work of adhesion for Pd particles on Fe<sub>3</sub>O<sub>4</sub>(111) (based on the results published in [89-92]), in order to compare it with  $W_{adh}$  values obtained for Pt / Fe<sub>3</sub>O<sub>4</sub>(111). The  $\gamma$  values for Pt(111) and Pd(111) used in our calculations were taken from DFT results [94]. For the Pt particles formed at 1 ML coverage after annealing at 600 K for 1 min, the calculated work of adhesion was  $W_{adh} = 4.0 \pm 0.5 \text{ J/m}^2$ . For the 3D particles formed at 2 ML coverage after annealing the  $W_{adh} = 3.8 \pm 0.1 \text{ J/m}^2$ . For comparison, the calculated work of

---

adhesion for Pd / Fe<sub>3</sub>O<sub>4</sub>(111) annealed at 600 K was found to be  $W_{adh} = 3.15 \pm 0.1 \text{ J/m}^2$ , which is much lower than for Pt. On Fe<sub>3</sub>O<sub>4</sub>(111) Pd forms only well-faceted 3D particles and Pt, which has a higher surface energy than Pd, could be expected to form even more ball-like particles. We believe it is the high adhesion energy between Pt and Fe<sub>3</sub>O<sub>4</sub>(111) which determines the formation of 2-dimensional islands in case of Pt instead of 3-dimensional particles observed for Pd (even at higher coverage).

In order to get a deeper insight into the detailed structure of Pt particles on Fe<sub>3</sub>O<sub>4</sub>(111), CO TPD studies were performed. We looked at CO desorption states between 300 and 600 K. To avoid changes in particles morphology (such as the effects of sintering which could take place during TPD experiments while heating to 600 K) the samples were pre-annealed at 600 K for 1 min. Also, in that way any CO molecules that could potentially adsorb from the background pressure of residual gases during Pt deposition were desorbed. After annealing the particles exhibited atomically flat top facets (Figs. 3.3(a)-(d)), which are believed to be (111) based on the literature results [87, 88]. Using CO TPD we addressed the structure of these facets and their crystallographic orientation. Additional blank experiment was made on Pt(111) single crystal using the same experimental setup. The experiment revealed a broad CO desorption state centered ~400 K which we attributed to CO desorbing from Pt(111) terraces (Fig. 3.3(f)), based on published results [95-98]. Publications also pointed out a desorption signal ~480 K assigned to CO desorption from low-coordinated Pt sites such as the step edges, kinks etc. Another blank experiment was made on pristine Fe<sub>3</sub>O<sub>4</sub>(111) film (not shown). The results revealed that at 300 K CO does not adsorb on Fe<sub>3</sub>O<sub>4</sub>(111) which is also in agreement with the literature results which mention only desorption states below RT (so called “ $\alpha$ ”, “ $\beta$ ” and “ $\gamma$ ” peaks positioned at 110, 180 and 230 K, respectively) [89, 99]. In the light of the blank experiments, two CO desorption peaks were expected from Pt / Fe<sub>3</sub>O<sub>4</sub>(111) system in the temperature range between 300 and 600 K: ~400 K, corresponding to CO desorption from Pt(111) facets and ~480 K corresponding to desorption from low-coordinated Pt sites. For the Pt coverages of 0.08 ML, 0.6 ML and 1 ML a CO desorption peak with a maximum at ~495 K and a shoulder at ~400 K was observed (Fig. 3.3(f)). For the 2 ML Pt coverage the peak ~495 K shifted down to ~480 K and the signal ~400 K increased. The positions of these peaks fitted the blank experiments and the literature values quite well. Next, we compared the CO desorption spectrums with the

---

corresponding morphologies (Figs. 3.3(a)-(d)). For the sub-monolayer Pt coverages, where only very small 2D particles were observed, the high temperature peak was found to scale with increasing platinum coverage. This could have been expected due to increasing number of low coordinated sites and rather negligible area of (111) planes. For the 1 ML coverage, where extended 2-monolayer-high islands of Pt were covering the major fraction of the surface, domination of the CO desorption from the (111) facets of Pt rather than from low coordinated sites was expected. Surprisingly, the recorded CO TPD spectrum exhibited mainly the high temperature peak and almost no desorption  $\sim 400$  K. We calculated the CO uptake per Pt surface area from the results obtained for Pt particles and Pt(111) single crystal using the areas under the curves. The CO adsorption capacity of Pt particles turned out to be proportionally  $\sim 10$  times lower than that of single crystal. The value was even lower when we have considered only the areas under the peaks centered at  $\sim 400$  K after spectral deconvolution. Interestingly, for the 2 ML Pt coverage the desorption  $\sim 400$  K was more adequate to the corresponding Pt surface area. The main difference in morphology between the 1 ML and 2 ML coverages was the presence of 3D particles that formed at 2 ML coverage after annealing at 600 K. It could be concluded that CO adsorption capability of the top facets of 2-dimensional (1 and 2 ML high) Pt particles grown on Fe<sub>3</sub>O<sub>4</sub>(111) was different than that of Pt(111) single crystal terraces and top facets of 3-dimensional (3 ML and higher) Pt particles. In order to check if Pt particles exhibit additional desorption features below 300 K we adsorbed CO at  $\sim 100$  K on similarly prepared samples and performed TPD from 100 to 600 K (not shown). Only the well-established in the literature peaks characteristic for CO desorption from pristine Fe<sub>3</sub>O<sub>4</sub>(111) were observed at the temperatures below the room temperature. Desorption signals from Pt particles in that temperature range, if any, were either lost in Fe<sub>3</sub>O<sub>4</sub>(111) signal or there were no additional features. The 300-600 K part of the spectrum reproduced the above mentioned relation between the Pt coverage / morphology and the CO uptake. Low CO adsorption capability of 2-dimensional Pt particles could origin from different effects:

- (i) Pt alloys with the substrate oxide
- (ii) Pt particles are encapsulated by iron oxide

- (iii) monolayer and bilayer Pt islands adopt to the structure of the supporting oxide

To exclude scenarios (i) and (ii) additional experiment was performed where Pt was deposited at ~100 K onto freshly prepared Fe<sub>3</sub>O<sub>4</sub>(111) film, exposed to CO and flashed to 600 K in front of the QMS. The important difference as compared to previous experiments was that the particles were not pre-annealed at 600 K prior to CO exposure. At 100 K alloy formation or encapsulation are rather improbable. The CO desorption signal was found to be very similar to that from the samples pre-annealed at 600 K (not shown). Considering the same Pt surface area, the calculated amount of CO molecules desorbing from the sample turned out to be ~30 % higher than for the pre-annealed system, however, this difference could be roughly explained by morphological changes which occur during heating from 100 K to 600 K. Scenario (iii) seemed to be the most probable. CO adsorption on metals follows the Blyholder model (for details please refer to Chapter 1.3). If the high adhesion energy between platinum and iron oxide would force the expansion of Pt lattice constant from 2.77 Å to 2.97 Å, a value which is the nearest neighbour distance in oxygen sublattices in Fe<sub>3</sub>O<sub>4</sub>(111), the expansion would reduce the Pt → CO π\* back-donation and therefore significantly weaken the Pt–CO bond. Unfortunately, the expansion could not be proven by STM because it was not possible to image the atomic structure of Pt particles using our experimental setup. However, the LEED pattern did not exhibit any additional features next to Fe<sub>3</sub>O<sub>4</sub>(111) spots, as could be expected for the sample covered in ~50 % by extended islands of crystalline Pt with different lattice constant than the oxide underneath. This further supported the hypothesis that the structure of Pt particles adopted to the structure of the substrate oxide. Theoretical studies would be necessary to fully validate this scenario.

We also examined the thermal stability of Pt deposits at high temperatures. 2.6 monolayers of Pt were deposited at RT onto freshly prepared Fe<sub>3</sub>O<sub>4</sub>(111) film. The sample was first flashed to 600 K, then annealed at 600 K for 5 min and finally annealed at 850 K for 1 min. STM and CO TPD were performed after each thermal treatment. The results, including particle height distribution diagram, are summarized in Figs. 3.4(a)-(e). Heating to 600 K resulted in a transformation of small particles into extended 2-dimensional islands and additional 3-dimensional particles, as expected for the Pt coverage > 2 ML. Longer annealing

---



at this temperature led to decrease in CO adsorption capabilities (Fig. 3.4(f)) which could be explained by morphological changes, namely the reduction of Pt surface area due to sintering effects. After annealing at 850 K for 1 min higher and better shaped particles were formed, with sharp edges running along the crystallographic directions of the substrate oxide. A significant fraction of the oxide support became uncovered so that the atomic structure between the particles could be resolved in STM (see Figs. 3.5(a)-(c)). The orientations of particles' edges further confirmed good epitaxial relationship between Pt(111) and Fe<sub>3</sub>O<sub>4</sub>(111). Heating at 850 K resulted in a dramatic drop of CO uptake (Fig. 3.4(f)) which could not be explained by thermal induced changes in particles size and shape (Fig. 3.4(d)).

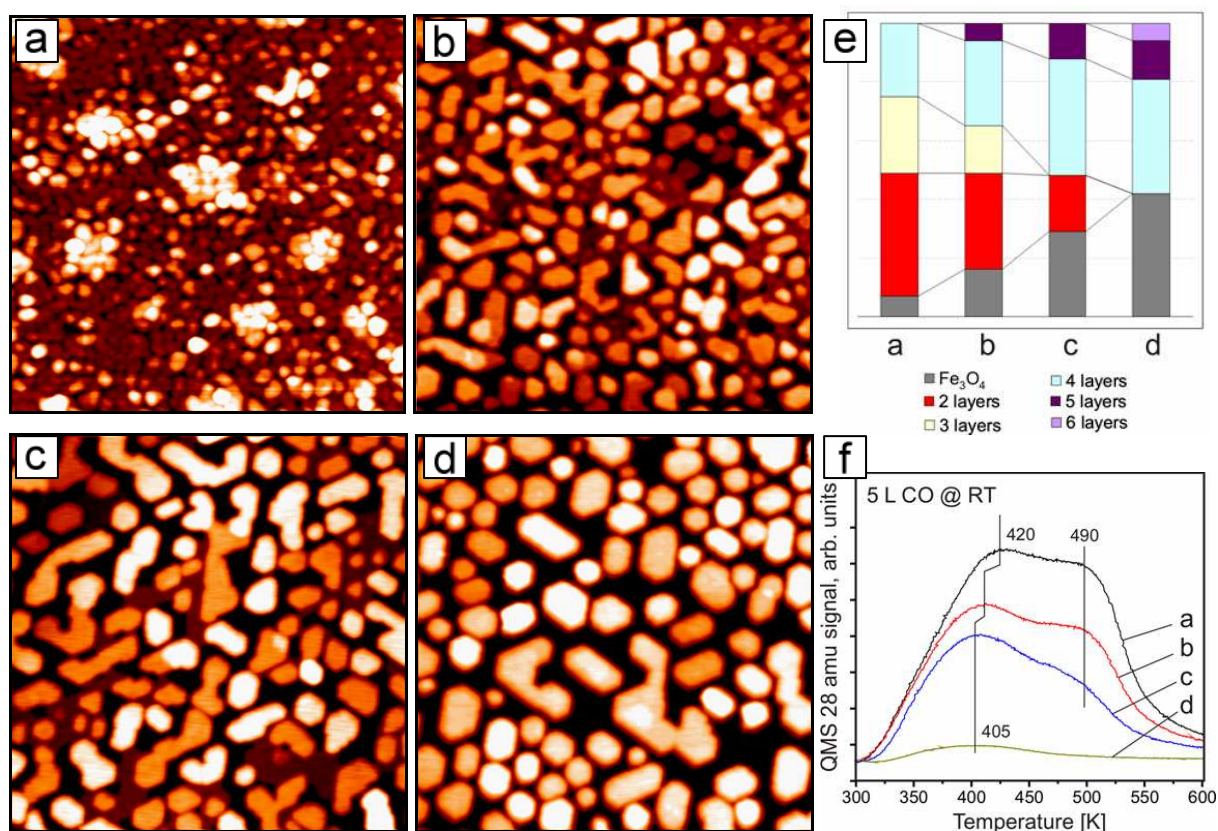


**Fig. 3.4** STM images of 2.6 ML Pt / Fe<sub>3</sub>O<sub>4</sub>(111): as deposited (a), flashed to 600 K (b), annealed at 600 K for 5 min (c) and annealed at 850 K for 1 min (d); the diagram (e) shows coverage dependent changes in particle height distribution; corresponding CO TPD results are shown in (f)

(STM: 100 x 100 nm<sup>2</sup>, 1.4 V, 0.7 nA (a-d))

An interesting observation was made on the basis of STM results: after annealing from 600 to 850 K the calculated total particle volume increased by ~20 % while previously it remained relatively constant when the sample was annealed from 100 to 600 K. Strongly decreased chemisorption is a typical manifestation of the Strong Metal-Support Interaction (SMSI), an effect often observed for noble metal particles supported on reducible oxides upon reducing treatment such as high temperature annealing in UHV (for details please refer to Chapter 1.2). The SMSI is typically associated with a decoration of the metal by a reduced form of the supporting oxide (so called “encapsulation”). It became clear that either the substrate material was somehow incorporated into the Pt particles or the particles were covered by the atoms of the support. The final prove for particles encapsulation came from more detailed STM studies. It was observed that the top facets of the largest Pt particles exhibit a superstructure with ~25 Å periodicity (Figs. 3.5(a)-(c); presented images were obtained for 1.8 ML Pt / Fe<sub>3</sub>O<sub>4</sub>(111) sample exposed to ~540 L of O<sub>2</sub> at 500 K and ~230 L of H<sub>2</sub> at the same temperature prior to flashing to 850 K in UHV (experiment described below), however, the observed encapsulating layer was identical). This periodicity is very similar to the long-range periodicity of the Moiré pattern observed on monolayer FeO(111) films grown on Pt(111) (for details please refer to Chapter 1.4). We were also able to get atomic resolution STM images exhibiting ~3 Å periodicity (Figs. 3.5(d)-(e); obtained for 2.6 ML Pt / Fe<sub>3</sub>O<sub>4</sub>(111) sample annealed at 850 K for 5 min). The results gave direct evidence that the Pt particles were encapsulated by iron oxide and the encapsulating layer is FeO(111) in nature. Due to the fact that the size of the Moiré unit cell is comparable to the size of the largest particles’ top facets, it was easier to observe the superstructure there. However, smaller Pt particles also exhibited wave-like modulation with similar periodicity which suggested that they were also encapsulated by some form of iron oxide. It also has to be mentioned that rarely, on top of some large Pt particles, different atomic structures were observed (not shown). These structures had a periodicity of ~6 Å, more similar to the periodicity observed on Fe<sub>3</sub>O<sub>4</sub>(111). In addition, they also exhibited the Moiré-like modulation amplitude. However, it was not clear if this was an iron oxide indeed or some kind of 2x2 surface reconstruction (O<sub>2</sub>? [44, 100, 101], low temperature FeO? [102, 103]). Nevertheless, these were the minor species observed.

---

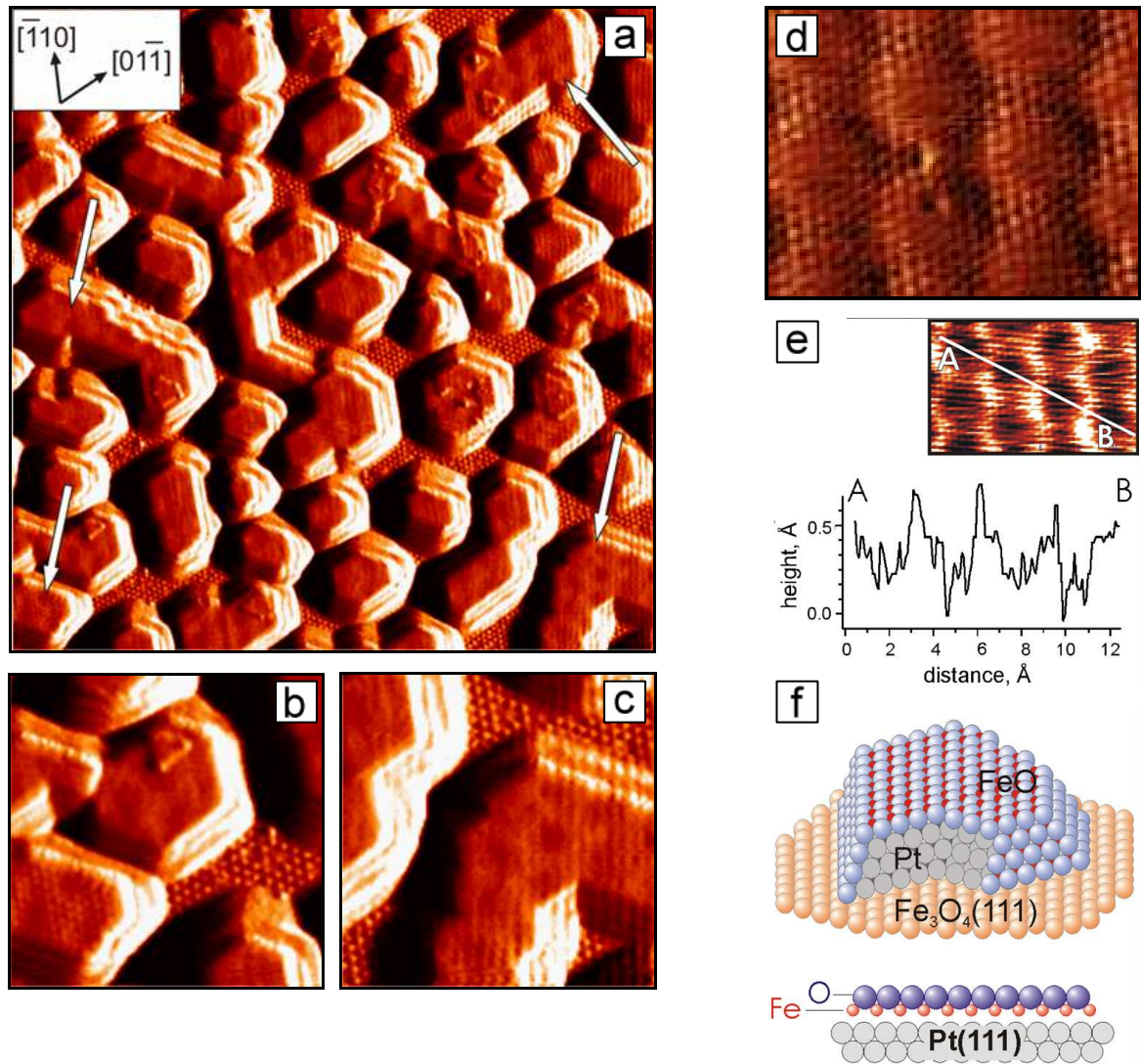


**Fig. 3.5** STM images of encapsulated Pt nanoparticles: Moiré pattern visible on the top facets (a-c); atomic resolution image showing structure with  $\sim 3$  Å periodicity (d); profile line showing the Moiré corrugation amplitude (e); schematic drawing of a Pt particle encapsulated by FeO(111) (f) (STM:  $80 \times 80$  nm<sup>2</sup>, 0.5 V, 0.6 nA (a);  $20 \times 20$  nm<sup>2</sup>, 0.5 V, 0.6 nA (b, c) and 0.5 V, 0.7 nA (d, e))

A question arose: why the particles were encapsulated by FeO(111) and not by the substrate Fe<sub>3</sub>O<sub>4</sub>(111)? It is known that iron oxides grow on Pt via Stransky-Krastanov mode [10, 104]. FeO(111) can be grown up to a total coverage of  $\sim 2.5$  ML by oxidation of iron in  $1 \times 10^{-6}$  mbar O<sub>2</sub> at 870 K. If the oxidation is performed at 1000 K, only a single FeO(111) layer is formed with Fe<sub>3</sub>O<sub>4</sub>(111) islands nucleating on top of it and coalescing with increasing coverage. This suggest that at low iron coverage the growth of FeO wetting layer is

thermodynamically more favorable than the growth of Fe<sub>3</sub>O<sub>4</sub>. If the iron migration from the oxide support to the Pt particles would be possible then an FeO layer would be formed in first place. It is important to mention that the decrease of CO uptake was also observed on the low-coordinated sites of Pt particles. As judged by the crystallographic orientations of the particles edges, the side facets exhibited (100) and (111) planes. From the literature it is known that FeO(111) monolayer films can be also grown on Pt(100) single crystal surfaces [105]. All this led us to the conclusion that the top, as well as the side facets, were encapsulated by FeO(111) so that the oxide was completely covering the Pt particles (Fig. 3.5(f)).

We also tried to determine the details on how the encapsulation proceeds. Fig. 3.6 presents CO TPD results obtained for 1.8 ML Pt / Fe<sub>3</sub>O<sub>4</sub>(111) sample after stepwise heating to 600, 700 and 800 K.

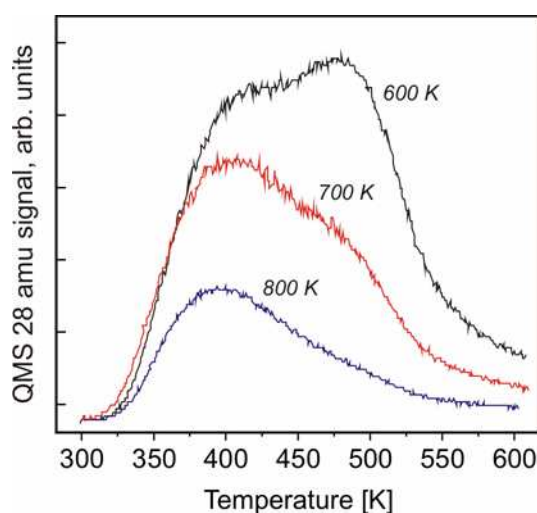


**Fig. 3.6** CO TPD results for 1.8 ML Pt / Fe<sub>3</sub>O<sub>4</sub>(111) after stepwise heating to 600, 700 and 800 K

A systematic drop in the CO uptake was observed after heating to 700 and 800 K. STM revealed that upon heating the particles sintered forming larger complexes (similarly as for the sample presented in Fig. 3.4). Most of the new-formed particles were  $0.9 \pm 0.1$  nm in height which corresponded to  $\sim 4$  atomic layers of Pt(111). As calculated on the basis of STM results, the fraction of uncovered oxide support increased from  $\sim 20$  to  $\sim 50$  % on average and the Pt surface area decreased by  $\sim 30$  % while CO TPD revealed that the CO uptake decreased

by ~70 %. Of course, this is only true if we consider that the CO uptake is proportional to the Pt surface area and is not much affected by precise particles morphology (at least for the particles which are > 5 nm in diameter). It was observed that the high temperature CO desorption peak, which is attributed to low-coordinated Pt sites, attenuated first (as clearly seen in Fig. 3.5 for heating from 600 to 700 K). All this suggested that the encapsulation proceeds gradually and most likely begins at the particles edges. More compelling evidence to this conclusion came from low temperature (LT) CO TPD experiments performed for different Pt coverages (Fig. 3.7). Prior to CO exposure Pt particles were pre-annealed at 600 K.

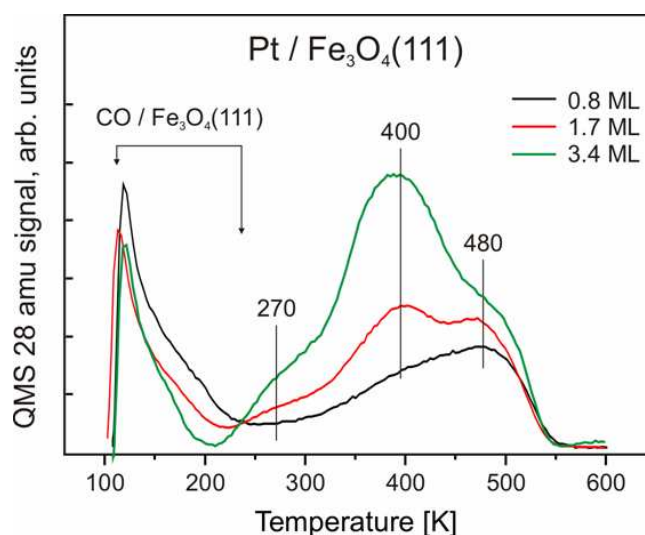


**Fig. 3.7** LT CO TPD results for Pt / Fe<sub>3</sub>O<sub>4</sub>(111) as a function of Pt coverage: 0.8, 1.7 and 3.4 ML (provided by Yingna Sun, PhD thesis, FU Berlin (2010))

The signals between 110 and 230 K were assigned to CO desorption from the substrate Fe<sub>3</sub>O<sub>4</sub>(111) film [89, 99], while the signals centered around 400 and 480 K were attributed to CO desorption from (111) facets and low-coordinated sites of Pt, respectively [95-98]. A new desorption state ~270 K was observed and tentatively assigned to CO desorption from Pt particles as the signal scaled with increasing Pt coverage. To explain the nature of this peak an experiment was made where Pt(111) single crystal surface was sputtered with 1 keV Ar<sup>+</sup> ions at RT and annealed at 600 K for 5 min. In that way a rough surface consisting of nanometer-sized Pt(111) terraces and large fraction of low coordinated sites was obtained

as judged by STM (Fig. 3.8(a)). CO TPD revealed two desorption states from this surface:  $\sim 400$  K attributed to Pt(111) terraces and  $\sim 510$  K attributed to low-coordinated sites. Next, 0.1 ML Fe was deposited at RT onto the Pt(111) surface and the sample was annealed at 600 K for 5 min. CO TPD results have shown that the intensity of the  $\sim 510$  K peak decreased upon Fe deposition by a factor of two, while the CO capacity of Pt terraces remained unchanged (Fig. 3.8(b)). In addition, a new desorption state appeared below 300 K, very similar to the  $\sim 270$  K peak observed on Pt / Fe<sub>3</sub>O<sub>4</sub>(111).

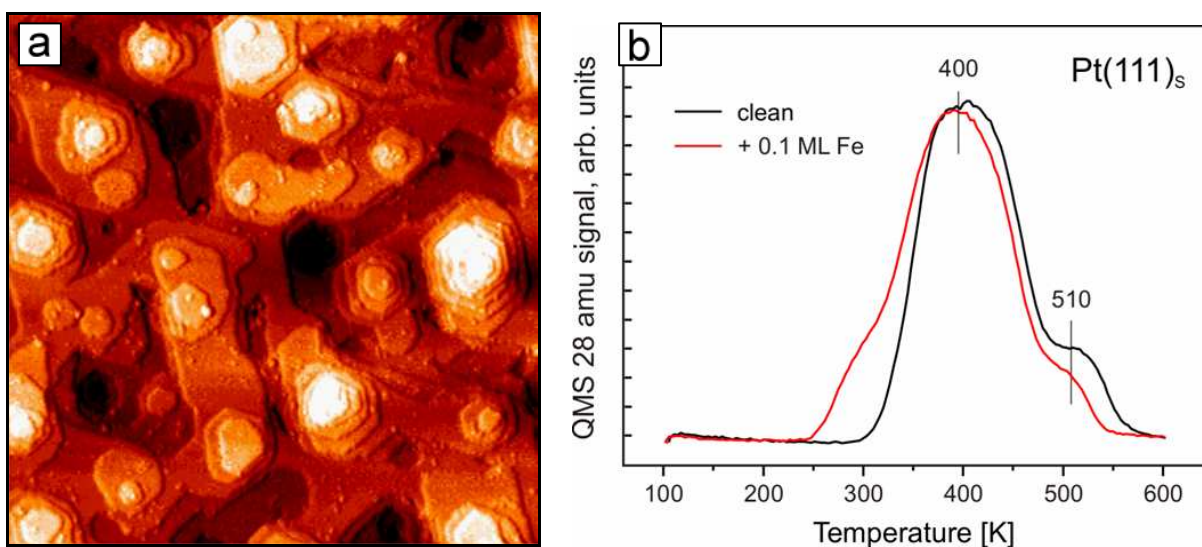


**Fig. 3.8** STM image of Pt(111) single crystal sputtered with 1 keV Ar<sup>+</sup> ions at 300 K and annealed at 600 K for 5 min (a); corresponding CO TPD spectra (black line) compared with the spectra obtained for the sample after 0.1 ML Fe deposition (red line) (b) (STM: 100 x 100 nm<sup>2</sup>, 0.7 V, 0.4 nA) (TPD provided by Yingna Sun, PhD thesis, FU Berlin (2010))

The decrease of the high temperature signal could be explained by decoration of the step edges by Fe and partial intermixing / alloying upon annealing. It was reported in the literature that the CO bond strength on Pt-Fe surfaces is weaker than on clean Pt [106]. It has to be kept in mind that Pt undergoes the SMSI effect on Fe<sub>3</sub>O<sub>4</sub>(111) which could result, in its initial stage at 600 K, in iron and / or oxygen migration onto Pt particles. Since the affinity of Pt to oxygen is lower than for iron, the metal migration is more probable than the O spillover. We believe that iron migration to low coordinated sites of Pt particles is the initial stage of encapsulation. Therefore, the presence of the peak  $\sim 270$  K could be explained

in the light of Fe migration onto Pt particles and partial intermixing upon annealing. We also observed carbon deposition on Pt upon CO treatment at 500 K (not shown; for details please refer to [82]). CO dissociation on low coordinated Pt sites could be another reason for the weakening of CO bonding strength to the particles' top facets.

It was also interesting to check if oxidation at much lower temperature will also lead to encapsulation. For that reason a freshly prepared 1.8 ML Pt / Fe<sub>3</sub>O<sub>4</sub>(111) sample pre-heated to 600 K was exposed to  $1 \times 10^{-6}$  mbar O<sub>2</sub> at 500 K for the time corresponding to the exposure of  $\sim 540$  L. Subsequent exposure to  $1 \times 10^{-6}$  mbar H<sub>2</sub> @ 500 K for the time corresponding to  $\sim 230$  L was performed in order to remove the oxygen (if any) from the Pt surface. Such a low temperature oxidation / reduction treatment resulted in a population of Pt particles which were 3 and 4 ML in height as judged by STM (not shown). As calculated, upon the treatment the fraction of uncovered oxide support increased from  $\sim 20$  to  $\sim 30$  % on average and the Pt surface area decreased by  $\sim 25$  %. CO TPD revealed that the CO adsorption capabilities of the system decreased by  $\sim 75$  % (Fig. 3.9).

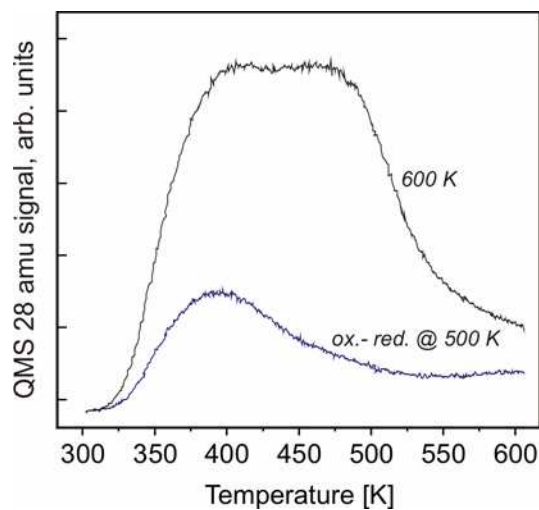


**Fig. 3.9** CO TPD results for 1.8 ML Pt / Fe<sub>3</sub>O<sub>4</sub>(111) flashed to 600 K (black line) and after additional oxidation-reduction treatment (blue line)

The effect was found to be similar to annealing at 850 K in UHV, however, it was not accompanied by as significant morphological changes. Interestingly, additional annealing at 850 K resulted in a formation of well-shaped, extended Pt particles, similar to the samples

which were not treated with O<sub>2</sub> and H<sub>2</sub> (not shown). When the oxidation / reduction procedure was applied to the samples which were first annealed to high temperatures, the treatment did not affect the particles' morphology and CO adsorption capabilities at all.

Interestingly, as judged from CO TPD results, there were some Pt sites which did not undergo the encapsulation, no matter if the encapsulation was induced by high temperature annealing in UHV or oxidation / reduction treatment (Figs. 3.6 and 3.9). In addition, the surface area of these sites was approximately the same in both cases. This phenomenon needs further investigation because it could be potentially useful in selective blocking of the reaction sites which are active in the absence of encapsulation (such as the top facets or edges of the particles), thus increasing the catalytic selectivity.

The theoretical explanation for the encapsulation of Pt particles on Fe<sub>3</sub>O<sub>4</sub>(111) could come again from surface energies and work of adhesion calculated on the basis of Wulff construction. As mentioned, the calculated work of adhesion for Pt particles annealed at 600 K was  $W_{adh} = 3.8 \pm 0.1 \text{ J/m}^2$ . For the particles annealed at 800 K the value increases to  $4.15 \pm 0.1 \text{ J/m}^2$ . Of course, this very high value would be valid for the particles which are not covered with iron oxide. The role of the encapsulating layer is to reduce the surface energy of the particle. In order to include the encapsulating oxide layer in the calculations,  $\gamma_{111}$  should be substituted with  $\gamma_{FeO/Pt(111)}$ . The  $\gamma_{FeO/Pt(111)}$  value is unknown, however, it is for sure smaller than  $\gamma_{111}$ . Therefore the value  $4.15 \text{ J/m}^2$  is the upper limit. For comparison, the calculated adhesion energy of Pd particles on Fe<sub>3</sub>O<sub>4</sub>(111) annealed at 600 K was  $3.15 \text{ J/m}^2$ . This value is much lower than for Pt on Fe<sub>3</sub>O<sub>4</sub>(111). That is probably why Pt undergoes the encapsulation while Pd does not. Another possible explanation would include electron transfer from the Fe<sub>3</sub>O<sub>4</sub>(111) film to the Pt particles (as generally proposed for SMSI in [17, 30]). The surface negative charges would favor the diffusion of Fe cations onto Pt particles, especially at high temperatures.



# Chapter 4

## Ultrathin FeO(111) films on Pt(111) in CO oxidation reaction

based on publications:

[107] Y.-N. Sun, Z.-H. Qin, M. Lewandowski, S. Kaya, S. Shaikhutdinov, and H.-J. Freund, *When an Encapsulating Oxide Layer Promotes Reaction on Noble Metals: Dewetting and in situ Formation of an "Inverted" FeO<sub>x</sub>/Pt Catalyst*, *Catalysis Letters* 126 (2008), p. 12631-12635.

[108] Y.-N. Sun, Z.-H. Qin, M. Lewandowski, E. Carrasco, M. Sterrer, S. Shaikhutdinov, and H.-J. Freund, *Monolayer Iron Oxide Film on Platinum Promotes Low Temperature CO Oxidation*, *Journal of Catalysis* 266 (2009), p. 359-368.

[109] Y.-N. Sun, L. Giordano, J. Goniakowski, M. Lewandowski, Z.-H. Qin, C. Noguera, S. Shaikhutdinov, G. Pacchioni, and H.-J. Freund, *The Interplay between Structure and CO Oxidation Catalysis on Metal-Supported Ultrathin Oxide Films*, *Angewandte Chemie* 122 (2010), p. 4520-4523 & *Angewandte Chemie International Edition* 49 (2010), p. 4418-4421.

[110] L. Giordano, M. Lewandowski, I. M. N. Groot, Y.-N. Sun, J. Goniakowski, C. Noguera, S. Shaikhutdinov, G. Pacchioni, and H.-J. Freund, *Oxygen-induced Transformations of a FeO(111) Film on Pt(111): A Combined DFT and STM Study*, *The Journal of Physical Chemistry C* 114 (2010), p. 21504-21509.

[111] M. Lewandowski, Y.-N. Sun, Z.-H. Qin, S. Shaikhutdinov, and H.-J. Freund, *Promotional effect of metal encapsulation on reactivity of iron oxide supported Pt catalysts*, *Applied Catalysis A: General* 391 (2011), p. 407-410.

[112] Y. Lei, M. Lewandowski, Y.-N. Sun, Y. Fujimori, Y. Martynova, I. M. N. Groot, R. Meyer, L. Giordano, G. Pacchioni, J. Goniakowski, C. Noguera, S. Shaikhutdinov, and H.-J. Freund, *CO + NO vs CO + O<sub>2</sub> reaction on monolayer FeO(111) films on Pt(111)*, *ChemCatChem* 3 (2011), p. 671-674.

[113] M. Lewandowski, I. M. N. Groot, S. Shaikhutdinov, and H.-J. Freund, *Scanning tunneling microscopy evidence for the Mars-van Krevelen type mechanism of low temperature CO oxidation on an FeO(111) film on Pt(111)*, *Catalysis Today* (2011), accepted.

### 4.1 Introduction

FeO(111) films grown on Pt(111) consist of 1 ML of iron and 1 ML of oxygen and are only few Å thick [10]. Such ultrathin films grown on metal single crystals can act as suitable supports to model dispersed metal catalysts [83, 114]. However, these films often exhibit

different properties than their bulk counterparts. The atomic structure of the interface between the oxide and the metal substrate (the nature of chemical bonds, low coordination of atoms, polarity effects and, in case of some transition metal oxides, the possibility of having cations in different oxidation states) can influence the chemical and physical properties of the oxide film [115, 116]. In addition, for the films which are few Å in thickness the supporting metal may, in favorable cases, determine the properties of adsorbates and deposits which are present on the surface [83, 117-123]. This is due to charge transfer effects which may occur at the interface: from the metallic substrate through the ultrathin oxide layer to the adsorbed molecules or deposited metal atoms / clusters, which would remain neutral on thicker films. Electron tunneling through the oxide layer is determined by the work function of the metal support and the electron affinity of the adsorbate / deposit. Depending on the nature of the oxide layer the work function of the metal substrate can increase or decrease [124]. By choosing the proper materials it is also possible to tune the direction of electron flow. All these effects made ultrathin oxide films attractive for application in electronic and magnetic devices. In the middle of XXth century a concept of the so called “electronic theory of catalysis” was introduced [125]. The main interest was to investigate the relation between the thickness of ultrathin semiconductor films grown on metal single crystals and the catalytic reactivity / selectivity of these films. A citation: “The semiconductor film arises as a result of oxidation of a metal, and its thickness can often be controlled to some extent ... By varying the thickness ... it is possible to control the adsorption capacity, the catalytic activity, and the selectivity ... It would be interesting to study the adsorption and catalytic properties of a semiconducting film on a metal, and their changes, during growth of the film.” [125]. At that time the experimental tools were not available to study this issue in detail. These ideas faded away and were forgotten for the next decades. Nowadays, more and more often the catalytic activity / selectivity of ultrathin oxide film-based systems is being discussed in the light of charge transfer effects [121, 123]. Modern experimental tools and computational methods give possibility to study the structure of catalytic material on the atomic level, before, after and even during the reaction, and determine the role of charge transfer effects in the reaction.

The CO oxidation reaction on Pt(111) proceeds via Langmuir-Hinshelwood mechanism (for details please refer to Chapter 1.3). It was shown that the reaction rate

---

strongly depends on the CO:O<sub>2</sub> partial pressures [41-44]. It is generally accepted that the CO<sub>2</sub> yield is much higher in O-rich conditions (CO:O<sub>2</sub> < 0.2) than in O-lean. In the first case the metal surface is covered with oxygen which does not affect the adsorption of CO and in the second case the adsorbed CO suppresses the dissociation of O<sub>2</sub> due to site blocking [44]. In this chapter we present the results of our studies on the reactivity of ultrathin FeO(111) films on Pt(111) in low temperature CO oxidation reaction in the mbar pressure range. The chapter summarizes the results published in the PhD thesis of Yingna Sun (Freie Universität Berlin, 2010), which are here supported by additional STM images and theoretical DFT calculations (DFT provided by Livia Giordano, Jacek Goniakowski and Gianfranco Pacchioni).

## 4.2 Samples preparation

Pt(111) single crystal was cleaned and ultrathin FeO(111) films were prepared as described in Chapter 3.2. CO TPD was performed in order to check if the oxide layer is closed (at RT at pressures up to 10<sup>-3</sup> mbar CO does not adsorb on the surface of FeO(111), only on Pt sites if any exposed).

For reactivity experiments the samples were transported to the high pressure cell. The samples were exposed to millibar pressures of gases (O<sub>2</sub>, CO, NO, He) in different proportions and at different temperatures, as described in the experimental section (Chapter 4.3). No pumping was provided to the HP cell during reactivity experiments. After the reaction time the samples were first cooled down to T < 400 K and secondarily the high pressure cell was pumped to 1 x 10<sup>-6</sup> mbar. The samples were then transported to the main chamber and characterized ex-situ using LEED, AES and STM.

Fe<sub>3</sub>O<sub>4</sub>(111) films were prepared according to the preparation procedure described in Chapter 3.2. Pt was deposited at RT and annealed in UHV at 850 K for 5 min in order to form extended 3-dimensional particles encapsulated by FeO overlayer. The particles' encapsulation was confirmed by STM.

## 4.3 Results & Discussion

### 4.3.1 FeO(111) / Pt(111) vs. Pt(111)

We studied the CO oxidation reaction on FeO(111) films grown on Pt(111) single crystal and compared the results with clean Pt(111). At pressures up to  $10^{-3}$  mbar FeO(111) is known to be essentially inert towards O<sub>2</sub> and CO even at elevated temperatures such as 450 K. Surprisingly, we found that in the millibar pressure range the oxide film exhibits very high CO<sub>2</sub> production rate, much higher than Pt(111) single crystal under the same reaction conditions. Fig. 4.1 presents a comparison between the CO<sub>2</sub> production on FeO(111) / Pt(111) and Pt(111) single crystal in 40 mbar CO + 20 mbar O<sub>2</sub> reaction at 450 K, a temperature much lower than typically used for Pt catalyst. Time zero corresponds to the start of heating of the catalyst to the reaction temperature (heating rate during GC experiments: 1 K/s).

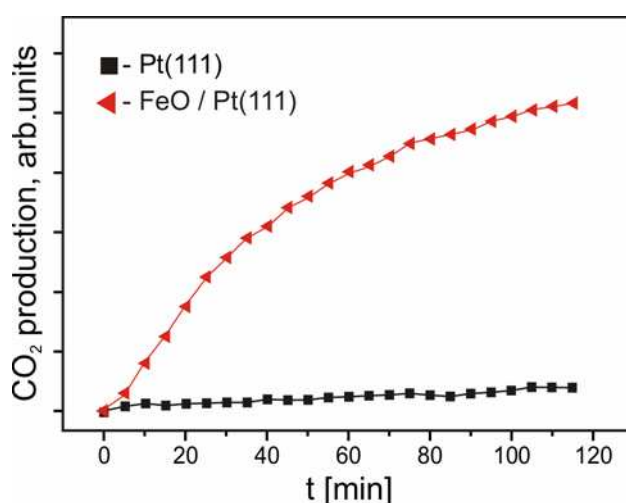


**Fig. 4.1** Kinetics of CO<sub>2</sub> production in CO oxidation reaction on FeO(111) / Pt(111) compared with Pt(111) single crystal: 40 mbar CO + 20 mbar O<sub>2</sub> at 450 K (GC results provided by Yingna Sun, PhD thesis, FU Berlin (2010))

In order to explain the greatly enhanced reactivity of ultrathin FeO(111) films, we performed systematic studies using different CO:O<sub>2</sub> ratios and different temperatures. To

determine the best CO:O<sub>2</sub> ratio we performed the reaction using pressure ratios ranging from 1:5 to 5:1, covering both the O-rich (CO:O<sub>2</sub> < 1) and the O-lean (or CO-rich) (CO:O<sub>2</sub> > 1) regimes. In the first case the O<sub>2</sub> pressure was kept constant at 20 mbar and the CO pressure was varied, and in the second case the CO pressure was kept at 10 mbar and the O<sub>2</sub> pressure was varied. The gas mixtures were always balanced with He to 1 bar. The results are presented in Fig. 4.2:

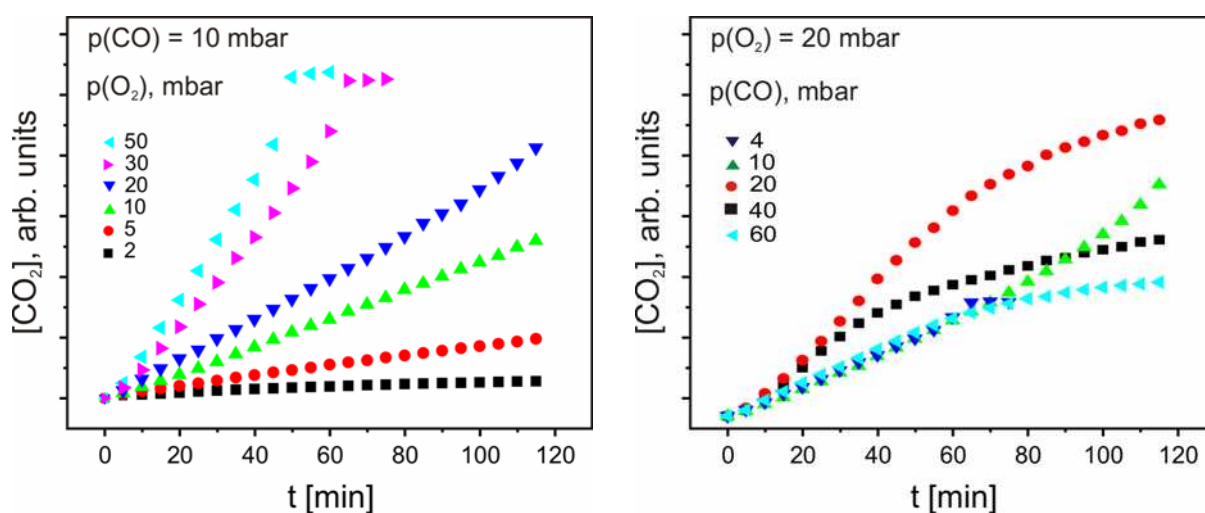


**Fig. 4.2** Kinetics of CO<sub>2</sub> production in CO oxidation reaction on FeO(111) / Pt(111) at 450 K for different CO and O<sub>2</sub> partial pressures  
(GC results provided by Yingna Sun, PhD thesis, FU Berlin (2010))

It was observed that in O-rich conditions the reaction rate is almost constant with time and increases when approaching 100% conversion, while in O-lean conditions the reaction slows down with time. Next, in order to determine the best total CO + O<sub>2</sub> pressure, experiments were performed where the CO:O<sub>2</sub> ratio was kept constant, but different total pressures were used (not shown). The results revealed that the reaction goes slower, if the partial pressures are reduced by an order of magnitude (for example 20 + 40 mbar compared with 2 + 4) (not shown). Nevertheless, in the whole pressure range studied, the FeO(111) films showed much higher activity in CO<sub>2</sub> production than Pt(111) single crystal.

We also tried to determine the best reaction temperature. For this we performed the 40 mbar CO + 20 mbar O<sub>2</sub> reaction at different temperatures between 400 and 450 K (Fig.

4.3). The maximum CO<sub>2</sub> production rate was observed for the reaction carried at 450 K, with a visible threshold at ~430 K.

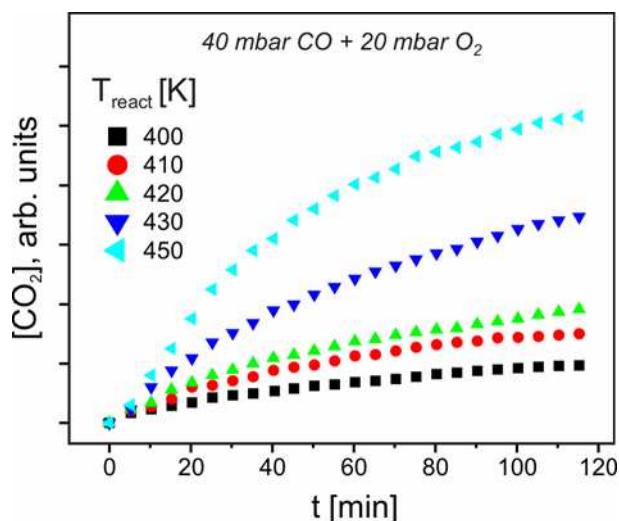


**Fig. 4.3** Kinetics of CO<sub>2</sub> production in CO oxidation reaction on FeO(111) / Pt(111) carried at different temperatures using 40 mbar CO + 20 mbar O<sub>2</sub>  
(GC results provided by Yingna Sun, PhD thesis, FU Berlin (2010))

It is important to mention that all the results did not seem to be affected by CO<sub>2</sub> accumulation in the reactor (pumping the reactor and refilling the gases did not have any impact on the reaction).

#### 4.3.2 O-lean conditions

We tried to explain why the reaction slows down with time in O-lean conditions. We performed LEED analysis of FeO(111) films after the reaction in O-lean conditions. As shown in Fig. 4.4 the characteristic satellite spots of FeO(111) were no longer visible and only Pt(111)-(1x1) spots with weaker Pt(111)-c(4x2)CO spots [98] could be seen. The results indicated that most probably a significant fraction of Pt(111) became exposed after the reaction.

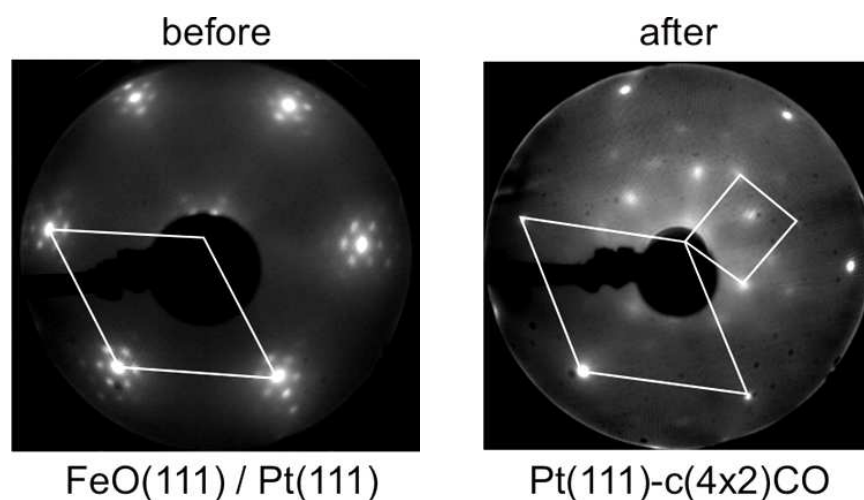


**Fig. 4.4** LEED patterns of FeO(111) film before (left) and after (right) 40 mbar CO + 20 mbar O<sub>2</sub> reaction at 450 K for 120 min (LEED: 60 eV)  
(provided by Yingna Sun, PhD thesis, FU Berlin (2010))

In order to confirm this suspicion, we investigated the morphology of the system using STM. Fig. 4.5 shows a comparison between the morphology of pristine FeO(111) film (a), FeO(111) film after 40 mbar CO + 20 mbar O<sub>2</sub> reaction at 450 K for 120 min (b) and Pt(111) single crystal after the same reaction (c).

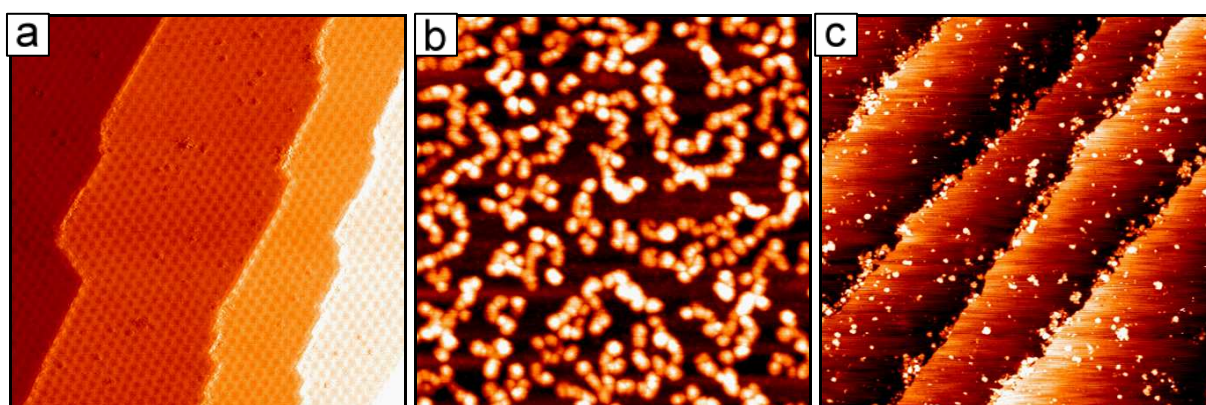


**Fig. 4.5** STM images: pristine FeO(111) film (a), the film after 40 mbar CO + 20 mbar O<sub>2</sub> reaction at 450 K for 120 min (b) and Pt(111) single crystal after the same reaction (c) (STM: 100 x 100 nm<sup>2</sup>, 0.7 V, 0.4 nA (a); 200 x 200 nm<sup>2</sup>, 0.8 V, 0.5 nA (b) and 200 x 200 nm<sup>2</sup>, 0.5 V, 0.3 nA (c))

Pt(111) single crystal did not seem to be affected by the reaction. It maintained the typical crystal morphology even after 120 min in the reaction (Fig. 4.5(c)). Very small particles which were observed on the crystal's surface after the reaction could be, on the basis of AES results (not shown), attributed to carbon formed by CO dissociation on low-coordinated Pt sites, as no oxygen signal was observed in the spectrum. For FeO(111) the results revealed that the film dewets during the reaction which results in a formation of randomly distributed particles. The particles had a narrow size distribution: most of them were  $8 \pm 1$  nm in diameter and  $1.8 \pm 0.1$  nm in height. The AES results revealed the presence of iron, oxygen and carbon on the surface (not shown). Surprisingly, O:Fe ratio turned out to be higher than for the pristine FeO(111) film and corresponded to FeO<sub>1.3</sub> stoichiometry. TDS results revealed that only CO and CO<sub>2</sub> were desorbing from the surface when heating to 800 K (not shown). The desorption profiles were similar to the profiles obtained for CO adsorbed on clean Pt(111), but the amount of desorbing molecules was found to be by ~30 % lower. The finding was in agreement with STM results which showed that a large fraction of Pt(111) surface was exposed after the reaction due to FeO(111) film dewetting, but the surface was still partially covered with small iron oxide Fe<sub>x</sub>O<sub>y</sub>C<sub>z</sub> particles (Fig. 4.5(b)).

In order to see how the dewetting proceeds, we exposed FeO(111) film to a mixture of 40 mbar CO + 20 mbar O<sub>2</sub> at 450 K for 10 min. Fig 4.6(a) shows an STM image of the sample after the reaction. The results revealed that small particles started to appear on the surface due to FeO(111) film dewetting. In the regions between the particles, the original FeO(111) structure could still be seen. The morphology of the sample after 120 min in the reaction (where a complete dewetting was observed) is shown for comparison in Fig. 4.6(b). Next, we stepwise annealed the fully dewetted sample to 500, 700 and 800 K in order to see if the film will wet the surface again. Fig. 4.7 shows an STM images of the dewetted sample as prepared (a) and after subsequent annealing steps ((b)-(d)). It was found that high temperature annealing forced the film to wet the surface again and restored the original stoichiometry of FeO<sub>(1)</sub> (as judged from AES results; not shown). In addition, FeO(111) satellite LEED pattern became visible again (not shown). All this indicated that iron remained on the surface after the CO + O<sub>2</sub> reaction and was not consumed in a production of volatile products.

---



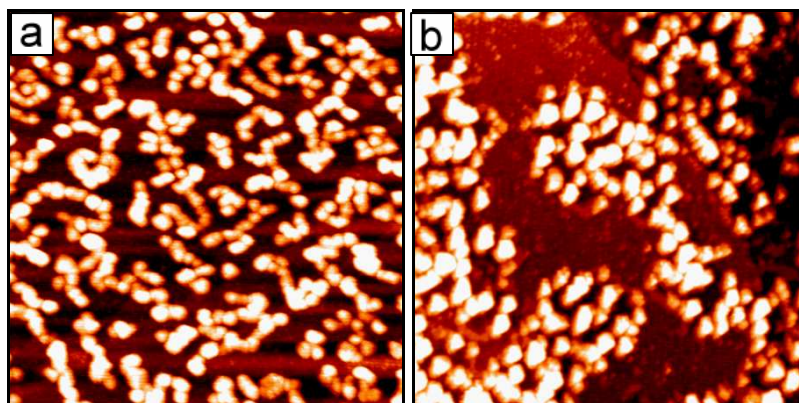


**Fig. 4.6** STM images of FeO(111) films: after 40 mbar CO + 20 mbar O<sub>2</sub> reaction at 450 K for 10 min (a) and after 120 min in the reaction (b) (STM: 200 x 200 nm<sup>2</sup>, 0.8 V, 0.4 nA (a) and 0.7 V, 0.4 nA (b))

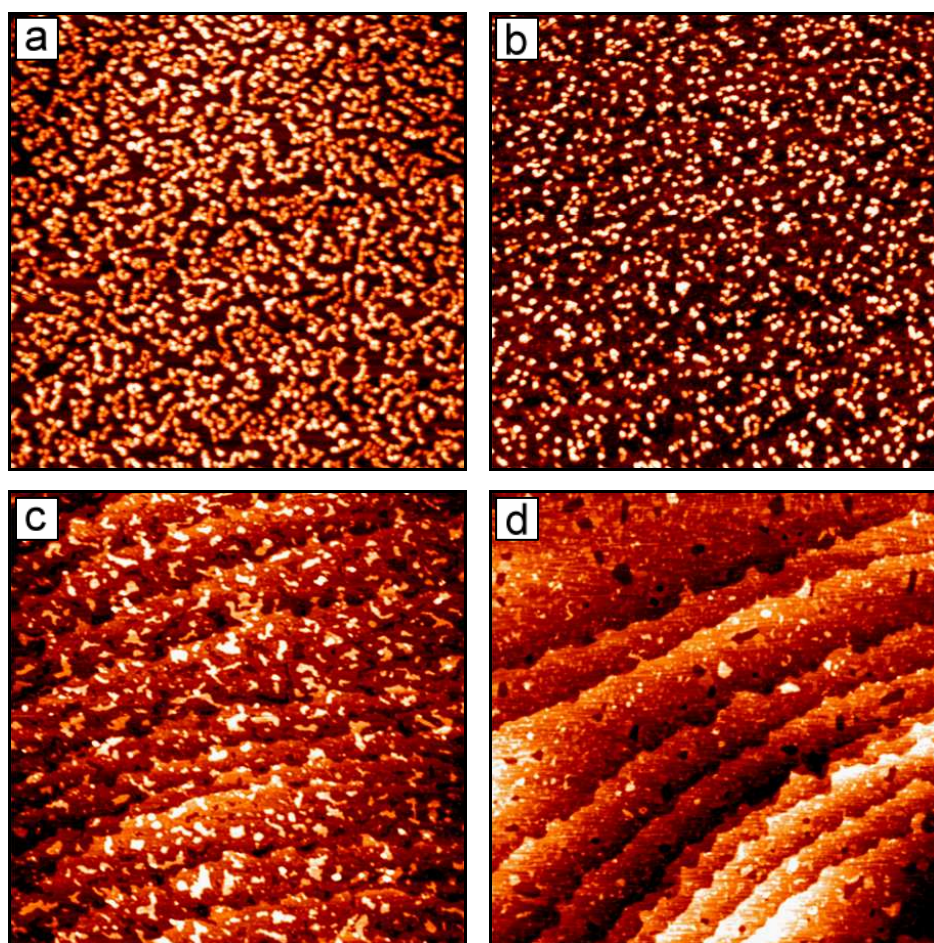


**Fig. 4.7** STM images of FeO(111) film after 120 min in 40 mbar CO + 20 mbar O<sub>2</sub> reaction at 450 K (a) and subsequent stepwise annealing at 500 (b), 700 (c) and 800 K (d) (STM: 500 x 500 nm<sup>2</sup>; 0.8 V, 0.5 nA (a); 0.8 V, 0.5 nA (b); 0.8 V, 0.5 nA (c) and 0.9 V, 0.6 nA (d))

The results suggested that:

- 1) In O-lean conditions FeO(111) film dewets which can explain the decrease in CO<sub>2</sub> production rate with time.
- 2) The highest rate is observed in the beginning of the reaction when the film is not dewetted.
- 3) The reaction slows down as the dewetting proceeds.
- 4) When maximum dewetting is observed, the rate remains constant and is very similar to the rate observed for Pt(111) single crystal.

Therefore, the enhanced reactivity of the system can be attributed to FeO(111) film rather than the particles formed upon dewetting.

### 4.3.3 O-rich conditions

We focused on the detailed investigation of sustained reactivity of FeO(111) films in O-rich conditions. AES results revealed that after the reaction the film becomes enriched with oxygen (without losing iron) and approach the stoichiometry of FeO<sub>2</sub> (not shown). In order to explain the oxygen enrichment we exposed pristine FeO(111) films to high pressures of CO and O<sub>2</sub> separately. After the millibar CO treatment at 450 K no significant changes in morphology and / or stoichiometry of the film were observed (as judged by LEED, AES and STM). The film seemed to be inert to CO even at millibar pressures. After exposure to millibar pressures of oxygen at 450 K, the appearance of higher order satellite spots (Fig. 4.8(b)), as compared to pristine FeO(111) films (Fig. 4.8(a)), could be observed in the LEED.

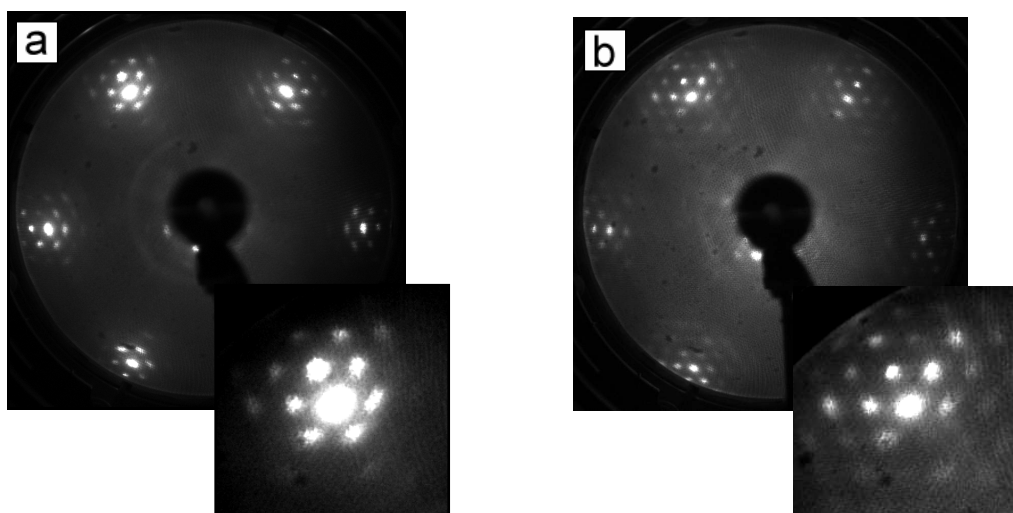


**Fig. 4.8** LEED patterns of FeO(111) film as prepared (a) and after exposure to 50 mbar O<sub>2</sub> at 450 K for 10 min (b); insets: zoom with enhanced contrast (LEED: 64 eV)

STM revealed a transformation of the FeO(111) film into a superstructure with a long-range periodicity quite similar to the original film (Fig. 4.9(a)). The surface seemed to have a multi-domain structure consisting of well-ordered “patches” / “islands”. Interestingly, FeO(111) was found to undergo the same transformation also at RT, but longer time was needed. Short treatment at RT resulted in partial transformation. Fig. 4.9(b) shows an FeO(111) film after 2 mbar O<sub>2</sub> treatment at RT, where partial reconstruction was observed. Partial transformation gave the possibility to identify the registry between the original FeO(111) and the superstructure patches. The patches seemed to use the Moiré pattern of the original FeO(111) film as a template. The corrugation amplitudes of the unreconstructed and reconstructed surfaces were imaged by profile lines shown in Figs. 4.9(c) and 4.9(d). The height modulation amplitude within the superstructure was  $\sim 0.6 \text{ \AA}$  (independent on the bias polarity) (Fig. 4.9(c)). That is much higher than  $\sim 0.1 \text{ \AA}$  observed for pristine FeO(111) films under the same tunneling conditions (Fig. 4.9(d)). Profile line in Fig. 4.9(d) made the determination of height difference between the original FeO(111) film and the superstructure patches possible. It was found to be  $\sim 0.65 \text{ \AA}$ , very similar to an interlayer distance between Fe and O planes in FeO(111) / Pt(111). High corrugation amplitude of the superstructure, as well as the height of the patches, indicated that the surface between the patches exposes unreconstructed FeO(111).

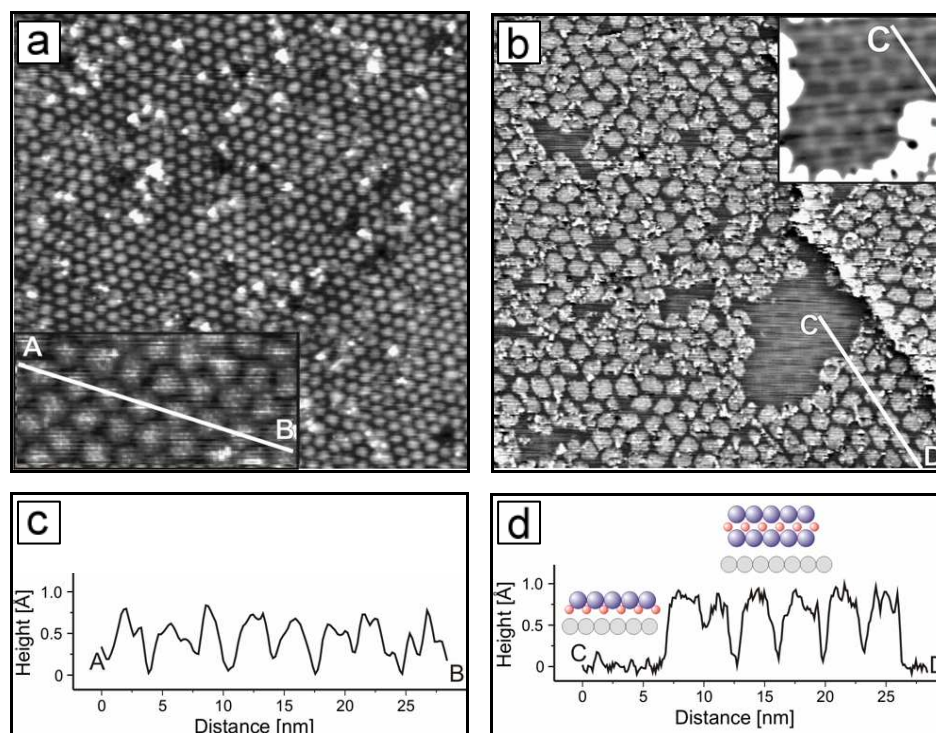


**Fig. 4.9** STM images of FeO(111) films: exposed to 20 mbar O<sub>2</sub> at 450 K for 10 min (a) and exposed to 2 mbar O<sub>2</sub> at 300 K for 5 h (b); insets: zoom of the structures; profile lines show surface corrugation amplitudes (c, d) (STM: 100 x 100 nm<sup>2</sup>, 1.0 V, 0.7 nA (a) and 50 x 50 nm<sup>2</sup>, 0.25 V, 0.3 nA (b))  
 ((b) provided by Shamil Shaikhutdinov)

In addition, STM revealed that the atomic arrangement within the patches is a  $(\sqrt{3} \times \sqrt{3})R30^\circ$  structure, with respect to the original FeO(111) (Figs. 4.10(a)-(c)). STM images of the samples oxidized at RT (where both pristine FeO(111) and reconstructed O-rich superstructure could be seen) revealed that the Moiré lattice of the oxidized FeO<sub>2</sub> patches was expanded by  $\sim 3\%$ , as compared to the original FeO(111) film (Figs. 4.9(b) and 4.10(b)). For the samples oxidized at 450 K, for which a uniform transformation across the whole surface was observed, the expansion was found to be even higher, up to  $\sim 10\%$  (difficult to measure precisely). The general knowledge is that an inverse relation appears between the lattice constants of the layers which contribute to the Moiré pattern and the periodicity of the superstructure itself. There is also a relation between the rotation of the lattices with respect to each other and the superstructure's periodicity. In case of FeO(111) there is no rotation of the lattices which means that the smaller the lattice constant of FeO(111), the larger the unit cell of the Moiré

(and vice versa). As mentioned, STM results revealed that the Moiré periodicity of the FeO<sub>2</sub> patches was larger by ~3 %, as compared to the Moiré of FeO(111) which would indicate that the lattice constant of FeO<sub>2</sub> is slightly smaller than that of FeO(111).

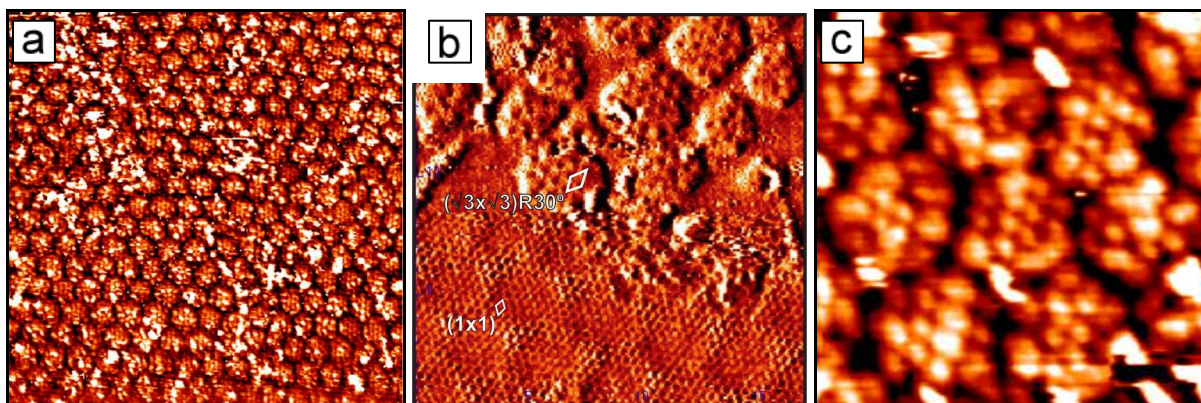


**Fig. 4.10** STM images of FeO(111) films: exposed to 14 mbar O<sub>2</sub> at 450 K for 10 min (a, c) and 0.5 mbar O<sub>2</sub> at 350 K for 10 min where both unreconstructed and reconstructed regions showing ( $\sqrt{3}\times\sqrt{3}$ )R30° structure are resolved on the same image (b) (STM: 50 x 50 nm<sup>2</sup>, 0.25 V, 0.7 nA (a); 50 x 50 nm<sup>2</sup>, 1.0 V, 0.7 nA, differentiated contrast (b) and 10 x 10 nm<sup>2</sup>, 0.1 V, 0.7 nA (c))

To verify this hypothesis we performed a comparative analysis of the LEED patterns of FeO(111) and FeO<sub>2</sub> films. The Pt(111) and FeO(111) diffraction spots could be clearly distinguished on both patterns, so that the distances between the spots could be measured (Fig. 4.8). The analysis revealed that upon high-pressure oxidation the lattice constant of the film indeed decrease from 3.09 Å to 3.05 Å (or by ~1.5 %) on average. To accommodate these changes while maintaining the same coincidence superstructure, the transformation must be accompanied by a rotation of the top layer with respect to Pt(111) substrate. This could explain the “patches”-like morphology of the O-rich films which would consist of domains rotated in a slightly different way. Another explanation may be related to differences in transformation of different crystallographic domains within the Moiré unit cell (for details please refer to Chapter 1.4). It could be that with increasing O<sub>2</sub> pressure and surface temperature different domains became transformed. This could explain why the patches were smaller and rather irregularly shaped in case of FeO(111) film exposed to 2 mbar O<sub>2</sub> at RT, as compared to the film treated with 50 mbar O<sub>2</sub> at 450 K (Fig. 4.9). A

formation of continuous film was probably not possible because not all the domain types could be transformed at the reaction conditions studied. Interestingly, even oxidation at high temperature, such as exposing the film to 10 mbar O<sub>2</sub> at 700 K for 10 min, did not result in complete transformation (Fig. 4.11(a)). It was observed, that after such treatment additional worm-like “borders” were formed between larger regions of the superstructure. To determine the nature of these structures more detailed studies are necessary, however, they could arise from lattice mismatch between the film and the support. AES results indicated that after the oxidation the film maintained the stoichiometry of FeO<sub>2.33</sub> (not shown). Interestingly, the LEED pattern became very diffuse and higher order spots characteristic for the superstructure could not be seen (Fig. 4.11(b)).

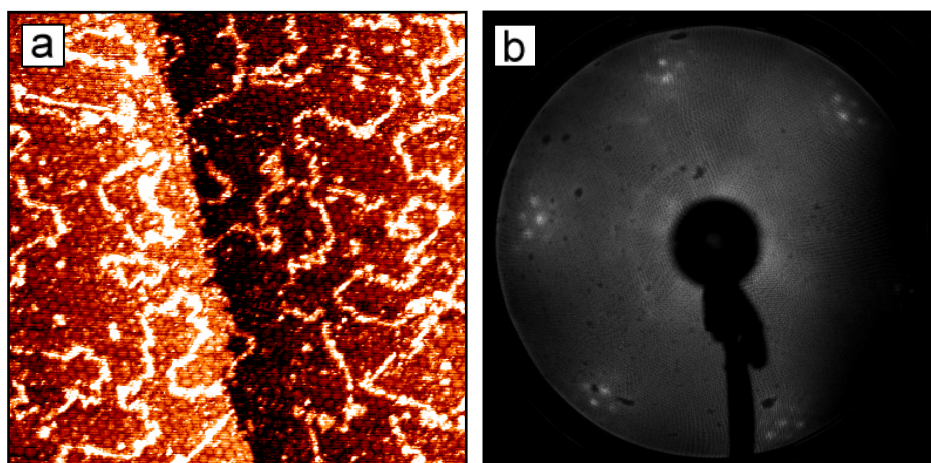


**Fig. 4.11** STM image (a) and LEED pattern (b) of FeO(111) film exposed to 10 mbar O<sub>2</sub> at 700 K for 10 min (LEED: 64 eV; STM: 100 x 100 nm<sup>2</sup>, 1.0 V, 0.7 nA)

We decomposed both the pristine FeO(111) and the superstructure by heating the films to high temperatures in front of the QMS and recording the O<sub>2</sub> (32 amu) desorption signal (Fig. 4.12). The pristine FeO(111) film exhibited a single ~1170 K desorption state, while the superstructure have shown an additional peak centered at ~840 K indicative for the presence of additional, more weakly bound oxygen on the surface. We calculated the total amount of the desorbing oxygen and found that the superstructure contains ~90 % more oxygen than the original FeO(111) film, with a significant contribution from the peak related to weakly-bound oxygen desorbing at ~840 K. This amount corresponds to the

stoichiometry of FeO<sub>1.8</sub>. The results were in perfect agreement with O:Fe ratios measured with AES both for FeO(111) films treated with high pressures of O<sub>2</sub> and FeO(111) films after CO oxidation reaction in O-rich conditions (not shown). The fact that the stoichiometry of the superstructure “O-rich” films was not exactly FeO<sub>2</sub> could be explained by incomplete transformation of FeO(111) to FeO<sub>2</sub>.

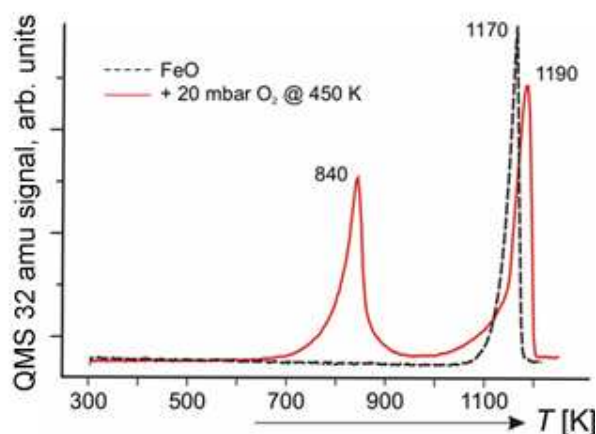


**Fig. 4.12** TDS of O<sub>2</sub> (32 amu signal): decomposition of pristine FeO(111) film (dashed line) and O-rich superstructure film formed upon FeO(111) exposure to 20 mbar O<sub>2</sub> at 450 K (solid line) (provided by Yingna Sun, PhD thesis, FU Berlin (2010))

On the basis of the experimental results we proposed a model of the reconstruction, according to which the film would transform from bilayer O–Fe/Pt structure into trilayer O–Fe–O/Pt-like “sandwich” structure. The model was supported by computational theoretical modeling. DFT calculations were provided by Livia Giordano, Jacek Goniakowski and Gianfranco Pacchioni. For details concerning the computational methods and models used in this work, please refer to [109, 110, 112]. First, an attempt was made to describe how the transformation from bilayer to trilayer structure proceeds. The computed enthalpy profile for the interaction of O<sub>2</sub> with FeO(111) film grown on Pt(111) is shown in Fig. 4.13:

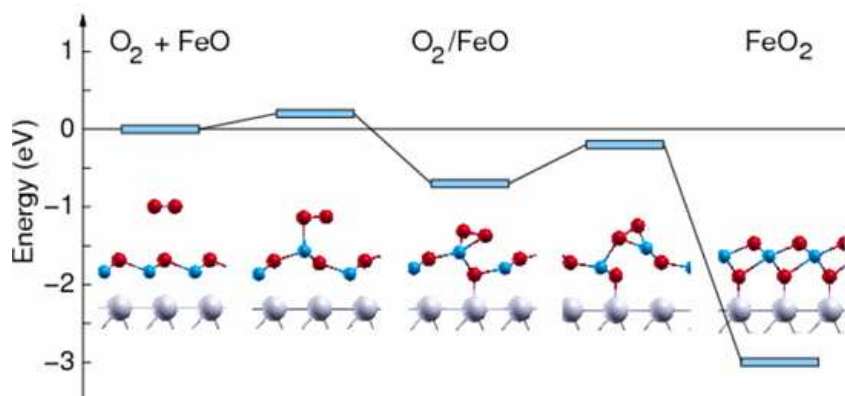


**Fig. 4.13** Calculated enthalpy profile for the interaction of  $O_2$  with FeO(111) film on Pt(111)  
(Fe blue, O red, Pt grey)

(provided by Livia Giordano, Jacek Goniakowski and Gianfranco Pacchioni)

According to the calculations, the transformation proceeds as follows:

- 1) By overcoming an energy barrier of 0.3 eV the  $O_2$  is molecularly chemisorbed (with adsorption energy of 0.7 eV) on the Fe atom which is pulled out from the pristine film. High oxygen pressure is necessary to overcome the adsorption barrier because thermal activation would result in  $O_2$  desorption.
- 2) Electrons are transferred from the metal / oxide substrate to the  $O_2$  molecule which becomes negatively charged.
- 3) The length of the O-O bond expands to 1.46 Å. Complete quenching of the magnetic moment indicates formation of peroxo species  $O_2^{2-}$ . The electron transfer is enabled mainly by a local inversion of the rumpling in the oxide film which locally lowers the work function of the support.
- 4) By overcoming an activation barrier of  $\sim 0.4$  eV the  $O_2$  molecule dissociates.
- 5) At high  $O_2$  coverage the formation of O adatoms results in a formation of trilayer O-Fe-O structure with a stoichiometry of  $FeO_2$ . The process is accompanied by a total



energy gain of 3 eV.

Next, the “patches”-like morphology of the O-rich superstructure was theoretically addressed. Ab-initio oxidation thermodynamics were calculated for different high-symmetry regions within the Moiré unit cell: fcc, top and hcp. The phase diagrams for FeO<sub>x</sub> films in these three regions are shown in Fig. 4.14. The transitions are plotted as a function of oxygen chemical potential  $\mu_O$ . The increase of oxygen partial pressure induces a progressive stabilization of the phases with higher oxygen content. Alternative configurations for each oxide stoichiometry were considered and optimized, but only the most stable for each are plotted.

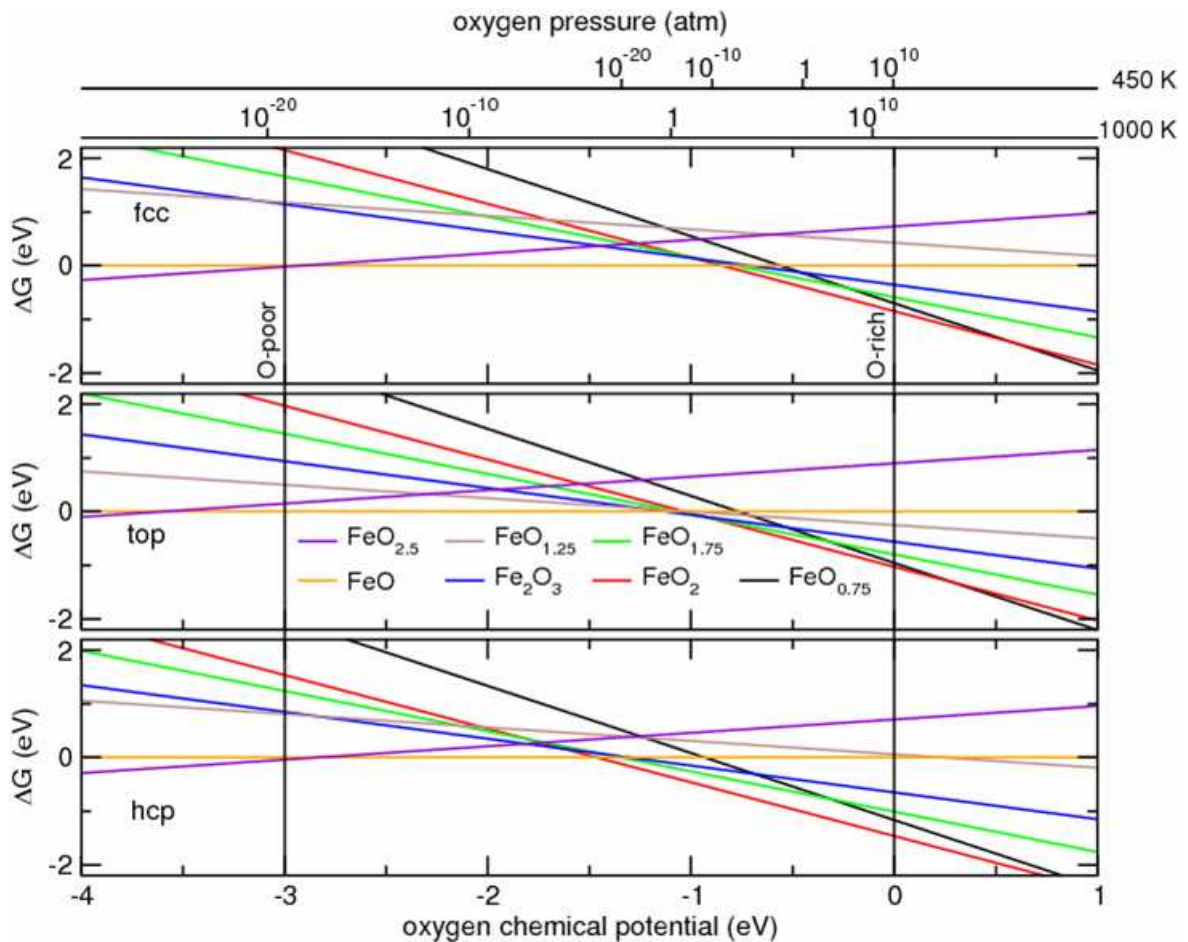


**Fig. 4.14** Phase diagrams for FeO<sub>x</sub> films in three high symmetry regions of the FeO(111) Moiré unit cell as a function of oxygen chemical potential  $\mu_O$  (provided by Livia Giordano, Jacek Goniakowski and Gianfranco Pacchioni)

The interpretation of the diagrams is as follows:

- (i) In extremely O-lean conditions ( $\mu_O < -3.0$  eV) oxygen vacancies are formed in the FeO film due to considerable vacancy formation energy (violet lines).
- (ii) The FeO film is stable in a relatively wide range of oxygen chemical potential. The stability is different for different regions within the Moiré unit cell (it extends up to  $\mu_O = -0.8$  eV,  $-1.1$  eV, and  $-1.5$  eV for fcc, top and hcp regions respectively; orange lines).
- (iii) For high  $\mu_O$  values the O-rich phase FeO<sub>2</sub> is directly stabilized in the hcp and fcc regions (red lines), while in the top region it involves a stable intermediate phase with Fe<sub>2</sub>O<sub>3</sub> stoichiometry (for  $-1.1$  eV  $< \mu_O < -0.9$  eV; blue line).
- (iv) Adsorption of additional oxygen on the FeO<sub>2</sub> film requires extremely O-rich conditions ( $\mu_O > 0.5$  eV).

The calculated phase diagrams show that different oxide phases may compete and / or coexist within the Moiré structure under certain oxidation conditions. In particular, at low oxygen pressure ( $\mu_O \sim -1.3$  eV) a formation of FeO<sub>2</sub> structure in the hcp regions of the FeO(111) / Pt(111) Moiré could be expected. The enhanced stability of the O-rich phase in the hcp region is driven by short covalent Pt-O bonds which are formed due to preferential O on-top Pt geometry. At higher oxygen pressure ( $\mu_O \sim -1.0$  eV) FeO<sub>2</sub> in the hcp regions should coexist with an intermediate oxide phase in the top regions. Finally, at high oxygen pressures ( $> \mu_O \sim -1.0$  eV) the FeO<sub>2</sub> trilayer should cover the entire Pt(111) surface. The experimental situation is much more complex. The structures which are present at different stages of oxidation process may tend to change their local registry with respect to the substrate in order to optimize the interface energy. Nevertheless, regardless the region within the Moiré the FeO<sub>2</sub> film is believed to have a trilayer structure with atomic layers in fcc stacking.

Finally, efforts were made to rationalize the experimentally observed ( $\sqrt{3} \times \sqrt{3}$ )R30° atomic arrangement within the FeO<sub>2</sub> patches. The ( $\sqrt{3} \times \sqrt{3}$ )R30° structure could be obtained

---

for example by removing 1/3 or 2/3 of Fe atoms or top-layer O atoms. As mentioned earlier, AES results showed that the amount of Fe does not change during the transformation. Removal of oxygen would result in  $\text{FeO}_{1.66}$  or  $\text{FeO}_{1.33}$  stoichiometries, respectively, which is also not the case as shown by AES and TDS results. The observed structure did not seem to depend on the STM tunneling conditions and bias polarity. The STM contrast is believed to be determined by Fe (rather than O) species forming electronic states near the Fermi level. Thus, it may be concluded that the  $(\sqrt{3}\times\sqrt{3})R30^\circ$  structure is related to Fe atomic arrangement. Optimization of the structure revealed that all interfacial O atoms adopt on quasi on-top positions of Pt and each atom forms a single short Pt-O bond which is the stabilizing mechanism. Two quasi-degenerate structures of the  $\text{FeO}_2$  trilayer film with respect to Fe atomic arrangement were found to be energetically favorable: the “planar” structure where all Fe atoms are in plane (Fig. 4.15(a)) and the “buckled” structure where the atoms are buckled (Fig. 4.15(b)).

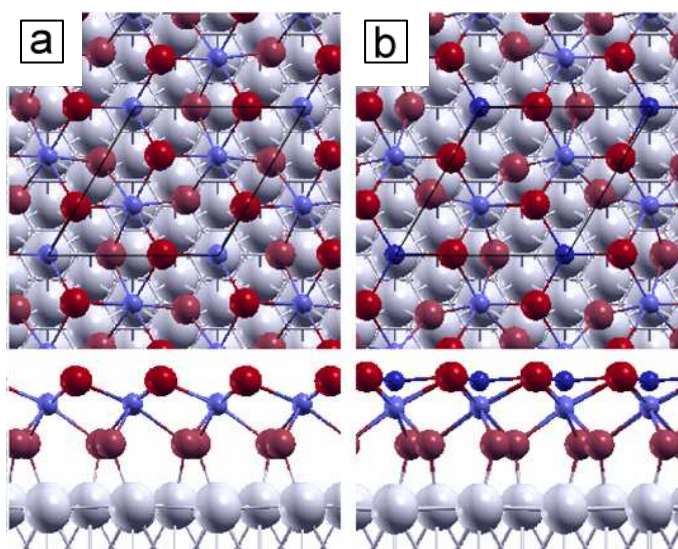


**Fig. 4.15** Energetically favorable quasi-degenerate structures of  $\text{FeO}_2$  trilayer: the “planar” (a) and the “buckled” structure (b) (provided by Livia Giordano, Jacek Goniakowski and Gianfranco Pacchioni)

The energy difference between the two structures was found to be very small ( $< 0.04$  eV in 0 K calculations), so it was difficult to state which of them is the structure experimentally observed. That is why both structures are discussed:

In the “planar” model all Fe ions are 6-fold coordinated and located in a similar distance to Pt(111) surface, thus forming a nearly flat Fe sublayer with an intra-layer corrugation  $< 0.08 \text{ \AA}$ . All O anions have three Fe neighbours. The film is asymmetric: the average Fe-O interlayer distance is  $1.23 \text{ \AA}$  at the interface side and  $0.75 \text{ \AA}$  at the surface side. All Fe ions are in  $\text{Fe}^{3+}$  oxidation state. An electron transfer from the metal substrate enables both surface and interface O ions to be in the  $\text{O}^{2-}$  state.

In the “buckled” model two out of three Fe ions in the unit cell are 6-fold coordinated, while the third ion flips outwards almost at the height of the top O layer. The corrugation amplitude within the Fe layer is  $0.87 \text{ \AA}$ . The surface of the film consists of a nearly flat layer of 3-fold coordinated Fe and O atoms with a well pronounced  $(\sqrt{3}\times\sqrt{3})R30^\circ$  symmetry. All O ions at the interface have two Fe neighbours.

STM images are dominated by the contrast from the ions in the top-most layer: surface O ions in case of the “planar” structure and both surface O ions, and the flipped Fe ions in case of the “buckled” film. The contribution of Fe ions is substantially different in the two structures: in the “planar” structure Fe ions contribute only a little to the STM contrast, while in the “buckled” film the 3-fold coordinated Fe ions dominate the STM image at all biases. As a consequence, three spots per  $(\sqrt{3}\times\sqrt{3})R30^\circ$  unit cell are visible for the “planar” structure, while only one spot appears in case of the “buckled” film. The simulated STM images compared with experimentally obtained image are shown in Figs. 4.16(a)-(c). The atomic periodicity observed on the simulated image of the “buckled” film was found to be in agreement with the periodicity observed experimentally (of course tip condition uncertainty has to be taken into account). This confirmed that the buckling within the Fe sublayer is responsible for the experimentally observed  $(\sqrt{3}\times\sqrt{3})R30^\circ$  structure. Interestingly, the fact that all Fe ions within the buckled film are in  $\text{Fe}^{3+}$  oxidation state, makes the structure similar to Fe-terminated  $\alpha\text{-Fe}_2\text{O}_3(0001)$ . This is in agreement with a general knowledge that the formation of bulk  $\alpha\text{-Fe}_2\text{O}_3$  is thermodynamically favorable at high oxygen pressures (see [10] and references therein). It is also known that under certain conditions  $\alpha\text{-Fe}_2\text{O}_3$  can be ferryl (Fe=O) terminated [126]. Our structure could be an intermediate state in the transformation from FeO to  $\text{Fe}_2\text{O}_3$ .

---

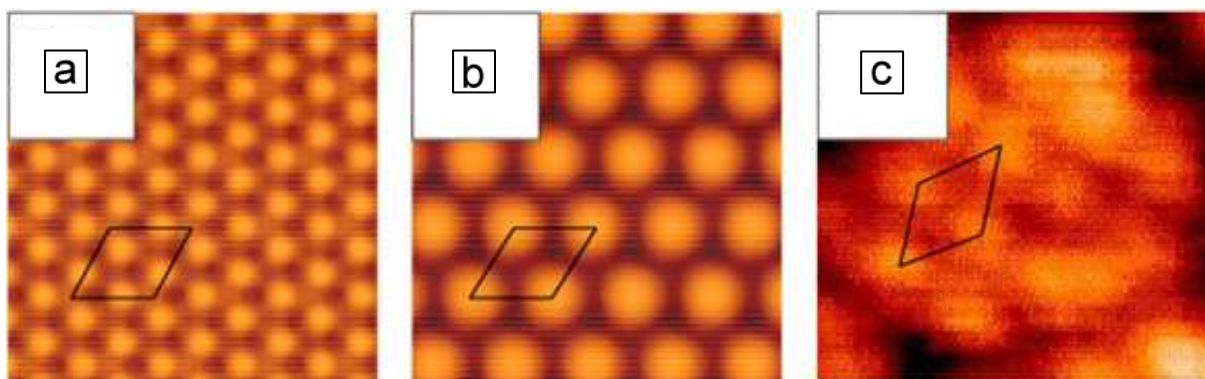


**Fig. 4.16** Comparison of simulated STM images for “planar” (a) and “buckled” (b) structures with experimentally obtained image (c) (simulated STM images:  $25 \times 25 \text{ nm}^2$ , 1.0 V, electron charge isodensity =  $1 \times 10^{-5} \text{ e}/\text{\AA}^3$  (a, b); STM:  $25 \times 25 \text{ nm}^2$ , 1.0 V, 0.7 nA (c))  
(a & b provided by Livia Giordano, Jacek Goniakowski and Gianfranco Pacchioni)

#### 4.3.4 Reaction mechanism

CO oxidation reaction on oxide surfaces usually follows the Mars-van Krevelen mechanism (for details please refer to Chapter 1.3). Generally speaking, CO is oxidized by the oxide lattice oxygen and the reduced catalyst is reoxidized by the gas phase oxygen. On FeO(111) the situation is more complex. The film was shown to be inert to CO even at millibar pressures. It is believed that the CO oxidation reaction proceeds via a transformation of FeO(111) film into an O-rich  $\text{FeO}_{2-x}$  superstructure which is the active oxide phase in this reaction. The O-rich films were found to be very active towards the molecules present in the background pressure of residual gases in the UHV chamber, mainly water and CO, as the films were becoming very “dirty” with time. It was proposed that the CO oxidation reaction on FeO(111) proceeds in three steps: (i) transformation of bilayer Fe-O film into trilayer O-Fe-O structure, (ii) reaction of CO with oxygen atoms in the topmost layer resulting in  $\text{CO}_2$  formation and desorption and (iii) replenishment of oxygen vacancies by the gas phase  $\text{O}_2$ . The proposed reaction mechanism was supported by theoretical DFT calculations. The computed enthalpy profile for (i) was shown in Fig. 4.13. The enthalpy profile for the  $\text{CO} + \text{FeO}_2/\text{Pt} \rightarrow \text{CO}_2 + \text{FeO}_2/\text{Pt}$  reaction ((ii)) is presented in Fig. 4.17:

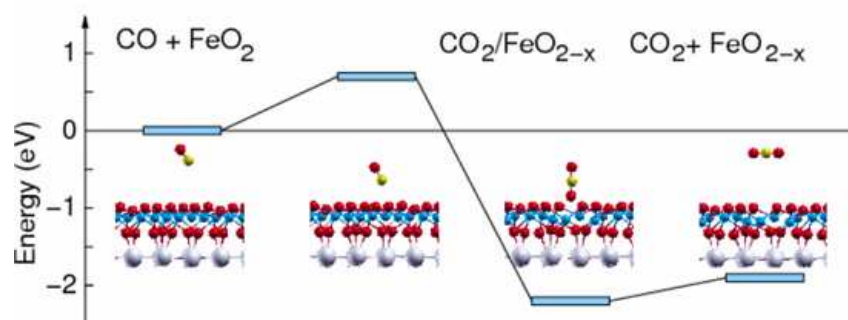


**Fig. 4.17** Calculated enthalpy profile for the  $\text{CO} + \text{FeO}_2/\text{Pt} \rightarrow \text{CO}_2 + \text{FeO}_{2-x}/\text{Pt}$  reaction

(Fe blue, O red, C yellow, Pt grey)

(provided by Livia Giordano, Jacek Goniakowski and Gianfranco Pacchioni)

According to the calculations, the interaction of CO with the O-rich film proceeds in the following way:

- 1) CO molecule approaches the surface of the O-rich film.
- 2) Near the  $\text{FeO}_2$  surface the CO molecule is, at most, physisorbed by overcoming an energy barrier of  $\sim 0.2$  eV.
- 3) CO strongly binds with the "C" end to one O ion in the topmost oxygen layer resulting in  $\text{CO}_2$  formation.
- 4)  $\text{CO}_2$  desorbs from the surface with an energy cost of 0.3 eV, leaving an oxygen vacancy.

In the proposed model CO interacts with the O-rich film via Eley-Rideal mechanism (for details please refer to Chapter 1.3). Because of low activation energy of the process, the reaction may indeed occur at lower temperatures than typically used for CO oxidation over Pt catalysts. It is important to note that in the proposed model only the reaction on flat  $\text{FeO}_2$  / Pt(111) terraces was considered. It is probable that the interaction at the border of  $\text{FeO}_2$  islands may occur at even lower energy cost. The formation of strong C–O bond in  $\text{CO}_2$

compensates the energy of removing an O atom from the film, such that the reaction is highly exothermic with a computed enthalpy of -1.9 eV. This is due to relatively low formation energy of oxygen vacancy on the FeO<sub>2</sub> / Pt(111) surface (1.3 eV with respect to 1/2 O<sub>2</sub>), about one-half of the energy calculated for the pristine FeO(111) film (2.8 eV). The findings are in agreement with TDS experiments where oxygen was found to desorb from the O-rich films at much lower temperature than from FeO(111) (840 K vs. 1170 K; Fig. 4.12). Therefore, the formation energy of oxygen vacancy is the key factor in the CO oxidation reaction over FeO(111) films. To end the catalytic cycle oxygen vacancies must be replenished by the gas phase O<sub>2</sub> (step (iii)). The restoration of the FeO<sub>2</sub> film may proceed through the mechanism shown in Fig. 4.13 or, alternatively, the oxygen vacancy could be filled by the gas phase O<sub>2</sub> which would then be transformed into a superoxo state O<sup>2-</sup> and the “dangling” O atom would react with CO molecule from the gas phase forming CO<sub>2</sub> (Fig. 4.18), thus regenerating the O-rich film in an exothermic reaction (by 4.3 eV) which has a very low activation barrier.

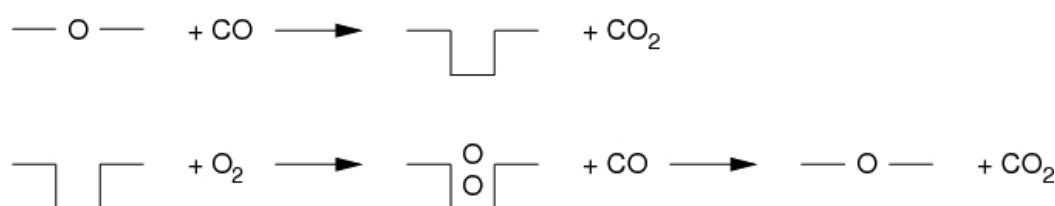


**Fig. 4.18** Schematic representation of the reaction pathways for CO interaction with O-rich film (top) and O<sub>2</sub> interaction with oxygen vacancy in the O-rich film (bottom)

In order to experimentally prove the proposed reaction mechanism, we performed the above mentioned reaction steps (i), (ii) and (iii) separately and subsequently: First the FeO(111) film was exposed to 50 mbar O<sub>2</sub> at 450 K for 10 min, than to 10 mbar CO at 450 K for 10 min and finally it was reoxidized using 50 mbar O<sub>2</sub> at 450 K for 10 min. STM characterization was performed after each reaction step. The results are summarized in Figs. 4.19(a)-(f). As expected, high pressure O<sub>2</sub> treatment resulted in a formation of O-rich superstructure (Fig. 4.19(a)). After exposing the O-rich phase to CO some surface regions were transformed back to FeO-like structure due to reaction of CO with O atoms in the

topmost layer resulting in CO<sub>2</sub> formation and desorption (Fig. 4.19(b)). The inset in Fig. 4.19(b) shows the  $\sim 3$  Å atomic periodicity characteristic for FeO(111), obtained within the chemically reduced patches. When the sample was reoxidized the FeO<sub>2</sub> structure was fully recovered (Fig. 4.19(c)). The same trend was observed in the corresponding LEED patterns (Figs. 4.19(d)-(f)). The experiment confirmed the Mars-van Krevelen type mechanism predicted for this reaction.

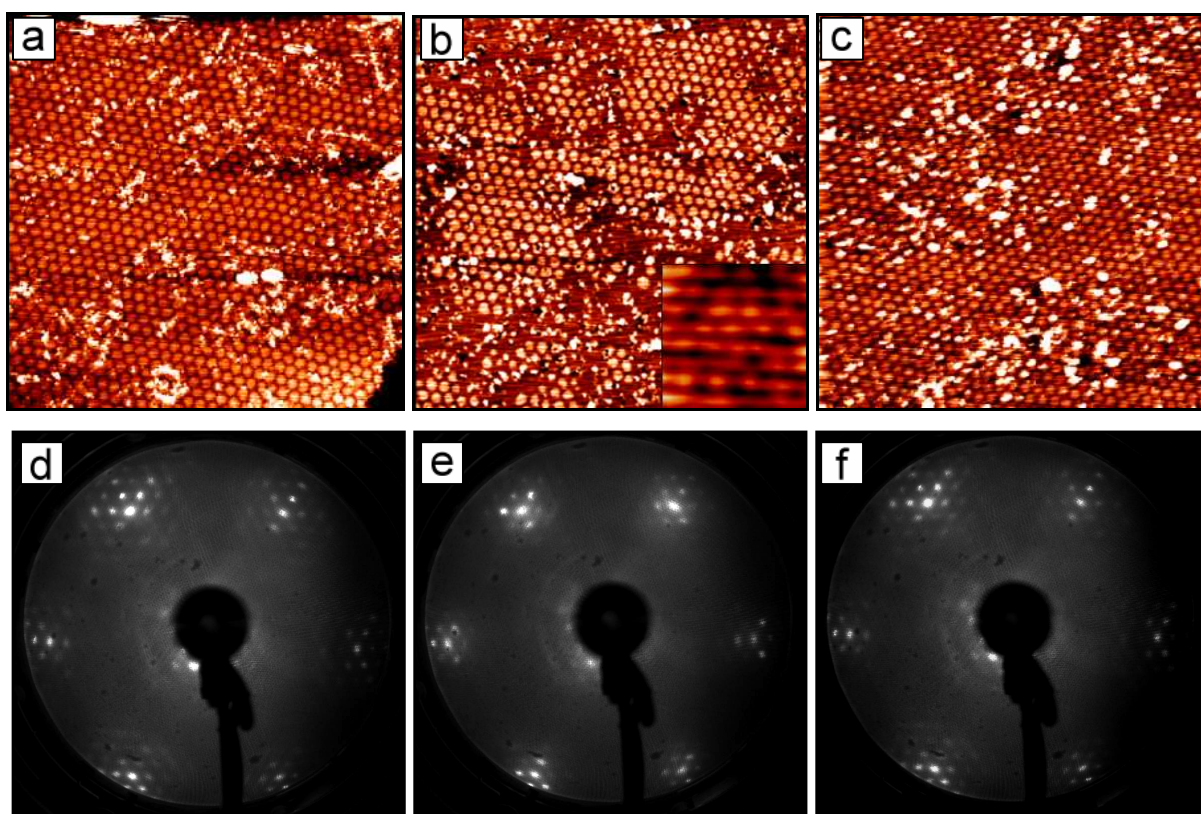


**Fig. 4.19** STM images and LEED patterns of FeO(111) film: after 50 mbar O<sub>2</sub> treatment at 450 K for 10 min (a, d), after 10 mbar CO treatment at 450 K for 10 min (b, e) and after reoxidation with 50 mbar O<sub>2</sub> at 450 K for 10 min (c, f); inset in (b) shows atomic structure within the reduced patches (STM: 100 x 100 nm<sup>2</sup>, 1.0 V, 0.7 nA (a); 100 x 100 nm<sup>2</sup>, 1.0 V, 0.7 nA (b); 1.75 x 1.75 nm<sup>2</sup>, 0.25 V; 0.7 nA (inset in b) and 100 x 100 nm<sup>2</sup>, 1.4 V, 0.7 nA (c); LEED: 64 eV)



#### 4.3.5 CO + O<sub>2</sub> vs. CO + NO

Inspired by the enhanced reactivity of FeO(111) films in CO + O<sub>2</sub> reaction, we addressed the question whether the effect would be similar if NO is used instead of O<sub>2</sub> as an oxidative agent. A comparison of the two could be helpful in understanding the reactivity of ultrathin oxide films. Blank experiments revealed that FeO(111) is essentially inert to NO at pressures up to 10<sup>-3</sup> mbar (not shown). However, when exposed to millibar pressures of the gas, the film transforms into a superstructure which is virtually identical to the one observed after millibar O<sub>2</sub> treatment (Fig. 4.20(c)). Long-range ordering could be seen in LEED and STM (Figs. 4.20(a) and 4.20(b)).

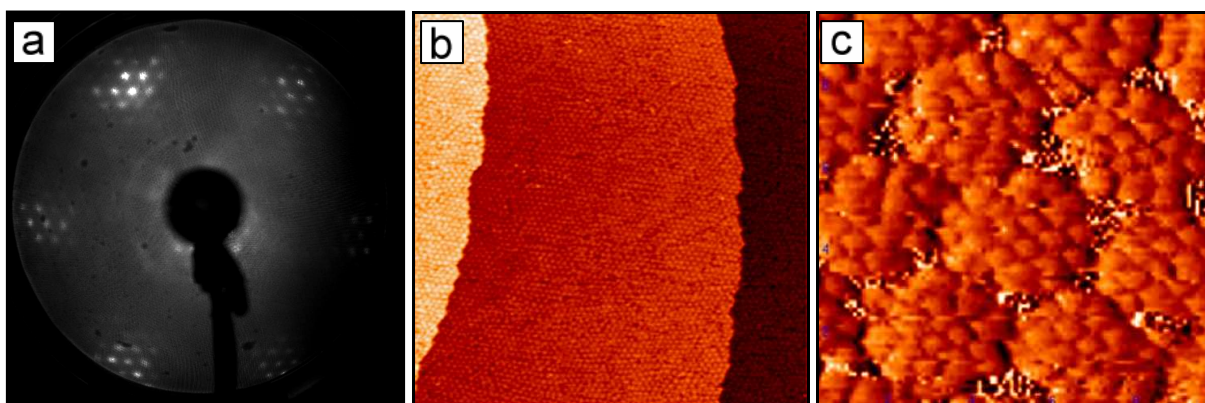


**Fig. 4.20** LEED pattern and STM images of FeO(111) film exposed to millibar pressures of NO: 20 mbar at 450 K for 10 min (a), 2 mbar at 450 K for 10 min (b) and 0.7 mbar at 300 K for 1 min (c) (LEED: 64 eV; STM: 200 x 200 nm<sup>2</sup>, 1.4 V, 0.7 nA (b) and 10 x 10 nm<sup>2</sup>, 1.0 V, 0.7 nA (c))

We decomposed the NO-treated films in front of the QMS and compared the results with those obtained for O<sub>2</sub>-treated FeO(111). Fig. 4.21 shows the O<sub>2</sub> desorption spectra as a function of temperature for the FeO<sub>2</sub> films formed with O<sub>2</sub> and NO at 300 and 450 K.

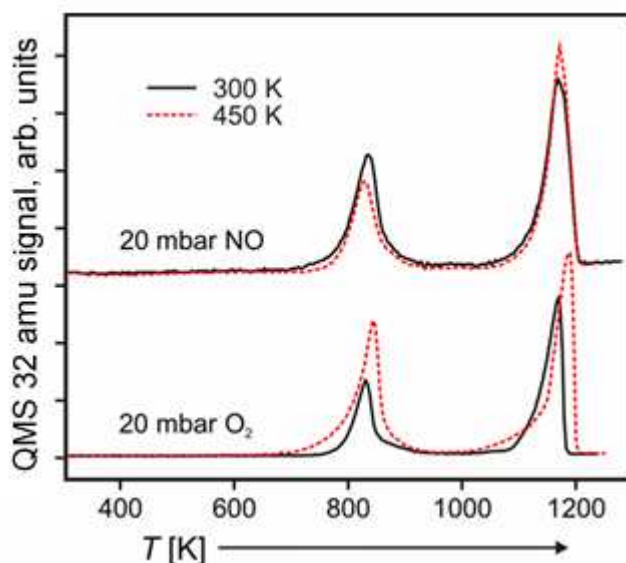


**Fig. 4.21** TDS of O<sub>2</sub> (32 amu signal): decomposition of O-rich films formed upon exposure to 20 mbar NO (top) and O<sub>2</sub> (bottom) at 300 and 450 K (solid and dashed lines respectively) (provided by Yingna Sun, PhD thesis, FU Berlin (2010))

In all the cases two desorption states were observed:  $\sim 840$  K and  $\sim 1190$  K. Only O<sub>2</sub> was desorbing from the samples which indicated that nitrogen was not incorporated into the NO-treated films and probably desorbed in a form of N<sub>2</sub> during the FeO  $\rightarrow$  FeO<sub>2</sub> transformation. Nitrogen peaks were also not observed in the AES spectrum (not shown). When the transformation was carried at 450 K, the intensities of oxygen peaks for NO- and O<sub>2</sub>-treated films were almost identical. Similar oxygen enrichment after oxidation at 450 K was also confirmed by AES results where the oxygen-to-iron ratio increased by the same order (not shown). For the NO-treated films the calculated O:Fe ratio was  $1.6 \pm 0.1$  independently on the reaction temperature. In case of O<sub>2</sub>-treated FeO(111) it was 1.5 for the reaction carried at 300 K and 1.9 for the reaction at 450 K. Even though the NO- and O<sub>2</sub>-treated films formed at 450 K had similar structure and stoichiometry the NO was found to be much better oxidative agent: FeO(111) was entirely transformed into O-rich superstructure upon exposure to 0.7 mbar NO at RT for 1 min while it still exhibited patches of unreconstructed surface after 5 hours in 2 mbar O<sub>2</sub> at the same temperature (please compare Fig. 4.20(b) with Fig. 4.9(b)). Therefore, it appeared that NO exhibits a lower activation barrier for the transformation. This would be in agreement with the

thermodynamics of the  $\text{FeO} + \text{NO} \rightarrow \text{FeO}_2 + 1/2 \text{N}_2$  reaction which is more exothermic than the  $\text{FeO} + 1/2 \text{O}_2 \rightarrow \text{FeO}_2$  due to additional energy gain ( $\sim 0.9$  eV) related to exothermic  $\text{NO} \rightarrow 1/2 \text{O}_2 + 1/2 \text{N}_2$  reaction.

Next, we studied the high pressure / low temperature CO oxidation reaction over FeO(111) films using CO + NO mixture and compared the results with CO + O<sub>2</sub> reaction over the same catalyst. Both reactions were carried in the O-rich (NO-rich) conditions using 50 mbar NO (O<sub>2</sub>) and 10 mbar CO. The reaction temperature was 450 K in both cases. The gas mixtures were balanced with He to 1 bar. We also performed additional experiments in which: (i) FeO(111) film was preconditioned with 20 mbar O<sub>2</sub> at 450 K for 10 min prior to CO + NO reaction and (ii) the film was preconditioned with 20 mbar NO at 450 K prior to CO + O<sub>2</sub> reaction. The results on CO<sub>2</sub> production in CO + O<sub>2</sub> reaction on pristine FeO(111), CO + NO on pristine FeO(111), CO + O<sub>2</sub> on NO pre-conditioned FeO(111) and CO + NO on O<sub>2</sub> pre-conditioned FeO(111) films are summarized in Fig. 4.22:

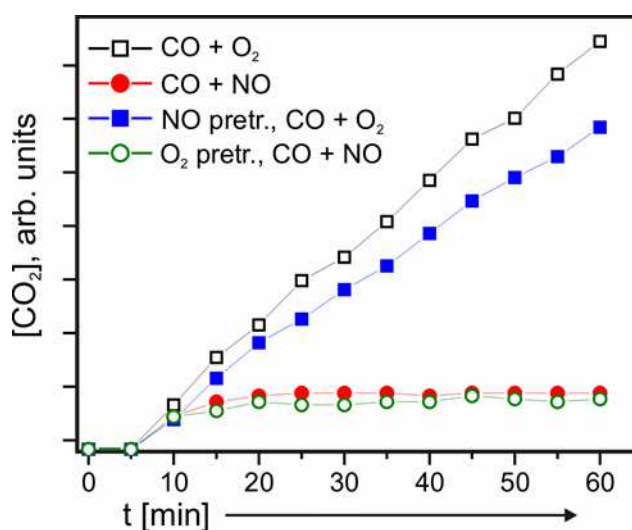


**Fig. 4.22** Kinetics of CO<sub>2</sub> production: CO + O<sub>2</sub> reaction on pristine FeO(111) film (white squares), CO + NO on FeO(111) (red circles), CO + O<sub>2</sub> on NO pre-conditioned FeO(111) (blue squares) and CO + NO on O<sub>2</sub> pre-conditioned FeO(111) (white circles) (provided by Yingna Sun, PhD thesis, FU Berlin 2010 and Yulia Martynova)

The CO + NO reaction showed almost zero CO<sub>2</sub> yield, no matter if the reaction was carried over pristine or O<sub>2</sub>-preconditioned FeO(111) (open and filled circles respectively). In case of CO + O<sub>2</sub> reaction the CO<sub>2</sub> yield was very high, no matter if the film was pretreated with NO or not (filled and open squares).

In order to rationalize the near-zero CO<sub>2</sub> production in CO + NO reaction we performed a detailed study of all the reaction steps using STM and LEED. First the FeO(111) film was treated with 20 mbar NO at 450 K for 10 min. Upon NO treatment the FeO(111) film transformed from bilayer O-Fe into trilayer O-Fe-O structure (Figs. 4.23(a) and 4.23(d)). Next, the sample was exposed to 10 mbar CO at 450 K for 10 min. CO interacted with the O-rich film forming CO<sub>2</sub> which desorbed leaving oxygen vacancies. STM revealed film dewetting, in agreement with LEED which showed only very diffuse spots of Pt(111) (Figs. 4.23(b) and 4.23(e)). Finally, an attempt was made to reoxidize the sample using 20 mbar NO at 450 K for 10 min. However, the film did not recover after dewetting caused by CO treatment (Figs. 4.23(c) and 4.23(f)). This indicated that the oxygen replenishment is the rate-limiting step in this reaction. That is somehow surprising due to the fact that NO seemed to be much more active than O<sub>2</sub> in O-rich phase formation. For the CO + NO reaction it appeared that after a single event of CO<sub>2</sub> production the reaction stops and a dewetted, disordered and partially reduced film is formed. Interestingly, these dewetted films could also not be recovered by high pressure O<sub>2</sub> treatment.

We also studied the morphology of the sample after the reaction where CO + NO mixture was used. The reaction was carried in NO-rich conditions (50 mbar NO + 10 mbar CO at 450 K for 10 min). The post-characterization of the spent catalyst revealed significant differences as compared to the samples exposed to CO + O<sub>2</sub> (same pressures and temperature). After the CO + O<sub>2</sub> reaction in the O-rich conditions the LEED pattern was still FeO(111)-like and the film was not dewetted (not shown). After CO + NO reaction the LEED pattern was very diffuse and only Pt(111) spots were visible (not shown). STM images revealed that the film dewetted (Fig. 4.24(a)), similarly to FeO(111) after CO + O<sub>2</sub> reaction in O-lean conditions (Fig. 4.24(b)). However, in case of CO + NO reaction the film did not dewet into small particles but few nm high worm-like structures.

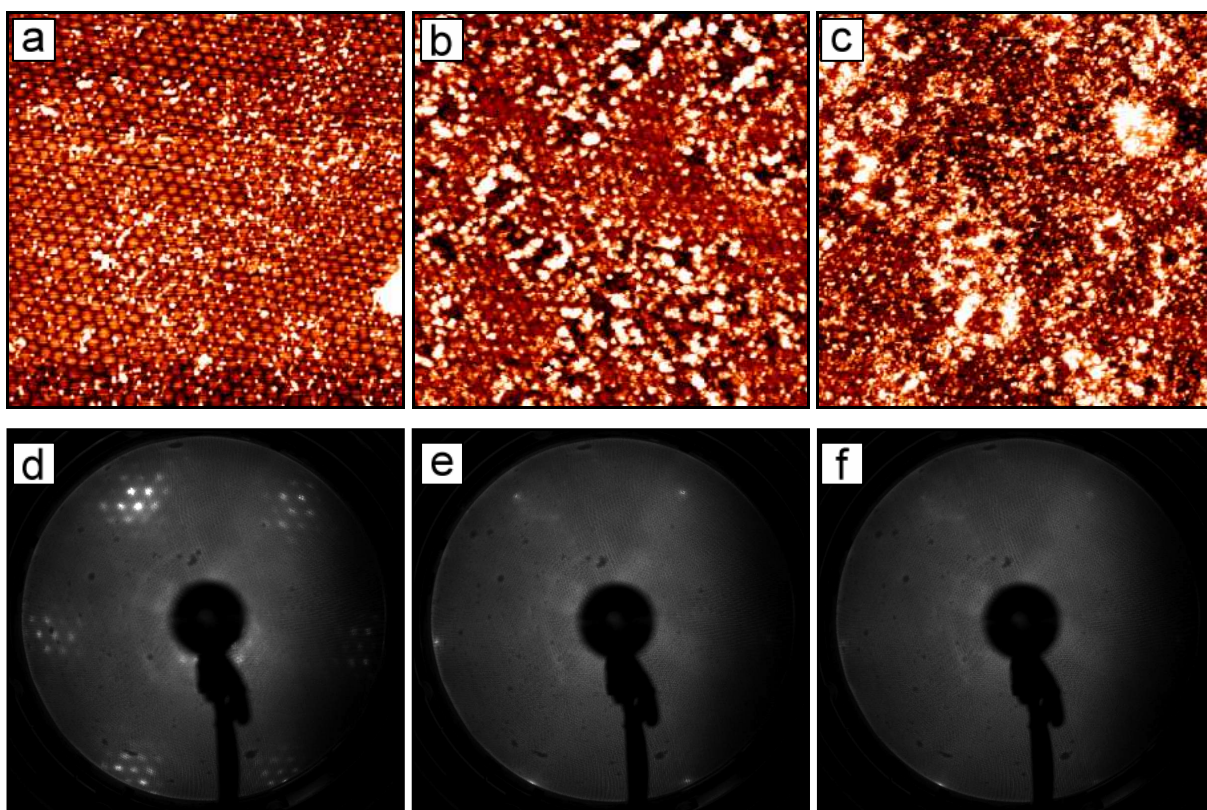


**Fig. 4.23** STM images and LEED patterns of FeO(111) film: after 20 mbar NO treatment at 450 K for 10 min (a, d), after 10 mbar CO treatment at 450 K for 10 min (b, e) and after reoxidation with 20 mbar NO at 450 K for 10 min (c, f) (STM:  $100 \times 100 \text{ nm}^2$ , 1.0 V, 0.7 nA (a);  $100 \times 100 \text{ nm}^2$ , 1.0 V, 0.7 nA (b) and  $100 \times 100 \text{ nm}^2$ , 1.0 V, 0.7 nA (c); LEED: 64 eV)

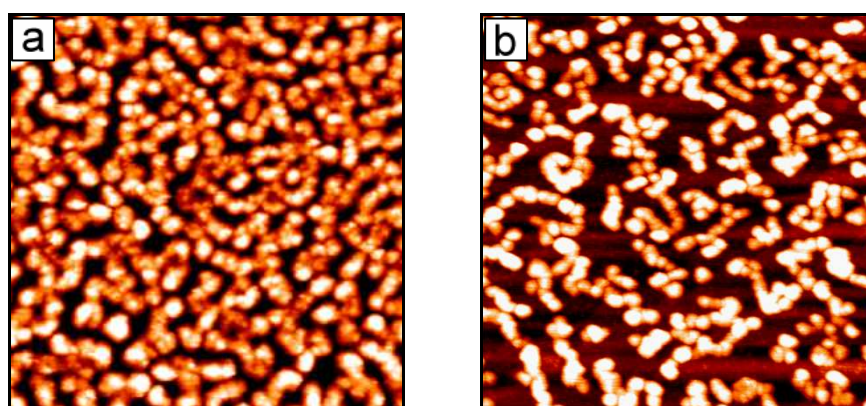


**Fig. 4.24** STM image of FeO(111) film after 50 mbar NO + 10 mbar CO reaction at 450 K for 10 min (a) compared with STM image of FeO(111) film after 20 mbar O<sub>2</sub> + 40 mbar CO at 450 K for 120 min (b) (STM:  $100 \times 100 \text{ nm}^2$ , 2.0 V, 0.7 nA (a) and  $200 \times 200 \text{ nm}^2$ , 0.7 V, 0.4 nA (b))

DFT analysis was performed in order to rationalize the difference between  $\text{CO} + \text{O}_2$  and  $\text{CO} + \text{NO}$  reactions. In both cases the O-rich phase should be formed in a similar way, but in case of NO it is expected to be accompanied by  $\text{N}_2$  (or other N-containing species) desorption.  $\text{CO}_2$  formation and desorption should also proceed similarly. The difference should be the oxygen vacancy replenishment. As mentioned, in case of  $\text{O}_2$  the vacancy is filled with gas phase oxygen which is transformed into a superoxo state  $\text{O}^{2-}$ . The “dangling” O atom reacts with CO from the gas phase forming  $\text{CO}_2$  and thus regenerates the O-rich film. In case of NO the NO molecule is expected to bind to the vacancy similarly to  $\text{O}_2$  (preferentially in the N-down geometry which is by  $\sim 0.6$  eV more favorable than the N-up) (Fig. 4.25). The “dangling” O atom cannot react with CO from the gas phase as the reaction should overcome a high ( $> 2$  eV) energy barrier (although the  $\text{CO}_2$  formation remains exothermic by 1.2 eV). The regeneration of the O-rich film through the “exchange reaction” of NO molecule from the gas phase with the NO in the vacancy resulting in the formation of  $\text{N}_2\text{O}$  and O in the vacancy is energetically favorable (the gain is  $\sim 2.5$  eV), however, it involves an equally high energy barrier and thus seems improbable. Therefore, the adsorption of NO on the vacancy kinetically blocks the further  $\text{CO}_2$  production and O-rich film regeneration.

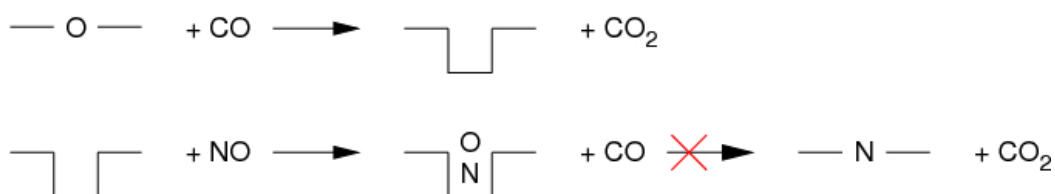


**Fig. 4.25** Schematic representation of the reaction pathways for CO interaction with O-rich film (top) and NO interaction with oxygen vacancy in the O-rich film (bottom)

#### 4.3.6 Encapsulated Pt / $\text{Fe}_3\text{O}_4(111)$ in CO oxidation reaction

It is generally accepted that the encapsulation of metal particles suppresses their catalytic activity (for details please refer to Chapter 1.2). However, due to limited thickness of the encapsulating layers, they may exhibit properties similar to the extended ultrathin oxide films. In Chapter 3 we showed that upon high temperature annealing in UHV Pt

particles supported on Fe<sub>3</sub>O<sub>4</sub>(111) are being encapsulated by an FeO(111) overlayer. These encapsulated particles could be treated as nanometer-sized FeO(111) islands on Pt(111) and act as suitable models for catalytic studies. Due to structural similarities between the encapsulating FeO(111) layers on top of Pt particles and extended FeO(111) films on Pt(111) it was interesting to check, if they would also show similarly enhanced activity in high pressure / low temperature CO oxidation reaction. In order to perform a full comparative study the reaction was carried over both encapsulated and non-encapsulated Pt particles and the results were compared with those obtained for Pt(111) single crystal and extended FeO(111) films on Pt(111). Additional blank experiments were also done on pristine Fe<sub>3</sub>O<sub>4</sub>(111) films.

Pt was deposited at RT onto freshly prepared Fe<sub>3</sub>O<sub>4</sub>(111) films. The Pt coverages used were 0.8 ML (which represented the low coverage) and 2.3 ML (high coverage). The particles were primarily annealed at 600 K for 5 min and secondarily at 850 K for 1 min. For 0.8 ML coverage after annealing at 600 K bilayer islands were formed and for 2.3 ML coverage additional 3-dimensional particles appeared (Figs. 4.26(a)-(d)). The reactivity curves for CO + O<sub>2</sub> reaction were recorded after each annealing step. The reaction was performed both in O-rich and O-lean conditions. CO TPD results revealed that annealing from 600 to 850 K resulted in a dramatic reduction of CO adsorption capabilities (by a factor of three for the 0.8 ML coverage and almost to zero in the case of 2.3 ML coverage; not shown), which indicated encapsulation of Pt by ultrathin FeO(111) layer (see Chapter 3). Therefore, the particles annealed at 850 K could be treated as encapsulated, while those annealed at 600 K as non-encapsulated. The pressures used for the CO oxidation reactions were 40 mbar of CO + 20 mbar of O<sub>2</sub> balanced by He to 1 bar for the reaction in O-lean conditions, and 10 mbar CO + 50 mbar O<sub>2</sub> in He balance for the reaction in O-rich conditions. GC experiments were performed by Yingna Sun [57] for different (more widespread) Pt coverages: 1.6 ML (representing the low coverage) and 6.3 ML (representing the high coverage). This was in order to make the difference between the reactivity results for low and high Pt coverages more pronounced. The results, compared with CO<sub>2</sub> production curves obtained for Pt(111), FeO(111) / Pt(111) and Fe<sub>3</sub>O<sub>4</sub>(111), are presented in Fig. 4.27.

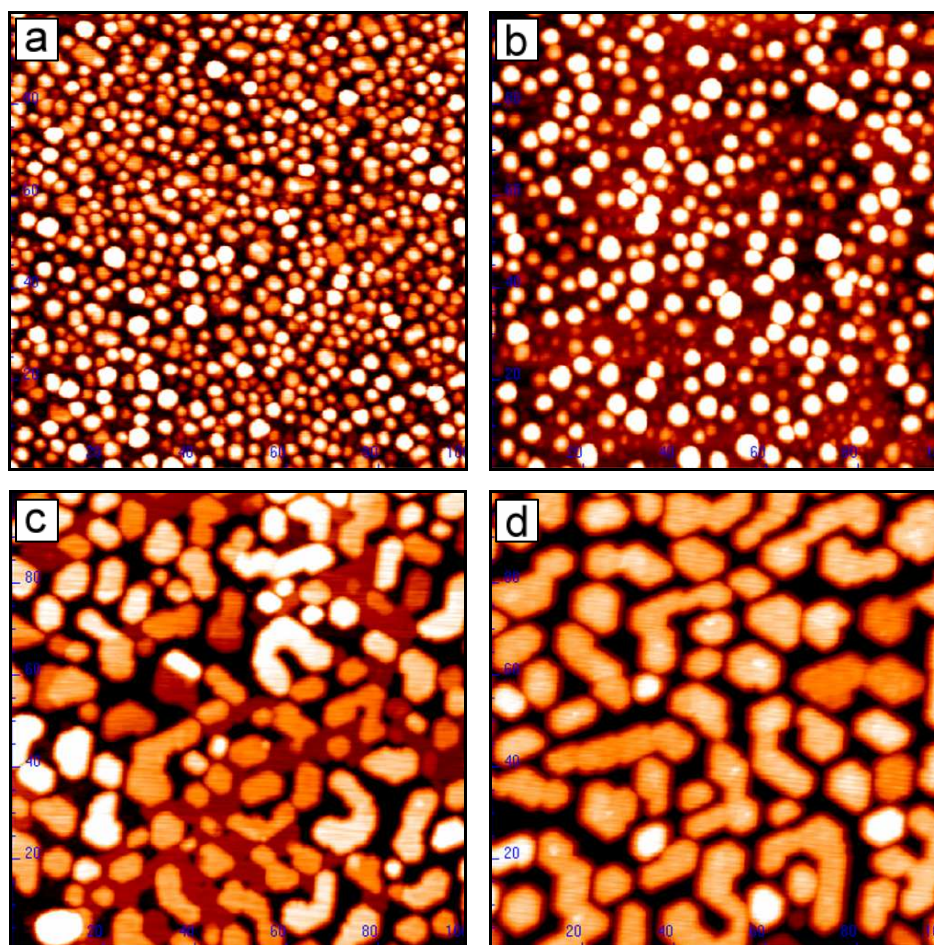


**Fig. 4.26** STM images of Pt / Fe<sub>3</sub>O<sub>4</sub>(111) for the Pt coverages of 0.8 ML (a, c) and 2.3 ML (b, d):  
annealed at 600 K for 5 min (a, b) and annealed at 850 K for 1 min (c, d)  
(STM: 100 x 100 nm<sup>2</sup>, 1.4 V, 1.0 nA (a) and 100 x 100 nm<sup>2</sup>, 1.4 V, 0.7 nA (b-d))

It could be clearly seen that the activity of the catalyst was much higher for high Pt coverage. This suggested that the reaction takes place on Pt particles rather than on particle / oxide interface because the number of interfacial sites was much higher at low Pt coverage. At low coverage the reactivity of the system was very similar to Pt(111) single crystal. It was observed that the average reaction rate increased by a factor of two when increasing the O<sub>2</sub> pressure from 20 to 50 mbar which indicated that O-rich conditions are more favorable for this reaction. Interestingly, at high Pt coverage the encapsulated particles exhibited much higher activity than the non-encapsulated ones, no matter if O-rich or O-lean conditions were used. Pristine Fe<sub>3</sub>O<sub>4</sub>(111) exhibited much lower activity in CO<sub>2</sub> production than FeO(111) films and encapsulated Pt particles but higher than Pt(111). Therefore, the



encapsulating layer seems to play a critical role in the reaction. Promotional effect of metal encapsulation on reactivity on this system is unique, as encapsulation is generally believed to suppress catalytic activity.

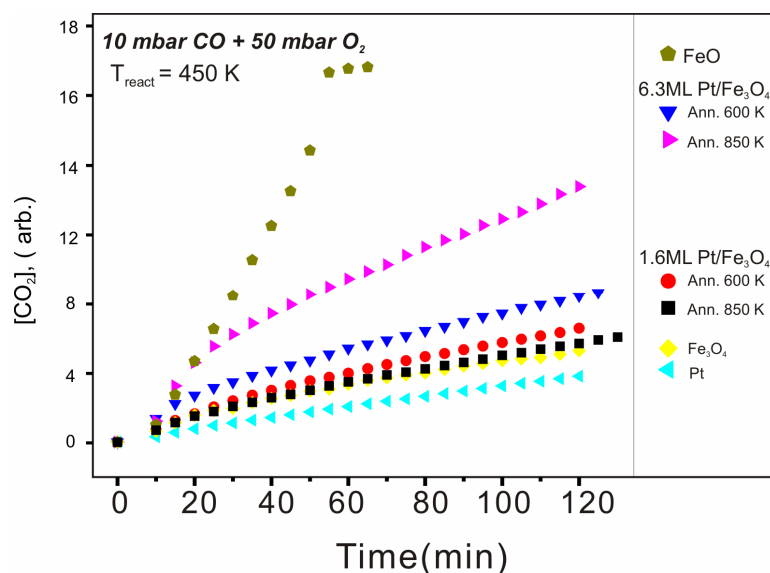


**Fig. 4.27** Kinetics of CO<sub>2</sub> production in CO oxidation reaction on Pt / Fe<sub>3</sub>O<sub>4</sub>(111) for the coverages of 1.6 and 6.3 ML compared with the result for pristine Fe<sub>3</sub>O<sub>4</sub>(111) film / Pt(111) (GC results provided by Yingna Sun, PhD thesis, FU Berlin (2010))

As described in previous sections, the reaction on extended FeO(111) films proceeds via oxygen induced transformation of the bilayer O-Fe film into the catalytically active trilayer O-Fe-O superstructure (Fig. 4.28(f)). To see if similar restructuring is also responsible for high reactivity of encapsulated Pt particles, we exposed a pre-annealed to 850 K 2.3 ML Pt sample to 20 mbar of O<sub>2</sub> at 450 K for 10 min. After oxidation the average size and shape of Pt particles remained unchanged (Figs. 4.28(a) and 4.28(b)). However, a superstructure could be seen on the top facets of particles which previously exhibited the encapsulating FeO(111) layer (Figs. 4.28(b)-(d)). The superstructure was similar to that observed on extended FeO<sub>2</sub> films, but in the case of particles it consisted of hemispherical protrusions (Fig. 4.28(e)) rather than honeycomb-like “patches”. Also the corrugation amplitude was different: ~1 Å in case of encapsulated particles and ~0.5 Å in case of extended FeO(111) film. Nevertheless, similarity between these structures could be clearly seen. The results suggested that most

probably CO oxidation reaction over these systems proceeds in a similar way.

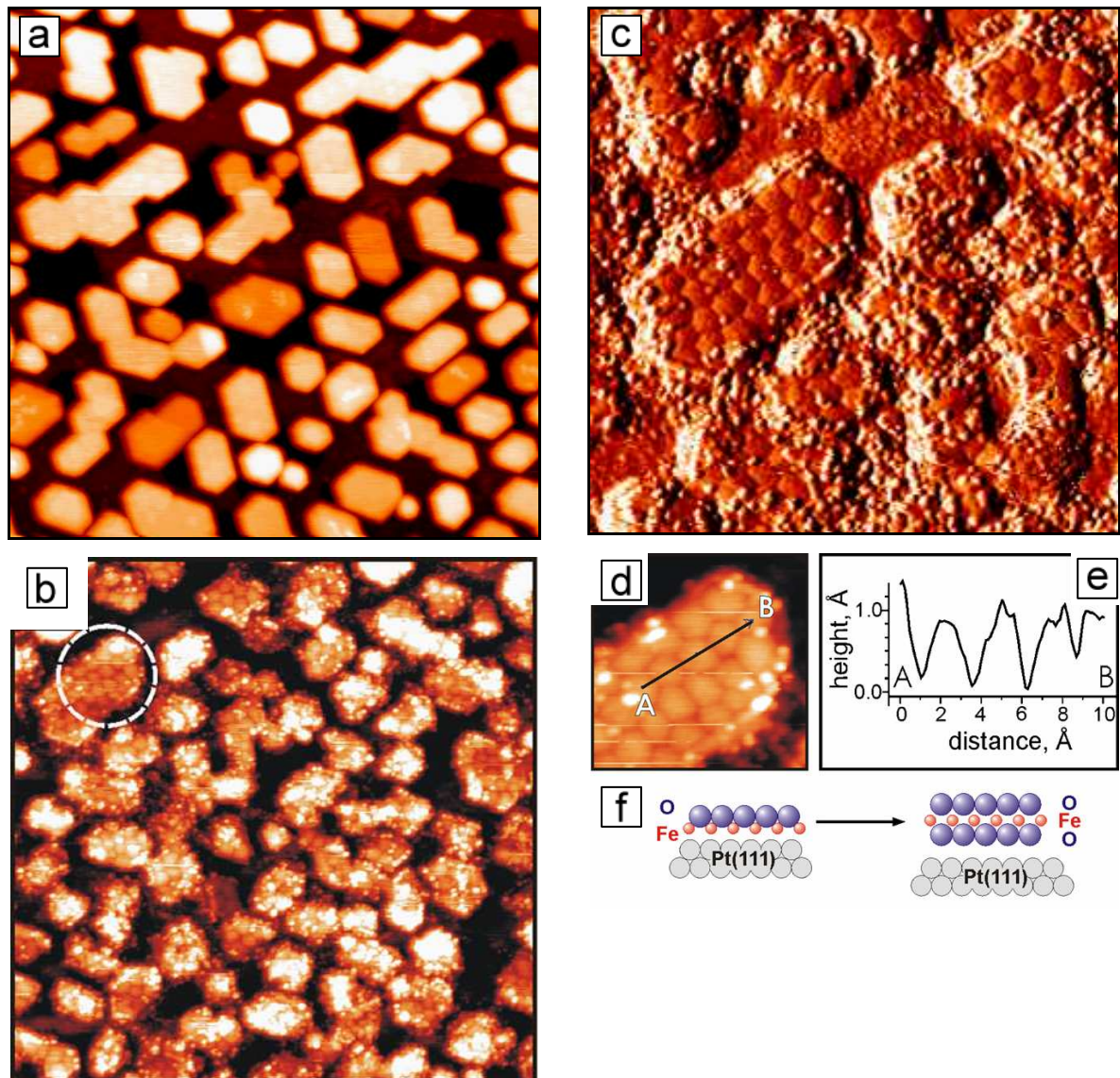


**Fig. 4.28** STM images of 2.3 ML Pt / Fe<sub>3</sub>O<sub>4</sub>(111) annealed in UHV at 850 K for 1 min (a) and subsequently exposed to 20 mbar O<sub>2</sub> at 450 K for 10 min (b-d): (c) and (d) show zoom of the Pt particle marked with circle in (b); profile line along A–B is shown in (e); schematic drawing of the transformation which occurs on the top facets of Pt particles upon O<sub>2</sub> treatment is shown in (f) (STM: 100 x 100 nm<sup>2</sup>, 1.4 V, 0.7 nA (a, b, d, d) and 50 x 50 nm<sup>2</sup>, 1.4 V, 0.7 nA, differentiated contrast (c))

It is important to mention that in case of the reaction carried in O-lean conditions after some time a catalyst deactivation proceeds (not shown). This could be due to insufficient oxygen replenishment and encapsulating layer dewetting followed by arising

competition between O<sub>2</sub> and CO for adsorption on exposed Pt sites. In addition, as mentioned in Chapter 3, CO can dissociate on these sites forming carbon the presence of which could influence the reaction. Under O-rich conditions it is expected that the oxygen replenishment is sufficient, so that no film dewetting occurs.

# Chapter 5

## Au & Pt nanoparticles supported on $\alpha$ -Fe<sub>2</sub>O<sub>3</sub>(0001) films

Part of Prof. Ernst Bauer's Humboldt Research Award 2008 project.

### 5.1 Introduction

Iron oxides have a well-established role in catalysis (see review [10] and references therein). Among them  $\alpha$ -Fe<sub>2</sub>O<sub>3</sub> is the most widely used one in industrial catalytic processes. It is also the least studied iron oxide in research laboratories, especially when thin oxide films are concerned. The oxide can act as a catalyst itself or as a support for catalytically active metal particles. Most of the catalytic studies on  $\alpha$ -Fe<sub>2</sub>O<sub>3</sub> are being performed on single crystals and powders. As an example, CO oxidation reaction on  $\alpha$ -Fe<sub>2</sub>O<sub>3</sub> single crystal and on Au /  $\alpha$ -Fe<sub>2</sub>O<sub>3</sub> was addressed both experimentally and theoretically [127-131]. Preparation of ordered atomically-flat hematite surfaces is very challenging, as the procedure requires high pressures of oxygen and high temperatures [10] or, alternatively, the use of oxygen plasma [132]. There are two known surface terminations of  $\alpha$ -Fe<sub>2</sub>O<sub>3</sub>(0001): the "biphase" and the (1x1) [10]. The structure of these terminations is still under scientific debate [10, 126, 133-138]. In order to get detailed understanding on the catalytic properties of  $\alpha$ -Fe<sub>2</sub>O<sub>3</sub>, a systematic approach is required: First, the structure of  $\alpha$ -Fe<sub>2</sub>O<sub>3</sub>(0001) surface terminations has to be finally solved. Next, the mechanisms of catalytic reactions on the oxide's surface need to be studied and linked to the industrial reaction conditions. Most importantly, the role of feedstock impurities, such as H<sub>2</sub>O, which are present during industrial catalytic processes, has to be investigated. It is known from the literature that H<sub>2</sub>O can interact with the surface of Fe<sub>3</sub>O<sub>4</sub>(111) (see [139] and references therein). As far as Fe<sub>2</sub>O<sub>3</sub> is concerned, to date mainly the H<sub>2</sub>O interaction with the regular  $\alpha$ -Fe<sub>2</sub>O<sub>3</sub> single crystal surfaces was studied [140-142]. Finally, the structure, stability and role of supported noble metal particles on different oxide's surface terminations have to be addressed.

Most of our studies on iron oxides were done on FeO(111) and Fe<sub>3</sub>O<sub>4</sub>(111) films grown on Pt(111). However, it is the  $\alpha$ -Fe<sub>2</sub>O<sub>3</sub> which is considered as catalytically relevant

material. That is why we decided to study  $\alpha$ -Fe<sub>2</sub>O<sub>3</sub>(0001) films on Pt(111). We concentrated on the development of a reproducible preparation procedure of differently terminated  $\alpha$ -Fe<sub>2</sub>O<sub>3</sub>(0001) surfaces. After solving the preparation issue, we performed a combined STM / LEED study on the surface structure of  $\alpha$ -Fe<sub>2</sub>O<sub>3</sub>(0001)-“biphase”. The structure of the “biphase” is widely discussed in the literature – the superstructure which is observed on top of the oxide has a long-range periodicity, similarly to FeO(111) (Moiré pattern), and could be a potentially interesting support for the growth of metal particles. Next, we addressed the nucleation, growth and thermal stability of Au & Pt nanoparticles supported on different oxide’s terminations. Au particles were grown on the “biphase”-terminated  $\alpha$ -Fe<sub>2</sub>O<sub>3</sub>(0001) and Pt particles were grown on the (1x1)-terminated films. Oxide-supported gold catalysts are known to be very active in many important catalytic reactions (see [143] as well as review [144] and references therein). We would also like to shed more light on the role of water in catalysis by gold. That is why we performed additional experiments by exposing the samples to high pressures of H<sub>2</sub>O. We also did preliminary studies on the thermal stability of Pt particles supported on  $\alpha$ -Fe<sub>2</sub>O<sub>3</sub>(0001)-(1x1) films in order to compare the results with data obtained for Pt / Fe<sub>3</sub>O<sub>4</sub>(111).

## 5.2 Samples preparation

The details of preparation of differently terminated  $\alpha$ -Fe<sub>2</sub>O<sub>3</sub>(0001) films on Pt(111) single crystal were described in the literature [10]. However, we encountered serious problems while reproducing these recipes on our experimental setup. Due to this we focused on the development of a new preparation procedures starting from a completely different approach.

### *“Biphase”-terminated $\alpha$ -Fe<sub>2</sub>O<sub>3</sub>(0001)*

Pt(111) single crystal was cleaned as described in the previous chapters. In order to grow the first (interface) iron oxide layer, 1 ML of Fe was deposited onto Pt(111) and oxidized in  $1 \times 10^{-5}$  mbar O<sub>2</sub> at 1000 K for 2 min. Next, four cycles of 8 ML Fe deposition and high temperature oxidation were performed. In the first cycle the oxidation was performed

---

in  $1 \times 10^{-5}$  mbar O<sub>2</sub> at 880 K for 5 min, in the second cycle  $1 \times 10^{-5}$  mbar O<sub>2</sub> at 1000 K for 5 min, in the third in  $5 \times 10^{-5}$  mbar O<sub>2</sub> at 1000 K for 5 min and in the final (fourth) cycle in  $5 \times 10^{-5}$  mbar O<sub>2</sub> at 1100 K for 10 min. After each oxidation the samples were cooled down in O<sub>2</sub> to  $T < 500$  K, except the final oxidation when the O<sub>2</sub> was pumped at  $T = \sim 1100$  K and the samples were cooled down instantly. In this way few nanometers thick “biphase”-terminated  $\alpha$ -Fe<sub>2</sub>O<sub>3</sub>(0001) films were grown. Prior to experiments the films were additionally flashed to 1000 K in UHV to desorb any molecules that could adsorb on the surface from the background pressure of residual gases. High heating rate ( $> 5$  K/s) was used in order to avoid the loss of surface oxygen. The quality of the films was checked with LEED, AES and STM.

#### *(1x1)-terminated $\alpha$ -Fe<sub>2</sub>O<sub>3</sub>(0001)*

The starting point for the preparation was the “biphase”-terminated  $\alpha$ -Fe<sub>2</sub>O<sub>3</sub>(0001) film. The samples were transported to the HP cell and oxidized in  $1 \times 10^{-1}$  mbar O<sub>2</sub> at 1000 K for 10 min. It was observed that the oxygen pressure is decreasing in the course of oxidation. For that reason during some preparations the oxygen was refilled from time to time, while other preparations were performed in oxygen flow at the same pressure. After the oxidation the samples were cooled down in O<sub>2</sub> to  $T < 400$  K and then the HP cell was pumped to  $1 \times 10^{-6}$  mbar (or the other way round). The influence of different preparation procedures on the film’s quality was investigated. Best films were obtained when the oxidation was carried without refilling the oxygen in the HP cell.

#### *Au & Pt nanoparticles*

Au and Pt were deposited at RT. The particles were annealed to different temperatures, as described in the experimental section (Chapter 5.3). The deposition rates were calibrated using STM images and WSxM processing software. For calibration purposes Au was deposited onto FeO(111) and Fe<sub>3</sub>O<sub>4</sub>(111) films grown on Pt(111) and Pt was deposited onto a clean Pt(111) single crystal.

H<sub>2</sub>O

Selected samples were transported to the HP cell and exposed to millibar (mbar) pressures of H<sub>2</sub>O at RT. Water was cleaned by freezing the flask from the outside using liquid nitrogen vapor and pumping the remaining gas. The pressure during the experiments was monitored using Baratron® gauges.

## 5.3 Results & Discussion

### 5.3.1 Au / $\alpha$ -Fe<sub>2</sub>O<sub>3</sub>-“biphase”

First we addressed the surface termination of the “biphase”. Different models were proposed in the literature, such as the coexistence of FeO(111) and  $\alpha$ -Fe<sub>2</sub>O<sub>3</sub>(0001) islands on top of  $\alpha$ -Fe<sub>2</sub>O<sub>3</sub> (Condon et al. [135]) or a thin misfit Fe<sub>3</sub>O<sub>4</sub> overlayer on top of  $\alpha$ -Fe<sub>2</sub>O<sub>3</sub> (Lanier et al. [137]). The STM images presented in Fig. 5.1(a) exhibit a typical “biphase” superstructure which consists of hexagonally shaped depression-like regions (darker) surrounded by six hexagonal hill-like regions (brighter). The superstructure is very regular: it has a long-range periodicity of  $\sim 50$  Å, a corrugation amplitude of  $\sim 0.5$  Å and a step height of  $\sim 2.5$  Å (the uncertainty is related to STM calibration). It is not clear if the hill / depression arrangement is due to a coexistence of different oxide phases or a Moiré type superstructure where the hills / depressed areas are related to electronic effects seen in STM. Unfortunately, it was not possible to resolve both regions with atomic resolution on the same STM image, but we were able to resolve them on separate images. The atomic structure of both regions exhibited hexagonal arrangement with periodicity of  $\sim 7.5$  Å within the inner (depressed) regions (Fig. 5.1(b)) and  $\sim 6.5$  Å within the outer (hill) regions (Fig. 5.1(c)). However, it is important to mention that the measured periodicities could slightly depend on the STM probe quality and the corresponding image distortion, as well as the STM calibration (unless measured on the same STM image which was not possible in our case). In reality the periodicities on both regions can be more / less similar (or even identical). According to our results the inner regions consist of  $\sim 18$ -20 atoms. It was observed that the orientation of the superstructure on different terraces was, in some cases,

---

rotated with respect to the other by  $\sim 12^\circ$ .

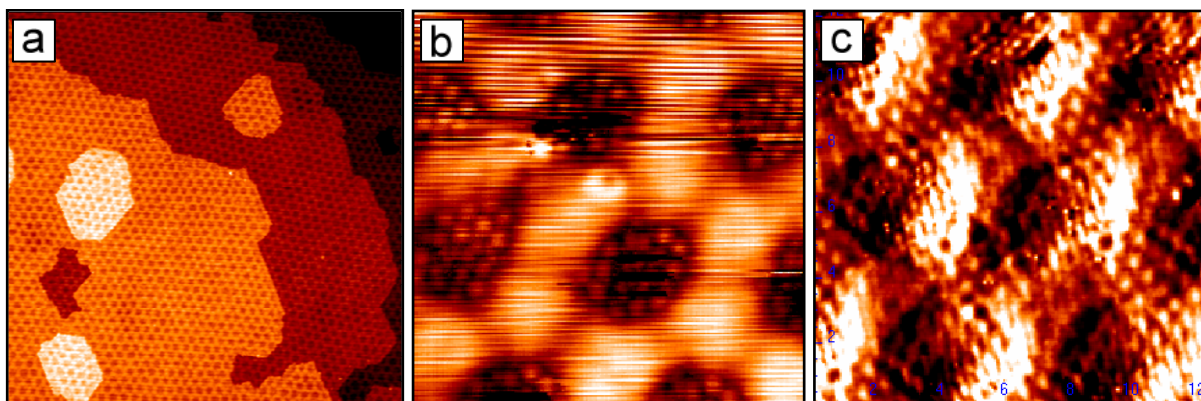


**Fig. 5.1** STM images of  $\alpha$ -Fe<sub>2</sub>O<sub>3</sub>-“biphase”: large scale image showing terraces of hexagonal superstructure (a) and atomic resolution images showing periodicities of  $\sim 7.5$  Å (b) and  $\sim 6.5$  Å (c) (STM:  $200 \times 200$  nm<sup>2</sup>, 1.4 V, 0.7 nA (a);  $12 \times 12$  nm<sup>2</sup>, 1.4 V, 0.7 nA (b) and  $12 \times 12$  nm<sup>2</sup>, 1.4 V, 0.7 nA, differentiated contrast (c))

STM images of freshly prepared “biphase” films revealed that the surface is very “clean”, i.e. it does not seem to attract adsorbates from the background pressure of residual gases. The situation did not change even after longer period of time (few days). This would suggest that the structure is inert to molecules such as CO and H<sub>2</sub>O, at least at very low pressures. All this makes it somehow similar to FeO(111) which could suggest that the “biphase” is oxygen- rather than iron-terminated. For comparison, unreconstructed Fe<sub>3</sub>O<sub>4</sub>(111) and  $\alpha$ -Fe<sub>2</sub>O<sub>3</sub>(0001)-(1x1) surfaces, which are believed to be iron-terminated, show high adsorption affinity to the background pressure molecules and become very “dirty” after few days in the UHV chamber. The LEED pattern of the “biphase” is presented in Fig. 5.2(a). After long-time annealing of the film at high temperatures ( $> 900$  K) the FeO(111)-like spots started to appear on top of the “biphase” pattern (as shown in Fig. 5.2(b)). This could be due to partial film dewetting. All these suggested that both “biphase” models: the coexistence of FeO(111) and  $\alpha$ -Fe<sub>2</sub>O<sub>3</sub>(0001) phases, as well as a misfit overlayer of Fe<sub>3</sub>O<sub>4</sub>, are rather unlikely.



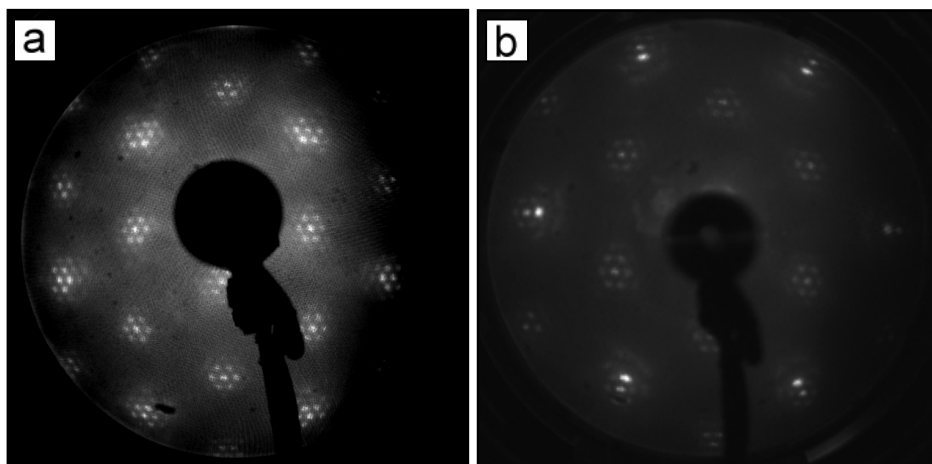


**Fig. 5.2** LEED patterns of  $\alpha$ -Fe<sub>2</sub>O<sub>3</sub>-“biphase” as prepared (a) and after long-time annealing at high temperatures (> 900 K) (b) (LEED: 64 eV)

On the basis of the long-range and atomic periodicities seen in STM, as well as the distances between the LEED spots, we tried to determine other possible surface terminations which would give rise to similar “biphase” structures. Optimization led us to a very simple model where the film would be oxygen-terminated but the topmost oxygen layer would be rotated with respect to the rest of the film by a small angle. This model would be in agreement with film inertness. We did simple simulations by drawing two hexagonal atomic lattices and placing one on top of the other in different ways: in one case the lattices had different periodicities with a ratio of 1:1.067, in order to simulate the model proposed by Lanier et al. (which is the most recent one described in the literature), and in the second case the periodicities ratio was 1:1, but the lattices were rotated with respect to each other by  $3.75^\circ$  (a value which fitted our calculations quite well), thus simulating our speculative model. We also performed FFT of these structures. The results are summarized in Fig. 5.3. It can be clearly seen that both models gave almost identical long range periodicities: 43.6 Å in case of Lanier model and  $42 \pm 5$  Å in case of our model, as well as similar FFT images. In both cases the superlattice cell would be rotated by  $30^\circ$  relative to the  $\alpha$ -Fe<sub>2</sub>O<sub>3</sub>-(1x1). Of course, our model is just speculative and additional experiments, as well as theoretical DFT calculations, are absolutely necessary to prove or disprove it.

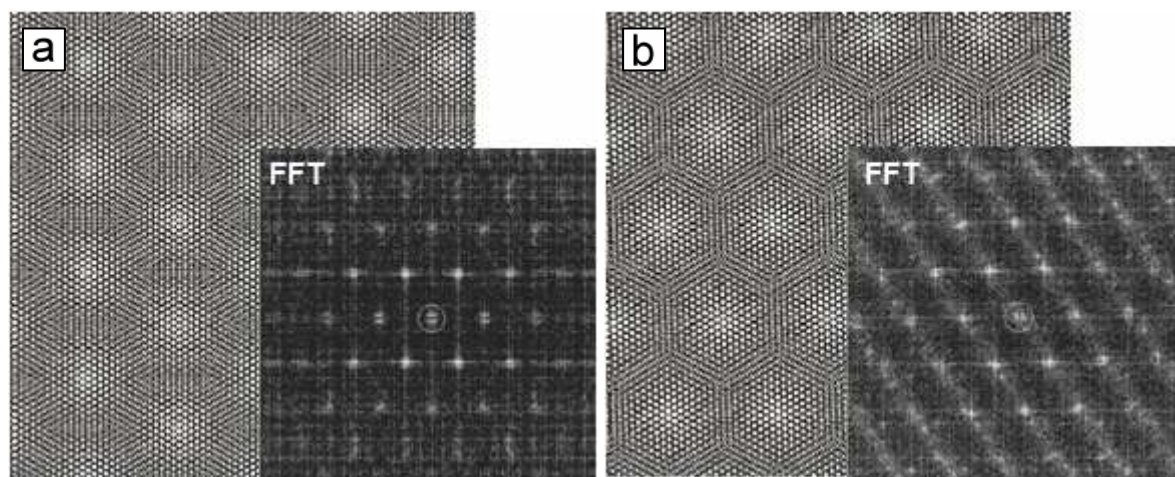


**Fig. 5.3**  $\alpha$ -Fe<sub>2</sub>O<sub>3</sub>-“biphase” superstructure models and corresponding FFT images: lattices with periodicity ratio of 1:1.067 (a) and lattices with periodicity ratio 1:1 rotated by 3.75° with respect to each other (b)

Next, Au was deposited at low coverage corresponding to  $\sim 1/28$  ML. STM results revealed that Au starts to nucleate on the darker (depressed) regions of the “biphase” superstructure (Fig. 5.4). There was no nucleation on the regions between the depressions or on the step edges observed.

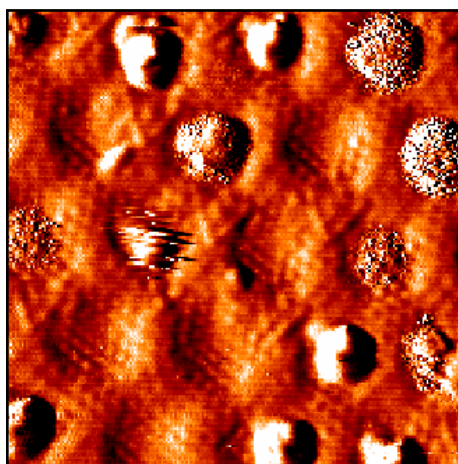


**Fig. 5.4** STM image of  $\sim 1/28$  ML Au /  $\alpha$ -Fe<sub>2</sub>O<sub>3</sub>-“biphase” (STM: 20 x 20 nm<sup>2</sup>, 1.0 V, 0.7 nA, differentiated contrast)

The exact size of the clusters was difficult to determine because of tip deconvolution effects. After deposition of additional  $\sim 1/28$  ML of Au, the size of the particles which were already present on the surface increased and additional particles started to nucleate on the depressed regions which were not previously occupied. At high Au coverage, corresponding to few monolayers (not calibrated), big hemispherical particles were formed (Figs. 5.5(b) and 5.5(c)). All the particles had almost identical shape, a diameter of  $\sim 3$  nm and a height of  $\sim 1$  nm ( $\sim 4$  atomic layers of Au). We were able to resolve on one STM image both the uncovered oxide substrate and the array of Au particles (Fig. 5.5(c)). This was possible because some of the Au particles were accidentally removed by STM tip during scanning.

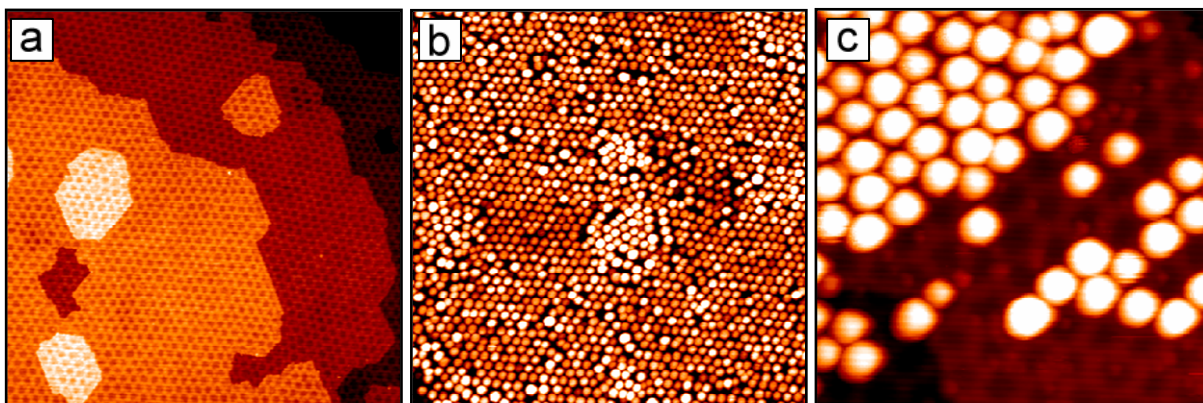


**Fig. 5.5** STM images of  $\alpha$ -Fe<sub>2</sub>O<sub>3</sub>-“biphase” as prepared (a) and after deposition of few monolayers of Au (b, c) (STM: 200 x 200 nm<sup>2</sup>, 1.4 V, 0.7 nA (a); 200 x 200 nm<sup>2</sup>, 2.0 V, 0.7 nA (b) and 50 x 50 nm<sup>2</sup>, 2.0 V, 0.7 nA (c))

The STM results clearly showed that the depressed regions of the “biphase” act as template for particles growth. Annealing to high temperatures, up to 700 K in UHV, did not change the overall morphology of the system which revealed extreme thermal stability of Au particles on this surface. The system could be potentially interesting for applications in catalysis and nanotechnology. Above 700 K particles sintering was observed which resulted in a formation of randomly distributed few-nanometers-high Au clusters (not shown).

We also did preliminary experiments on the effect of hydroxylation of “biphase”  $\alpha$ -Fe<sub>2</sub>O<sub>3</sub>(0001) films. The experiments were performed on the sample which contained very small amount of Au ( $< 0.1$  ML) which has to be kept in mind while interpreting the data. The

sample was transported to the HP cell and exposed to 1 mbar H<sub>2</sub>O at RT for 10 min. Surprisingly, after the exposure the LEED pattern looked very similar, as the one of (1x1)-terminated  $\alpha$ -Fe<sub>2</sub>O<sub>3</sub>(0001) (Fig. 5.6(b)). Unfortunately, the surface turned out to be very rough (“dirty”) which made STM measurements impossible. This could be due to adsorption of water and other molecules which were present in the high pressure cell during water exposure. The AES revealed the presence of carbon (not shown) the origin of which is unknown. Heating the sample to 1000 K recovered the “biphase”-like LEED pattern (Fig. 5.6(c)). Interestingly, the film seemed to be better ordered, as compared to the original “biphase” as higher order satellite spots could be seen.

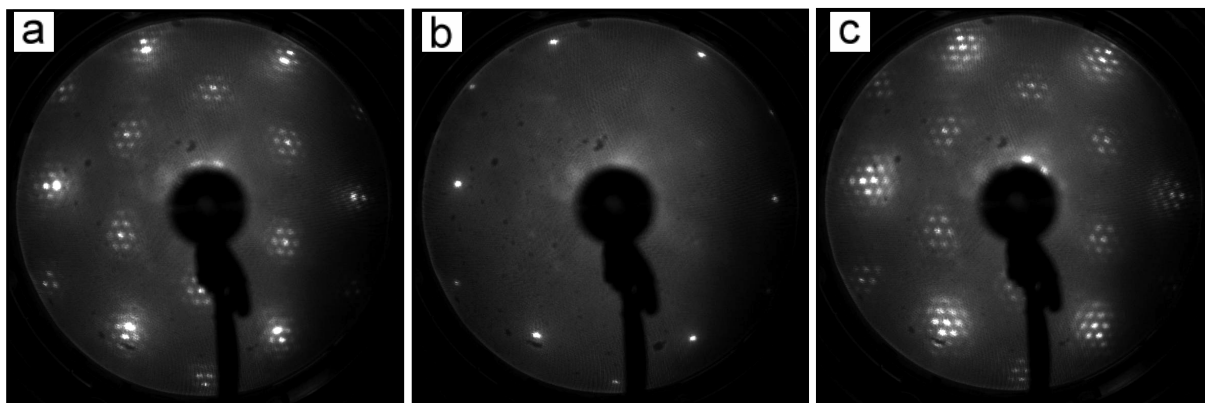


**Fig. 5.6** LEED patterns of  $\alpha$ -Fe<sub>2</sub>O<sub>3</sub>-“biphase” film as prepared (a), exposed to 1 mbar of H<sub>2</sub>O for 10 min (b) and after subsequent heating to 1000 K (c) (LEED: 64 eV)

The STM results also revealed a structure very similar to the original “biphase” (Fig. 5.7). It was possible to resolve the atomic arrangement on the hill-like regions of the superstructure, but not on the depressed areas. The changes in the structure were tentatively explained by partial film reduction due to H<sub>2</sub>O treatment and surface carbon burning during heating to 1000 K. However, it has to be kept in mind that a very small amount of Au was present on the surface which could influence the water-oxide interaction.

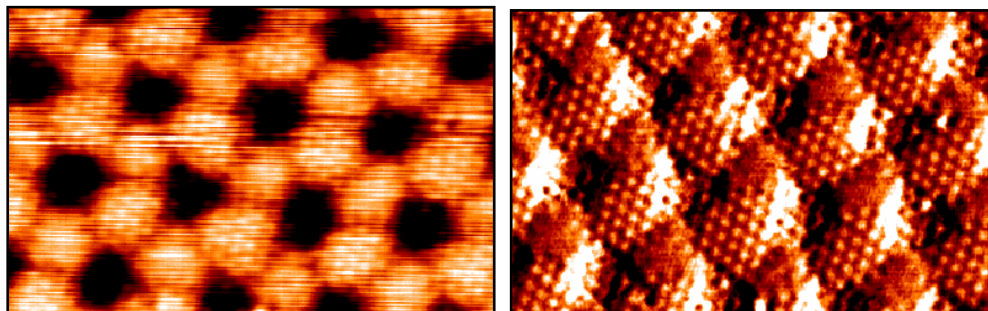


**Fig. 5.7** STM images of  $\alpha$ -Fe<sub>2</sub>O<sub>3</sub>-“biphase” film exposed to 1 mbar of H<sub>2</sub>O for 10 min and subsequently heated to 1000 K: topography (left) & current image (right) (STM: 20 x 12 nm<sup>2</sup>, 1.4 V, 0.7 nA)

### 5.3.2 Pt / $\alpha$ -Fe<sub>2</sub>O<sub>3</sub>-(1x1)

(1x1)-terminated  $\alpha$ -Fe<sub>2</sub>O<sub>3</sub>(0001) films were prepared as described in Chapter 5.2. The quality of the films was checked with LEED, AES and STM. Significant amounts of carbon (272 eV peak), as well as other contamination (peaks  $\sim$ 186 eV and  $\sim$ 220 eV; Mo?) [145], were observed in the AES spectrum (Fig. 5.8). The origin of the contamination was unclear, however, it was always appearing after heating the samples to  $T > 900$  K in the high pressure cell. The stability of the (1x1) surface termination of  $\alpha$ -Fe<sub>2</sub>O<sub>3</sub>(0001) may be related to surface contamination as the contaminants were always observed on the films which showed best quality LEED patterns (see also Fig. 5.6(b)). In order to remove carbon, the samples were flashed to 900 K in UHV using high heating rate (5-10 K/s). The overall structure of the films was not affected by thermal treatment, as judged by LEED (Fig. 5.9(a)). STM images revealed that most probably the carbon was burned with the use of surface oxygen atoms which resulted in holes in the film (Fig. 5.9(b)). Unfortunately, the molybdenum could not be removed which has to be kept in mind while interpreting the data. The atomically resolved STM images obtained between the holes showed hexagonal structure with a periodicity of  $\sim$ 5 Å (5.9(c)), typical for (1x1)-terminated  $\alpha$ -Fe<sub>2</sub>O<sub>3</sub>(0001).

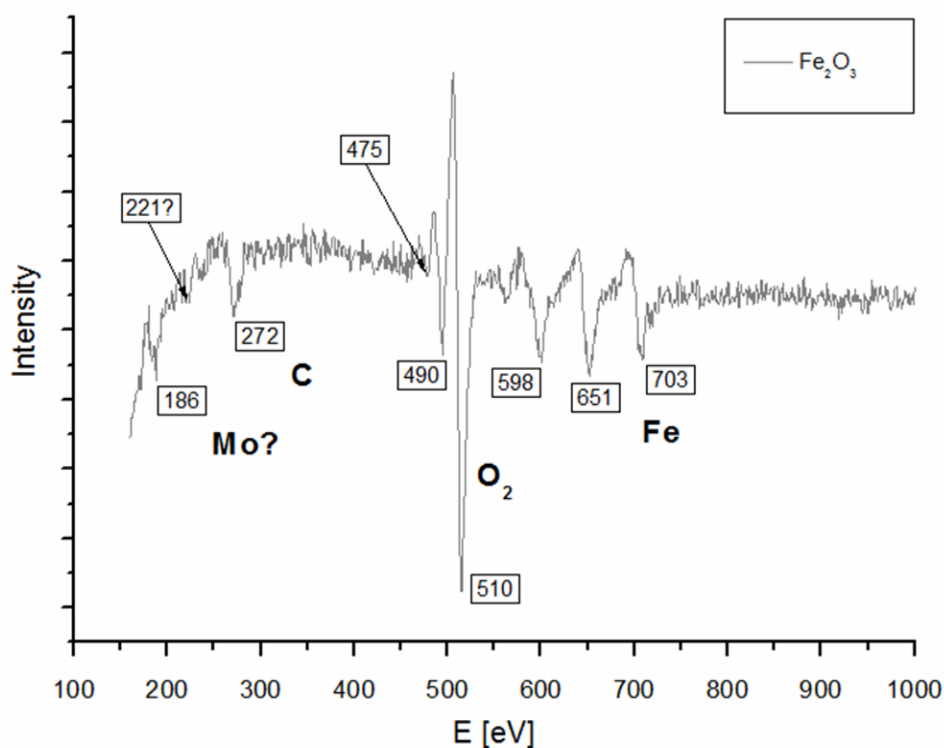


**Fig. 5.8** AES spectrum of  $\alpha$ -Fe<sub>2</sub>O<sub>3</sub>-(1x1) film: carbon and (probably) molybdenum contamination peaks visible

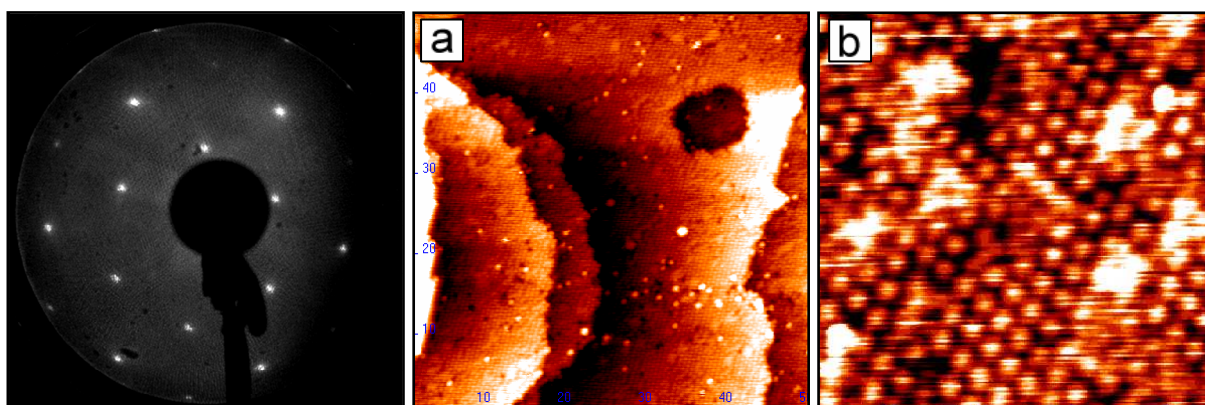


**Fig. 5.9** LEED pattern and STM images of  $\alpha$ -Fe<sub>2</sub>O<sub>3</sub>-(1x1): extended terraces (a) and atomic resolution image showing 5 Å periodicity (b) (LEED: 64 eV; STM: 50 x 50 nm<sup>2</sup>, 1.4 V, 0.7 nA (a) and 8 x 8 nm<sup>2</sup>, 1.4 V, 0.7 nA (b))

Next, 6 Å of Pt were deposited onto the surface. As deposited, Pt formed randomly distributed 3-dimensional particles of different sizes and height ranging from 3-5 ML (Fig.

5.10(a)). Annealing at 600 K for 5 min resulted in particles coalescence and formation of extended Pt islands. The islands were mainly 5 ML in height however, higher particles could also be observed (Fig. 5.10(b)). Annealing at 850 K for 5 min caused the formation of very high 2.5-4 nm particles which were 4-10 nm in diameter (Fig. 5.10(c)). The particles became well-faceted and hexagonally-shaped. Preferential crystallographic orientations for the particles' edges could be seen.

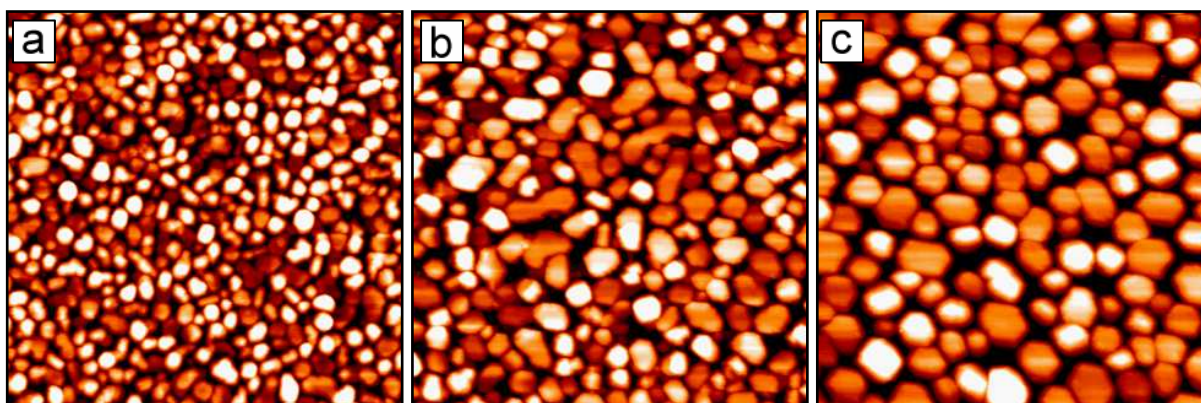


**Fig. 5.10** STM images of 6 Å Pt /  $\alpha$ -Fe<sub>2</sub>O<sub>3</sub>-(1x1): as deposited (a), after annealing at 600 K for 5 min (b) and after annealing at 850 K for 5 min (c) (STM: 100 x 100 nm<sup>2</sup>, 1.4 V, 0.7 nA)

Interestingly, after high temperature annealing in UHV, an atomic structure with 5-6 Å periodicity was observed on top of some particles (Fig. 5.11; marked with red circle). In addition, it was found that the overall particle volume increased by ~20 % on average. This may suggest that the particles were encapsulated by iron oxide. However, CO TPD experiments need to be performed in order to validate this scenario. The observed periodicity, as well as the volume increase, suggested that the encapsulating layer could be more similar to  $\alpha$ -Fe<sub>2</sub>O<sub>3</sub>(0001) or Fe<sub>3</sub>O<sub>4</sub>(111) rather than FeO(111) as in the case of Pt / Fe<sub>3</sub>O<sub>4</sub>(111).

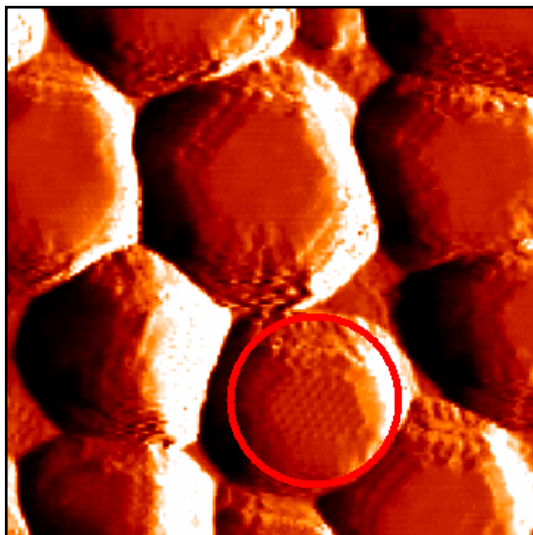


**Fig. 5.11** STM image of Pt /  $\alpha$ -Fe<sub>2</sub>O<sub>3</sub>-(1x1) after high temperature annealing: atomic structure with 5-6 Å periodicity can be seen on top of one of the particles (red circle)  
(STM: 30 x 30 nm<sup>2</sup>, 1.4 V, 0.7 nA, differentiated contrast)



# Chapter 6

## Summary

Iron oxide thin films have been shown as suitable systems for modeling iron oxide based catalysts. Here, we studied FeO(111), Fe<sub>3</sub>O<sub>4</sub>(111), “biphase”- and (1x1)-terminated  $\alpha$ -Fe<sub>2</sub>O<sub>3</sub>(0001) films grown on Pt(111). Morphology of the films, as well as nucleation, growth and thermal stability of noble metal particles, namely Pt & Au, supported on these films were investigated using primarily STM in combination with LEED, AES and TPD. Structural transformations which occur under various temperature / pressure treatments were also addressed. The studies were aimed to gain deeper understanding of structure-reactivity relationships for iron oxide based systems in low temperature CO oxidation reaction in the mbar pressure range. Experimental results were supported by theoretical DFT calculations (provided by Giordano, Goniakowski and Pacchioni).

### **Pt / Fe<sub>3</sub>O<sub>4</sub>(111)**

We studied nucleation, growth and thermal stability of Pt particles supported on Fe<sub>3</sub>O<sub>4</sub>(111) films. Platinum nucleates randomly on the regular terrace sites of Fe<sub>3</sub>O<sub>4</sub>(111) forming monolayer islands which coalesce with increasing coverage. Annealing in UHV resulted in particles sintering and formation of well-faceted 2D islands and 3D particles, depending on the Pt coverage. 2-dimensional structures exhibited lower CO adsorption uptake which is tentatively assigned to the effect of platinum lattice expansion at the interface with the oxide substrate. Annealing at T > 800 K in UHV resulted in encapsulation of Pt by iron oxide overlayer as a result of Strong Metal-Support Interaction (SMSI). Atomic resolution STM images revealed that the encapsulating layer is a monolayer FeO(111) film in nature. The results indicated that the encapsulation most likely begins at the particle edges. The effects were explained by high adhesion energy between platinum and iron oxide.

**FeO(111) / Pt(111)**

It was found that the FeO(111) films on Pt(111) are active in the low temperature CO oxidation reaction in the mbar pressure range. We showed that the reaction includes transformation of bilayer O-Fe film into trilayer O-Fe-O structure. The transformation results in the formation of close-packed FeO<sub>2</sub> islands rather than continuous film, thus leading to an FeO<sub>1.8</sub> stoichiometry of the film, on average. The FeO<sub>2</sub> islands showed a ( $\sqrt{3}\times\sqrt{3}$ )R30° structure with respect to original FeO(111), which was explained by structural relaxation of the Fe sublattice. In addition, the Moiré lattice expansion was observed. STM results provided direct evidence that the CO oxidation reaction on FeO(111) films proceeds via the Mars-van Krevelen type mechanism. The reaction can be divided into three steps: (i) transformation of bilayer Fe-O film into trilayer O-Fe-O film structure, (ii) reaction of CO with the topmost oxygen atoms and desorption of CO<sub>2</sub> and (iii) replenishment of oxygen vacancies by the gas phase O<sub>2</sub>. In the O-lean conditions film dewetting was observed that slowed down the CO<sub>2</sub> production. Replacing O<sub>2</sub> with NO as an oxidative agent resulted in a formation of virtually identical oxygen-rich films. However, these films did not show sustained reactivity in the CO + NO reaction, indicating that oxygen replenishment is the rate-limiting step in this reaction. The STM study of the encapsulated Pt / Fe<sub>3</sub>O<sub>4</sub> system in the low temperature CO oxidation reaction revealed, basically, the same scenario that explains the activity enhancement observed for encapsulated Pt particles as compared to clean Pt particles.

**Au & Pt /  $\alpha$ -Fe<sub>2</sub>O<sub>3</sub>(0001)**

We developed a preparation procedure for “biphase”- and (1x1)-terminated  $\alpha$ -Fe<sub>2</sub>O<sub>3</sub>(0001) films on Pt(111). The procedure includes oxidation steps at high temperatures between 1000 and 1100 K in high pressures of oxygen, i.e.  $5 \times 10^{-5}$  mbar in case of the “biphase” and  $1 \times 10^{-1}$  mbar in case of the (1x1). The surface termination of the “biphase” was investigated using LEED and STM. A model was proposed where the surface is terminated with an O layer that is rotated by a small angle. The “biphase” surface was shown as a good template for the growth of monodispersed Au nanoparticles with a narrow

---

particles size distribution. The particles were found to nucleate only on specific regions within the “biphase” structure. In addition, the particles were shown to be resistant towards sintering up to 700 K in UHV. In addition, the stability of the “biphase” surface in high pressures of H<sub>2</sub>O was investigated. We also studied Pt /  $\alpha$ -Fe<sub>2</sub>O<sub>3</sub>(0001)-(1x1). Pt was deposited at high coverage which resulted in a formation of nm high 3D particles. After high temperature annealing the particles sintered and became well shaped. An atomic structure was observed on top of some of the particles which may suggest that they underwent encapsulation by the substrate oxide. Additional studies are necessary to get more detailed information on this system.

## Literature

- [1] J. A. Dumesic, G. W. Huber, and M. Boudart in *Handbook of Heterogeneous Catalysis* (1997) by G. Ertl, H. Knözinger, and J. Weitkamp, Eds. VCH, Weinheim, Germany, p. 1.
- [2] *Catalysis Looks to the Future* (1992), National Academy Press, Washington, D.C., USA, p. 12.
- [3] J. J. Berzelius, *Edinburgh New Philosophical Journal* 21 (1836), p. 223-228.
- [4] F. Haber, *The synthesis of ammonia from its elements* (1918), Nobel Lecture.
- [5] G. Ertl, *Reactions at Surfaces: From Atoms to Complexity* (2007), Nobel Lecture.
- [6] B. H. Davis in *Handbook of Heterogeneous Catalysis* (1997) by G. Ertl, H. Knözinger, and J. Weitkamp, Eds. VCH, Weinheim, Germany, p. 16-37.
- [7] G. A. Somorjai, *Introduction to Surface Chemistry and Catalysis* (1994), John Wiley & Sons, Inc., New York, USA.
- [8] C. C. Chusuei, X. Lai, K. Luo, and D. W. Goodman, *Topics in Catalysis* 14 (2001), p. 71-83.
- [9] J. Libuda, S. Schaueremann, M. Laurin, T. Schalow, and H.-J. Freund, *Monatshefte für Chemie* 136 (2005), p. 59-75.
- [10] W. Weiss and W. Ranke, *Progress in Surface Science* 70 (2002), p. 1-151.
- [11] R. M. Jaeger, H. Kuhlenbeck, H.-J. Freund, M. Wuttig, W. Hoffmann, R. Franchy, and H. Ibach, *Surface Science* 259 (1991), p. 235-252.
- [12] M. C. Wu, J. S. Corneille, C. A. Estrada, J. W. He, and D. W. Goodman, *Chemical Physics Letters* 182 (1991), p. 472-478.
- [13] T. Schroeder, M. Adelt, B. Richter, M. Naschitzki, M. Bäumer, and H.-J. Freund, *Surface Review and Letters* 7 (2000), p. 7-14.
- [14] W. Ostwald, *Lehrbuch der Allgemeinen Chemie* (1896), vol. 2, part 1, Leipzig, Germany.
- [15] M. Cherkaoui and L. Capolungo, *Atomistic and Continuum Modeling of Nanocrystalline Materials* (2009), Springer GmbH, Germany, p. 294-295.
- [16] E. Bauer, *Zeitschrift für Kristallographie* 110 (1958), p. 372-394.
- [17] Q. Fu and T. Wagner, *Surface Science Reports* 62 (2007), p. 431-498.
- [18] G. Wulff, *Zeitschrift für Kristallographie und Mineralogie* 34 (1901), p. 449-530.
- [19] K. H. Hansen, T. Worren, S. Stempel, E. Lægsgaard, M. Bäumer, H.-J. Freund, F.

- Besenbacher, and I. Stensgaard, *Physical Review Letters* 83 (1999), p. 4120-4123.
- [20] S. J. Tauster, S. C. Fung, and R. L. Garten, *Journal of the American Chemical Society* 100 (1978), p. 170-174.
- [21] J.-M. Pan and T. E. Madey, *Catalysis Letters* 20 (1993), p. 269-274.
- [22] F. Pesty, H.-P. Steinrück, and T. E. Madey, *Surface Science* 33 (1995), p. 9-83.
- [23] F. Cosandey, L. Zhang, and T. E. Madey, *Surface Science* 474 (2001), p. 1-13.
- [24] O. Dulub, W. Hebenstreit, and Ulrike Diebold, *Physical Review Letters* 84 (2000), p. 3646-3649.
- [25] D. R. Jennison, O. Dulub, W. Hebenstreit, and U. Diebold, *Surface Science Letters* 492 (2001), p. L677-L687.
- [26] T. Suzuki and R. Souda, *Surface Science* 448 (2000), p. 33-39.
- [27] D. R. Mullins and K. Z. Zhang, *Surface Science* 513 (2002), p. 163-173.
- [28] S. D. Senanayake, J. Zhou, A. P. Baddorf, and D. R. Mullins, *Surface Science* 601 (2007), p. 3215-3223.
- [29] Y. Gao, Y. Liang, and S. A. Chambers, *Surface Science* 365 (1996), p. 638-648.
- [30] Q. Fu, T. Wagner, S. Olliges, and H.-D. Carstanjen, *The Journal of Physical Chemistry B* 109 (2005), p. 944-951.
- [31] H. Knözinger and E. Taglauer in *Handbook of Heterogeneous Catalysis* (1997) by G. Ertl, H. Knözinger, and J. Weitkamp, Eds. VCH, Weinheim, Germany, p. 216-231.
- [32] R. A. Bennett, P. Stone, and M. Bowker, *Catalysis Letters* 59 (1999), p. 99-105.
- [33] M. Bowker, P. Stone, R. A. Bennett, and N. Perkins, *Surface Science* 497 (2002), p. 155-173.
- [34] M. Bowker, P. Stone, P. Morrall, R. Smith, R. Bennett, N. Perkins, R. Kvon, C. Pang, E. Fourre, and M. Hall, *Journal of Catalysis* 234 (2005), p. 172-181.
- [35] M. Bowker and R. A. Bennet in *Model Systems in Catalysis: Single Crystals to Supported Enzyme Mimics* (2010) by R. M. Rioux, Springer Science+Business Media, Berlin, Germany, p. 155-173.
- [36] F. Silly and M. R. Castell, *The Journal of Physical Chemistry B* 109 (2005), p. 12316-12319.
- [37] Z. Majzik, N. Balázs, and A. Berkó, *The Journal of Physical Chemistry C* 115 (2011), p. 9535-9544.
- [38] F. Sedona, G. A. Rizzi, S. Agnoli, F. X. Llabrés i Xamena, A. Papageorgiou, D. Ostermann,

- M. Sambì, P. Finetti, K. Schierbaum, and G. Granozzi, *The Journal of Physical Chemistry B* 109 (2005), p. 24411-24426.
- [39] C. Wu, M. S. J. Marshall, and M. R. Castell, *The Journal of Physical Chemistry C* 115 (2011), p. 8643-8652.
- [40] *Encyclopedia Britannica Online*:  
[www.britannica.com/EBchecked/topic/95021/carbon-monoxide](http://www.britannica.com/EBchecked/topic/95021/carbon-monoxide) (07.2011)
- [41] I. Langmuir, *Transactions of the Faraday Society* 17 (1922), p. 621-654.
- [42] T. Engel and G. Ertl, *Advances in Catalysis* 28 (1979), p. 1-78.
- [43] P. J. Berlowitz, C. H. F. Peden, and D. W. Goodman, *The Journal of Physical Chemistry* 92 (1988), p. 5213-5221.
- [44] J. Wintterlin, S. Völkening, T. V. W. Janssens, T. Zambelli, and G. Ertl, *Science* 278 (1997), p. 1931-1934.
- [45] A. K. Santra and D. W. Goodman, *Electrochimica Acta* 47 (2002), p. 3595-3609.
- [46] J. T. Kummer, *The Journal of Physical Chemistry* 90 (1986), p. 4747-4752.
- [47] G. Blyholder, *The Journal of Physical Chemistry* 68 (1964), p. 2772-2777.
- [48] K. Kochloefl in *Handbook of Heterogeneous Catalysis* (1997) by G. Ertl, H. Knözinger, and J. Weitkamp, Eds. VCH, Weinheim, Germany, p. 2151-2159.
- [49] G. Ketteler, W. Weiss, W. Ranke, and R. Schlögl, *Physical Chemistry Chemical Physics* 3 (2001), p. 1114-1122.
- [50] Y. J. Kim, C. Westphal, R. X. Ynzunza, H. C. Galloway, M. Salmeron, M. A. Van Hove, and C. S. Fadley, *Physical Review B* 55 (1997), p. 13448-13451.
- [51] *Encyclopedia Britannica Online*:  
<http://www.britannica.com/EBchecked/topic/387754/moire-pattern> (07.2011)
- [52] E. D. L. Rienks, N. Nilius, H.-P. Rust, and H.-J. Freund, *Physical Review B* 71 (2005), p. R241404-1-R241404-4.
- [53] C. Noguera, *Journal of Physics: Condensed Matter* 12 (2000), p. R367-R410.
- [54] M. Paul, M. Sing, R. Claessen, D. Schrupp, and V. A. M. Brabers, *Physical Review B* 76 (2007), p. 075412-1-075412-8.
- [55] I. Horcas, R. Fernandez, J. M. Gomez-Rodriguez, J. Colchero, J. Gomez-Herrero, and A. M. Baro, *Review of Scientific Instruments* 78 (2007), p. 013705-1-013705-8.
- [56] <http://gwyddion.net> (07.2011)
- [57] Yingna Sun, *Enhanced Reactivity Of Ultrathin Oxide Films In Oxidation Reactions: Back*
-

- To "Electronic Theory Of Catalysis" (2010), PhD thesis, Freie Universität Berlin.
- [58] G. Binnig, H. Rohrer, Ch. Gerber, and E. Weibel, *Applied Physics Letters* 40 (1981), p. 178-180.
- [59] G. Binnig, H. Rohrer, Ch. Gerber, and E. Weibel, *Physical Review Letters* 49 (1982), p. 57-61.
- [60] G. Binnig and H. Rohrer, *Scanning Tunneling Microscopy - From Birth To Adolescence* (1986), Nobel Lecture, *Angewandte Chemie International Edition in English* 26 (1987), p. 606-614.
- [61] C. J. Chen, *Introduction to Scanning Tunneling Microscopy* (1993), Oxford University Press, New York, USA.
- [62] <http://www.fkf.mpg.de/ga/research/stmtutor/stmtheo.html> (07.2011)
- [63] [http://wapedia.mobi/en/Scanning\\_tunneling\\_microscope](http://wapedia.mobi/en/Scanning_tunneling_microscope) (07.2011)
- [64] E. Meyer, H. Hug, and R. Bennewitz, *Scanning Probe Microscopy: The Lab on a Tip* (2004), Springer-Verlag, Berlin, Germany.
- [65] S. N. Magonov and M.-H. Whangbo, *Surface Analysis with STM and AFM: Experimental and Theoretical Aspects of Image Analysis* (1996), Wiley-VCH, Weinheim, Germany.
- [66] G. Binnig and D. P. E. Smith, *Review of Scientific Instruments* 57 (1986), p. 1688-1689.
- [67] L. de Broglie, *The wave nature of the electron* (1929), Nobel Lecture.
- [68] C. Davisson and L. H. Germer, *Physical Review* 30 (1927), p. 705-740.
- [69] W. L. Bragg, *The diffraction of X-rays by crystals* (1922), Nobel Lecture.
- [70] S. J. Garrett, *Introduction to Surface Analysis* (2001), Lecture Notes, Michigan State University, USA.
- [71] G. Ertl and J. Kueppers, *Low Energy Electrons and Surface Chemistry* (1985), Verlag Chemie, Weinheim, Germany, p. 210.
- [72] L. Meitner, *Zeitschrift für Physik* 9 (1922), p. 131-144.
- [73] Pierre Auger, *Comptes Rendus de l'Académie des sciences* 177 (1923), p. 169-171.
- [74] *Encyclopedia Britannica Online*,  
<http://www.britannica.com/EBchecked/topic/41699/atomic-mass> (07.2011)
- [75] J. K. Lang, *Handbook on Mass Spectrometry: Instrumentation, Data and Analysis, and Applications* (2010), Nova Science Publishers Inc., Hauppauge, USA.
- [76] <http://www.pfeiffer-vacuum.com> (07.2011)
- [77] P. Hoffman, *Lecture Notes on Surface Science* (2005), Lecture Notes, Århus University,

Denmark.

[78] P. A. Redhead, *Vacuum* 12 (1962), p. 203-211.

[79] J. W. Niemantsverdriet, *Spectroscopy in Catalysis* (2007), Wiley-VCH, Weinheim, Germany, p. 29-31.

[80] Z.-H. Qin, M. Lewandowski, Y.-N. Sun, S. Shaikhutdinov, and H.-J. Freund, *The Journal of Physical Chemistry C* 112 (2008), p. 10209-10213.

[81] Z.-H. Qin, M. Lewandowski, Y.-N. Sun, S. Shaikhutdinov, and H.-J. Freund, *Journal of Physics: Condensed Matter* 21 (2009), p. 134019-1-134019-6.

[82] Y.-N. Sun, Z.-H. Qin, M. Lewandowski, S. Shaikhutdinov, and H.-J. Freund, *Surface Science* 603 (2009), p. 3099-3103.

[83] N. Nilius, E. D. L. Rienks, H.-P. Rust, and H.-J. Freund, *Physical Review Letters* 95 (2005), p. 066101-1-066101-4.

[84] S. Shaikhutdinov, R. Meyer, D. Lahav, M. Bäumer, T. Klüner, and H.-J. Freund, *Physical Review Letters* 91 (2003), p. 076102-1-076102-4.

[85] R. Meyer, M. Bäumer, Sh. K. Shaikhutdinov, and H.-J. Freund, *Surface Science* 546 (2003), p. 813-819.

[86] R. Meyer, D. Lahav, T. Schalow, M. Laurin, B. Brandt, S. Schaueremann, S. Guimond, Th. Klüner, H. Kuhlenbeck, J. Libuda, Sh. Shaikhutdinov, and H.-J. Freund, *Surface Science* 586 (2005), p. 174-182.

[87] C. Gatel and E. Snoeck, *Surface Science* 600 (2006), p. 2650-2662.

[88] C. Gatel and E. Snoeck, *Surface Science* 601 (2007), p. 1031-1039.

[89] R. Meyer, Sh. K. Shaikhutdinov, and H.-J. Freund, *Zeitschrift für Physikalische Chemie* 218 (2004), p. 905-914.

[90] T. Schalow, B. Brandt, M. Laurin, S. Schaueremann, S. Guimond, D. E. Starr, H. Kuhlenbeck, S. K. Shaikhutdinov, J. Libuda, and H.-J. Freund, *Angewandte Chemie* 117 (2005), p. 7773-7777 & *Angewandte Chemie International Edition* 44 (2005), p. 7610-7605.

[91] T. Schalow, B. Brandt, D. E. Starr, M. Laurin, S. Schaueremann, S. K. Shaikhutdinov, J. Libuda, and H.-J. Freund, *Catalysis Letters* 107 (2006), p. 189-196.

[92] T. Schalow, B. Brandt, M. Laurin, S. Schaueremann, S. Guimond, H. Kuhlenbeck, J. Libuda, and H.-J. Freund, *Surface Science* 600 (2006), p. 2528-2542.

[93] T. Ma, Q. Fu, H.-Y. Su, H.-Y. Liu, Y. Cui, Z. Wang, R.-T. Mu, W.-X. Li, and X.-H. Bao, *ChemPhysChem* 10 (2009), p. 1013-1016.



- [94] L. Vitos, A. Ruban, H. Skriver, and J. Kollár, *Surface Science* 411 (1998), p. 186-202.
- [95] G. Ertl, M. Neumann, and K. M. Streit, *Surface Science* 64 (1977), p. 393-410.
- [96] R. W. McCabe and L. D. Schmidt, *Surface Science* 66 (1977), p. 101-124.
- [97] M. R. McClellan, J. L. Gland, and F. R. McFesly, *Surface Science* 112 (1981), p. 63-77.
- [98] H. Steininger, S. Lehwald, and H. Ibach, *Surface Science* 123 (1982), p. 264-282.
- [99] C. Lemire, V. E. Henrich, Sh. Shaikhutdinov, and H.-J. Freund, *Surface Science* 572 (2004), p. 103-114.
- [100] N. R. Avery, *Chemical Physics Letters* 96 (1983), p. 371-373.
- [101] J. L. Gland, B. A. Sexton, and G. B. Fisher, *Surface Science* 95 (1980), p. 587-602.
- [102] Sh. K. Shaikhutdinov, M. Ritter, X. G. Wang, H. Over, and W. Weiss, *Physical Review B: Condensed Matter and Material Physics* 60 (1999), p. 11062-11069.
- [103] Y.-X. Yao, Q. Fu, Z. Wang, D.-L. Tan, and X.-H. Bao, *The Journal of Physical Chemistry C* 114 (2010), p. 17069-17079.
- [104] W. Weiss and M. Ritter, *Physical Review B: Condensed Matter and Material Physics* 59 (1999), p. 5201-5213.
- [105] Sh. Shaikhutdinov, M. Ritter, and W. Weiss, *Physical Review B: Condensed Matter and Material Physics* 62 (2000), p. 7535-7541.
- [106] A. Atli, M. Abon, P. Beccat, J. C. Bertolini, and B. Tardy, *Surface Science* 302 (1994), p. 121-125.
- [107] Y.-N. Sun, Z.-H. Qin, M. Lewandowski, S. Kaya, S. Shaikhutdinov, and H.-J. Freund, *Catalysis Letters* 126 (2008), p. 12631-12635.
- [108] Y.-N. Sun, Z.-H. Qin, M. Lewandowski, E. Carrasco, M. Sterrer, S. Shaikhutdinov, and H.-J. Freund, *Journal of Catalysis* 266 (2009), p. 359-368.
- [109] Y.-N. Sun, L. Giordano, J. Goniakowski, M. Lewandowski, Z.-H. Qin, C. Noguera, S. Shaikhutdinov, G. Pacchioni, and H.-J. Freund, *Angewandte Chemie* 122 (2010), p. 4520-4523 & *Angewandte Chemie International Edition* 49 (2010), p. 4418-4421.
- [110] L. Giordano, M. Lewandowski, I. M. N. Groot, Y.-N. Sun, J. Goniakowski, C. Noguera, S. Shaikhutdinov, G. Pacchioni, and H.-J. Freund, *The Journal of Physical Chemistry C* 114 (2010), p. 21504-21509.
- [111] M. Lewandowski, Y.-N. Sun, Z.-H. Qin, S. Shaikhutdinov, and H.-J. Freund, *Applied Catalysis A: General* 391 (2011), p. 407-410.
- [112] Y. Lei, M. Lewandowski, Y.-N. Sun, Y. Fujimori, Y. Martynova, I. M. N. Groot, R. Meyer,

- L. Giordano, G. Pacchioni, J. Goniakowski, C. Noguera, S. Shaikhutdinov, and H.-J. Freund, *ChemCatChem* 3 (2011), p. 671-674.
- [113] M. Lewandowski, I. M. N. Groot, S. Shaikhutdinov, and H.-J. Freund, *Catalysis Today* (2011), accepted.
- [114] M. Sterrer, T. Risse, L. Giordano, M. Heyde, N. Nilius, H.-P. Rust, G. Pacchioni, and H.-J. Freund, *Angewandte Chemie* 119 (2007), p. 8858-8861 & *Angewandte Chemie International Edition* 46 (2007), p. 8703-8706.
- [115] H.-J. Freund, *Surface Science Prospectives* 601 (2007), p. 1438-1442.
- [116] N. Nilius, *Surface Science Reports* 64 (2009), p. 595-659.
- [117] M. Sterrer, T. Risse, U. M. Pozzoni, L. Giordano, M. Heyde, H.-P. Rust, G. Pacchioni, and H.-J. Freund, *Physical Review Letters* 98 (2007), p. 096107-1-096107-4.
- [118] M. Sterrer, T. Risse, M. Heyde, H.-P. Rust, and H.-J. Freund, *Physical Review Letters* 98 (2007), p. 206103-1-206103-4.
- [119] L. Giordano, G. Pacchioni, J. Goniakowski, N. Nilius, E. D. L. Rienks, and H.-J. Freund, *Physical Review Letters* 101 (2008), p. 026102-1-026102-4.
- [120] E. D. L. Rienks, N. Nilius, H.-J. Freund, L. Giordano, G. Pacchioni, and J. Goniakowski, *Physical Review B* 73 (2009), p. 075427-1-075427-6.
- [121] A. Hellman, S. Klacar, H. Grönbeck, *Journal of the American Chemical Society* 131 (2009), p. 16636-16637.
- [122] X. Lin, B. Yang, H.-M. Benia, P. Myrach, M. Yulikov, A. Aumer, M. A. Brown, M. Sterrer, O. Bondarchuk, E. Kieseritzky, J. Rucker, T. Risse, H.-J. Gao, N. Nilius, and H.-J. Freund, *Journal of the American Chemical Society* 132 (2010), p. 7745-7749.
- [123] A. Gonchar, T. Risse, H.-J. Freund, L. Giordano, C. Di Valentin, and G. Pacchioni, *Angewandte Chemie* 123 (2011), p. 2684-2687 & *Angewandte Chemie International Edition* 50 (2011), p. 2635-2638.
- [124] L. Giordano, F. Cinquini, and G. Pacchioni, *Physical Review B* 73 (2005), p. 045414-1-045414-6.
- [125] F. F. Vol'kenshtein, *Russian Chemical Reviews* 35 (1966), p. 537-546.
- [126] C. Lemire, S. Bertarione, A. Zacchina, D. Scarano, A. Chaka, S. Shaikhutdinov, and H.-J. Freund, *Physical Review Letters* 94 (2005), p. 166101-1-166101-4.
- [127] P. Li, D. E. Miser, S. Rabiei, R. T. Yadav, and M. R. Hajaligol, *Applied Catalysis B: Environmental* 43 (2003), p. 151-162.

- [128] A. K. Kandalam, B. Chatterjee, S. N. Khanna, B. K. Rao, P. Jena, and B. V. Reddy, *Surface Science* 601 (2007), p. 4873-4880.
- [129] H. Randall, R. Doepper, and A. Renken, *Industrial & Engineering Chemistry Research* 36 (1997), p. 2996-3001.
- [130] Z. Y. Zhong, J. Highfield, M. Lin, J. Teo, and Y. F. Han, *Langmuir* 24 (2008), p. 8576-8582.
- [131] S. Kudo, T. Maki, M. Yamada, and K. Mae, *Chemical Engineering Science* 65 (2010), p. 214-219.
- [132] A. Barbier, R. Belkhou, P. Ohresser, M. Gautier-Soyer, O. Bezencenet, M. Mulazzi, M.-J. Guittet, and J.-B. Moussy, *Physical Review B* 72 (2005), p. 245423-1-245423-7.
- [133] R. L. Kurtz and V. E. Henrich, *Surface Science* 129 (1983), p. 345-354.
- [134] R. J. Lad and V. E. Henrich, *Surface Science* 193 (1988), p. 81-93.
- [135] N. G. Condon, F. M. Leibsle, A. R. Lennie, P. W. Murray, D. J. Vaughan, and G. Thornton, *Physical Review Letters* 75 (1995), p. 1961-1964.
- [136] G. Ketteler, W. Weiss, and W. Ranke, *Surface Review and Letters* 8 (2001), p. 661-683
- [137] C. H. Lanier, A. N. Chiaramonti, L. D. Marks, and K. R. Poepelmeier, *Surface Science* 603 (2009), p. 2574-2579.
- [138] M. Lübke and W. Moritz, *Journal of Physics: Condensed Matter* 21 (2009), p. 134010-1-134010-8.
- [139] R. S. Cutting, C. A. Muryn, D. J. Vaughan, and G. Thornton, *Surface Science* 602 (2008), p. 1155-1165.
- [140] T. P. Trainor, A. C. Chaka, P. J. Eng, M. Newville, J. Catalano, G. A. Waychunas, and G. E. Brown Jr., *Surface Science* 573 (2004), p. 204-224.
- [141] S. Yin, X. Ma, and D. E. Ellis, *Surface Science* 601 (2007), p. 2426-2437.
- [142] S. Yamamoto, T. Kendelewicz, J. T. Newberg, G. Ketteler, D. E. Starr, E. R. Mysak, K. J. Andersson, H. Ogasawara, H. Bluhm, M. Salmeron, G. E. Brown, Jr., and A. Nilsson, *The Journal of Physical Chemistry C* 114 (2010), p. 2256-2266.
- [143] M. Haruta, N. Yamada, T. Kobayashi, and S. Iijima, *Journal of Catalysis* 115 (1989), p. 301-309.
- [144] M. Haruta, *Gold Bulletin* 37 (2004), p. 27-36.
- [145] *Handbook of Auger Electron Spectroscopy* (1982), JOEL LTD., Tokyo, Japan.

# List of abbreviations

**AES** Auger Electron Spectroscopy

**AFM** Atomic Force Microscopy

**CAICISS** Coaxial Impact-Collision Ion Scattering Spectroscopy

**DFT** Density Function Theory

**DOS** Density Of States

**FFT** Fast Fourier Transform

**GC** Gas Chromatography

**LDOS** Local Density of States

**LEED** Low Energy Electron Diffraction

**LEIS** Low Energy Ion Scattering

**LT** Low temperature

**ML** Monolayer

**MS** Mass Spectrometry / Mass Spectrometer

**PVD** Physical Vapor Deposition

**QMS** Quadrupole Mass Spectrometer

**RGA** Residual Gas Analysis

**RHEED** Reflection High-Energy Electron Diffraction

**RT** Room temperature

**SMSI** Strong Metal-Support Interaction

**SPM** Scanning Probe Microscopy

**STM** Scanning Tunneling Microscopy

**STS** Scanning Tunneling Spectroscopy

**SXPS** Soft X-ray Photoelectron Spectroscopy

**TDS** Thermal Desorption Spectroscopy

**TEM** Transmission Electron Microscopy

**TOF** Turnover Frequency

**TPD** Temperature Programmed Desorption

**UHV** Ultra-High Vacuum

**WGS** Water Gas Shift

**XPS** X-ray Photoelectron Spectroscopy

# List of figures

Figure	Page
<b>Fig. 1.1</b> Model systems with increasing level of complexity: metal single crystal (a), oxide film (b) & oxide supported metal particles (c)	3
<b>Fig. 1.2</b> Graphical comparison of thin film growth modes: Volmer-Webber (a), Frank-van der Merwe (b) and Stransky-Krastanov (c)	4
<b>Fig. 1.3</b> Schematic drawing of a metal particle on oxide support: system in thermodynamic equilibrium [17]	5
<b>Fig. 1.4</b> Schematic drawing of a supported particle exhibiting (111) top facet and (111) / (100) side facets: structural parameters indicated	6
<b>Fig. 1.5</b> Langmuir-Hinshelwood CO oxidation reaction mechanism	9
<b>Fig. 1.6</b> Eley-Rideal CO oxidation reaction mechanism	10
<b>Fig. 1.7</b> Mars-van Krevelen CO oxidation reaction mechanism	10
<b>Fig. 1.8</b> Calculated temperature-pressure phase diagram for the iron-oxygen system [46]	11
<b>Fig. 1.9</b> Model structure of FeO(111): side view (a) & top view (b) [46]	12
<b>Fig. 1.10</b> FeO(111) / Pt(111): LEED pattern & STM images (LEED: 64 eV; STM: 100 x 100 nm <sup>2</sup> , 0.7 V, 0.4 nA (a) and 9 x 9 nm <sup>2</sup> , 1.6 V, 0.7 nA (b))	13
<b>Fig. 1.11</b> High symmetry regions within the FeO(111) / Pt(111) Moiré unit cell: "top" (circle), "fcc" (square) & "hcp" (triangle) [48]	13
<b>Fig. 1.12</b> Model structure of Fe <sub>3</sub> O <sub>4</sub> (111): side view (a) & top view (b) [46]	14

<b>Fig. 1.13</b> $\text{Fe}_3\text{O}_4(111) / \text{Pt}(111)$ : LEED pattern & STM images (LEED: 64 eV; STM: 500 x 500 nm <sup>2</sup> , 1.4 V, 0.7 nA (a) and 20 x 20 nm <sup>2</sup> , 1.4 V, 0.7 nA (b))	15
<b>Fig. 1.14</b> Model structure of $\alpha\text{-Fe}_2\text{O}_3(0001)$ : side view (a) & top view (b) [46]	16
<b>Fig. 1.15</b> $\alpha\text{-Fe}_2\text{O}_3(0001) / \text{Pt}(111)$ : LEED patterns & STM images; the “biphase”- (top) and the (1x1)- (bottom) (LEED: 64 eV; STM: 300 x 300 nm <sup>2</sup> , 1.4 V, 1.0 nA (a); 20 x 20 nm <sup>2</sup> , 1.4 V, 0.7 nA (b); 50 x 50 nm <sup>2</sup> , 1.4 V, 0.7 nA (c) and 8 x 8 nm <sup>2</sup> ; 1.4 V, 0.7 nA (d))	16
<b>Fig. 2.1</b> The main experimental UHV chamber	18
<b>Fig. 2.2</b> Single crystal mounted on the sample holder (left) & the sample stage on the main manipulator (right)	19
<b>Fig. 2.3</b> Omicron MICRO H STM (left) & measuring computer with SCALA PRO software (right)	20
<b>Fig. 2.4</b> The high pressure cell: side view (left) & the sample stage of the high pressure cell (right)	21
<b>Fig. 2.5</b> The gas line system	22
<b>Fig. 2.6</b> Schematic drawing of a 1-dimensional metal-vacuum-metal tunneling junction on the example of STM [57]	25
<b>Fig. 2.7</b> Schematic drawing of a Scanning Tunneling Microscope (STM) [61]	27
<b>Fig. 2.8</b> Typical piezo elements used in STMs: combination of three elements (left) [60] & tube geometry (right) [62]	28
<b>Fig. 2.9</b> Typical STM images: topography (left) & current (right) (samples: $\text{Fe}_3\text{O}_4(111) / \text{Pt}(111)$ (top) and $\text{Pt} / \text{Fe}_3\text{O}_4(111) / \text{Pt}(111)$ (bottom); STM: 300 x 300 nm <sup>2</sup> , 1.4 V, 0.7 nA (top) and 50 x 50 nm <sup>2</sup> , 1.4 V, 0.7 nA (bottom))	30

<b>Fig. 2.10</b> Schematic drawing of electron scattering at the crystal surface [66]	32
<b>Fig. 2.11</b> Schematic drawing of a Low Energy Electron Diffractometer (LEED) [67]	33
<b>Fig. 2.12</b> A typical LEED image (sample: $\text{Fe}_3\text{O}_4(111)$ / $\text{Pt}(111)$ ; LEED: 90 eV)	34
<b>Fig. 2.13</b> Graphical illustration of the Auger effect	35
<b>Fig. 2.14</b> A typical AES spectrum (sample: $\text{Pt}(111)$ single crystal contaminated with carbon)	36
<b>Fig. 2.15</b> Schematic drawing of a Quadrupole Mass Spectrometer (QMS) [72]	38
<b>Fig. 2.16</b> A typical TPD spectrum of CO adsorbed (sample: $\text{Pt} / \text{Fe}_3\text{O}_4(111) / \text{Pt}(111)$ flashed to 600 K)	40
<b>Fig. 2.17</b> Typical sets of first- (a) and second-order (b) desorption curves for different initial coverages [73]	41
<b>Fig. 2.18</b> Typical set of zero-order desorption curves for different initial coverages [66]	42
<b>Fig. 3.1</b> $\text{Pt}(111)$ single crystal: LEED pattern & STM image with profile line showing monatomic steps (LEED: 64 eV; STM: $1000 \times 1000 \text{ nm}^2$ , 0.7 V, 0.4 nA)	45
<b>Fig. 3.2</b> STM images of $\text{Pt} / \text{Fe}_3\text{O}_4(111)$ at different coverages: 0.08 ML (a), 0.6 ML (b), 1.0 ML (c) and 2.0 ML (d); insets show coverage dependent changes in particle height distribution; STM image of $\text{Fe}_3\text{O}_4(111)$ film as prepared is shown for comparison (STM: $500 \times 500 \text{ nm}^2$ , 1.4 V, 0.7 nA ( $\text{Fe}_3\text{O}_4$ ); $100 \times 100 \text{ nm}^2$ , 1.4 V, 0.7 nA (a); $100 \times 100 \text{ nm}^2$ , 1.0 V, 1.0 nA (b); $100 \times 100 \text{ nm}^2$ , 1.4 V, 0.7 nA (c) and $100 \times 100 \text{ nm}^2$ , 1.0 V, 0.7 nA (d))	47
<b>Fig. 3.3</b> STM images of $\text{Pt} / \text{Fe}_3\text{O}_4(111)$ at different coverages annealed at 600 K for 1 min: 0.08 ML (a), 0.6 ML (b), 1.0 ML (c) and 2.0 ML (d); profile lines show particles height; the diagram shows coverage dependent changes in particle height distribution (e); corresponding CO TPD results compared with clean $\text{Pt}(111)$ single	48



crystal are shown in (f) (STM: 50 x 50 nm<sup>2</sup>, 1.0 V, 0.6 nA (a); 1.0 V, 1.0 nA (b); 1.4 V, 0.7 nA (c) and 1.4 V, 0.7 nA (d))

**Fig. 3.4** STM images of 2.6 ML Pt / Fe<sub>3</sub>O<sub>4</sub>(111): as deposited (a), flashed to 600 K (b), annealed at 600 K for 5 min (c) and annealed at 850 K for 1 min (d); the diagram (e) shows coverage dependent changes in particle height distribution; corresponding CO TPD results are shown in (f) (STM: 100 x 100 nm<sup>2</sup>, 1.4 V, 0.7 nA (a-d)) 53

**Fig. 3.5** STM images of encapsulated Pt nanoparticles: Moiré pattern visible on the top facets (a-c); atomic resolution image showing structure with ~3 Å periodicity (d); profile line showing the Moiré corrugation amplitude (e); schematic drawing of a Pt particle encapsulated by FeO(111) (f) (STM: 80 x 80 nm<sup>2</sup>, 0.5 V, 0.6 nA (a); 20 x 20 nm<sup>2</sup>, 0.5 V, 0.6 nA (b, c) and 0.5 V, 0.7 nA (d, e)) 55

**Fig. 3.6** CO TPD results for 1.8 ML Pt / Fe<sub>3</sub>O<sub>4</sub>(111) after stepwise heating to 600, 700 and 800 K 56

**Fig. 3.7** LT CO TPD results for Pt / Fe<sub>3</sub>O<sub>4</sub>(111) as a function of Pt coverage: 0.8, 1.7 and 3.4 ML (provided by Yingna Sun, PhD thesis, FU Berlin (2010)) 57

**Fig. 3.8** STM image of Pt(111) single crystal sputtered with 1 keV Ar<sup>+</sup> ions at 300 K and annealed at 600 K for 5 min (a); corresponding CO TPD spectra (black line) compared with the spectra obtained for the sample after 0.1 ML Fe deposition (red line) (b) (STM: 100 x 100 nm<sup>2</sup>, 0.7 V, 0.4 nA) (TPD provided by Yingna Sun, PhD thesis, FU Berlin (2010)) 58

**Fig. 3.9** CO TPD results for 1.8 ML Pt / Fe<sub>3</sub>O<sub>4</sub>(111) flashed to 600 K (black line) and after additional oxidation-reduction treatment (blue line) 59

**Fig. 4.1** CO<sub>2</sub> production in CO oxidation reaction on FeO(111) / Pt(111) compared with Pt(111) single crystal: 40 mbar CO + 20 mbar O<sub>2</sub> at 450 K (GC results provided by Yingna Sun, PhD thesis, FU Berlin (2010)) 64

**Fig. 4.2** CO<sub>2</sub> production in CO oxidation reaction on FeO(111) / Pt(111) at 450 K for different CO and O<sub>2</sub> partial pressures (GC results provided by Yingna Sun, PhD 65

thesis, FU Berlin (2010))

**Fig. 4.3** Kinetics of CO<sub>2</sub> production in CO oxidation reaction on FeO(111) / Pt(111) carried at different temperatures using 40 mbar CO + 20 mbar O<sub>2</sub> (GC results provided by Yingna Sun, PhD thesis, FU Berlin (2010)) 66

**Fig. 4.4** LEED patterns of FeO(111) film before (left) and after (right) 40 mbar CO + 20 mbar O<sub>2</sub> reaction at 450 K for 120 min (LEED: 60 eV) (provided by Yingna Sun, PhD thesis, FU Berlin (2010)) 67

**Fig. 4.5** STM images: pristine FeO(111) film (a), the film after 40 mbar CO + 20 mbar O<sub>2</sub> reaction at 450 K for 120 min (b) and Pt(111) single crystal after the same reaction (c) (STM: 100 x 100 nm<sup>2</sup>, 0.7 V, 0.4 nA (a); 200 x 200 nm<sup>2</sup>, 0.8 V, 0.5 nA (b) and 200 x 200 nm<sup>2</sup>, 0.5 V, 0.3 nA (c)) 67

**Fig. 4.6** STM images of FeO(111) films: after 40 mbar CO + 20 mbar O<sub>2</sub> reaction at 450 K for 10 min (a) and after 120 min in the reaction (b) (STM: 200 x 200 nm<sup>2</sup>, 0.8 V, 0.4 nA (a) and 0.7 V, 0.4 nA (b)) 69

**Fig. 4.7** STM images of FeO(111) film after 120 min in 40 mbar CO + 20 mbar O<sub>2</sub> reaction at 450 K (a) and subsequent stepwise annealing at 500 (b), 700 (c) and 800 K (d) (STM: 500 x 500 nm<sup>2</sup>; 0.8 V, 0.5 nA (a); 0.8 V, 0.5 nA (b); 0.8 V, 0.5 nA (c) and 0.9 V, 0.6 nA (d)) 69

**Fig. 4.8** LEED patterns of FeO(111) film as prepared (a) and after exposure to 50 mbar O<sub>2</sub> at 450 K for 10 min (b); insets: zoom with enhanced contrast (LEED: 64 eV) 71

**Fig. 4.9** STM images of FeO(111) films: exposed to 20 mbar O<sub>2</sub> at 450 K for 10 min (a) and exposed to 2 mbar O<sub>2</sub> at 300 K for 5 h (b); insets: zoom of the structures; profile lines show surface corrugation amplitudes (c, d) (STM: 100 x 100 nm<sup>2</sup>, 1.0 V, 0.7 nA (a) and 50 x 50 nm<sup>2</sup>, 0.25 V, 0.3 nA (b)) ((b) provided by Shamil Shaikhutdinov) 72

**Fig. 4.10** STM images of FeO(111) films: exposed to 14 mbar O<sub>2</sub> at 450 K for 10 min (a, c) and 0.5 mbar O<sub>2</sub> at 350 K for 10 min where both unreconstructed and reconstructed regions showing ( $\sqrt{3}\times\sqrt{3}$ )R30° structure are resolved on the same 73

image (b) (STM: 50 x 50 nm<sup>2</sup>, 0.25 V, 0.7 nA (a); 50 x 50 nm<sup>2</sup>, 1.0 V, 0.7 nA, differentiated contrast (b) and 10 x 10 nm<sup>2</sup>, 0.1 V, 0.7 nA (c))

**Fig. 4.11** STM image (a) and LEED pattern (b) of FeO(111) film exposed to 10 mbar O<sub>2</sub> at 700 K for 10 min (LEED: 64 eV; STM: 100 x 100 nm<sup>2</sup>, 1.0 V, 0.7 nA) 74

**Fig. 4.12** TDS of O<sub>2</sub> (32 amu signal): decomposition of pristine FeO(111) film (dashed line) and O-rich superstructure film formed upon FeO(111) exposure to 20 mbar O<sub>2</sub> at 450 K (solid line) (provided by Yingna Sun, PhD thesis, FU Berlin (2010)) 75

**Fig. 4.13** Calculated enthalpy profile for the interaction of O<sub>2</sub> with FeO(111) film on Pt(111) (Fe blue, O red, Pt grey) (provided by Livia Giordano, Jacek Goniakowski and Gianfranco Pacchioni) 76

**Fig. 4.14** Phase diagrams for FeO<sub>x</sub> films in three high symmetry regions of the FeO(111) Moiré unit cell as a function of oxygen chemical potential  $\mu_{\text{O}}$  (provided by Livia Giordano, Jacek Goniakowski and Gianfranco Pacchioni) 77

**Fig. 4.15** Energetically favorable quasi-degenerate structures of FeO<sub>2</sub> trilayer: the “planar” (a) and the “buckled” structure (b) (provided by Livia Giordano, Jacek Goniakowski and Gianfranco Pacchioni) 79

**Fig. 4.16** Comparison of simulated STM images for “planar” (a) and “buckled” (b) structures with experimentally obtained image (c) (simulated STM images: 25 x 25 nm<sup>2</sup>, 1.0 V, electron charge isodensity =  $1 \times 10^{-5} \text{ e}/\text{\AA}^3$  (a, b); STM: 25 x 25 nm<sup>2</sup>, 1.0 V, 0.7 nA (c)) (a & b provided by Livia Giordano, Jacek Goniakowski and Gianfranco Pacchioni) 81

**Fig. 4.17** Calculated enthalpy profile for the CO+FeO<sub>2</sub>/Pt→CO<sub>2</sub>+FeO<sub>2</sub>/Pt reaction (Fe blue, O red, C yellow, Pt grey) (provided by Livia Giordano, Jacek Goniakowski and Gianfranco Pacchioni) 82

**Fig. 4.18** Schematic representation of the reaction pathways for CO interaction with O-rich film (top) and O<sub>2</sub> interaction with oxygen vacancy in the O-rich film (bottom) 83

- Fig. 4.19** STM images and LEED patterns of FeO(111) film: after 50 mbar O<sub>2</sub> treatment at 450 K for 10 min (a, d), after 10 mbar CO treatment at 450 K for 10 min (b, e) and after reoxidation with 50 mbar O<sub>2</sub> at 450 K for 10 min (c, f); inset in (b) shows atomic structure within the reduced patches (STM: 100 x 100 nm<sup>2</sup>, 1.0 V, 0.7 nA (a); 100 x 100 nm<sup>2</sup>, 1.0 V, 0.7 nA (b); 1.75 x 1.75 nm<sup>2</sup>, 0.25 V; 0.7 nA (inset in b) and 100 x 100 nm<sup>2</sup>, 1.4 V, 0.7 nA (c); LEED: 64 eV) 84
- Fig. 4.20** LEED pattern and STM images of FeO(111) film exposed to millibar pressures of NO: 20 mbar at 450 K for 10 min (a), 2 mbar at 450 K for 10 min (b) and 0.7 mbar at 300 K for 1 min (c) (LEED: 64 eV; STM: 200 x 200 nm<sup>2</sup>, 1.4 V, 0.7 nA (b) and 10 x 10 nm<sup>2</sup>, 1.0 V, 0.7 nA (c)) 85
- Fig. 4.21** TDS of O<sub>2</sub> (32 amu signal): decomposition of O-rich films formed upon exposure to 20 mbar NO (top) and O<sub>2</sub> (bottom) at 300 and 450 K (solid and dashed lines respectively) (provided by Yingna Sun, PhD thesis, FU Berlin (2010)) 86
- Fig. 4.22** Kinetics of CO<sub>2</sub> production: CO + O<sub>2</sub> reaction on pristine FeO(111) film (white squares), CO + NO on FeO(111) (red circles), CO + O<sub>2</sub> on NO pre-conditioned FeO(111) (blue squares) and CO + NO on O<sub>2</sub> pre-conditioned FeO(111) (white circles) (provided by Yingna Sun, PhD thesis, FU Berlin 2010 and Yulia Martynova) 87
- Fig. 4.23** STM images and LEED patterns of FeO(111) film: after 20 mbar NO treatment at 450 K for 10 min (a, d), after 10 mbar CO treatment at 450 K for 10 min (b, e) and after reoxidation with 20 mbar NO at 450 K for 10 min (c, f) (STM: 100 x 100 nm<sup>2</sup>, 1.0 V, 0.7 nA (a); 100 x 100 nm<sup>2</sup>, 1.0 V, 0.7 nA (b) and 100 x 100 nm<sup>2</sup>, 1.0 V, 0.7 nA (c); LEED: 64 eV) 89
- Fig. 4.24** STM image of FeO(111) film after 50 mbar NO + 10 mbar CO reaction at 450 K for 10 min (a) compared with STM image of FeO(111) film after 20 mbar O<sub>2</sub> + 40 mbar CO at 450 K for 120 min (b) (STM: 100 x 100 nm<sup>2</sup>, 2.0 V, 0.7 nA (a) and 200 x 200 nm<sup>2</sup>, 0.7 V, 0.4 nA (b)) 89
- Fig. 4.25** Schematic representation of the reaction pathways for CO interaction with O-rich film (top) and NO interaction with oxygen vacancy in the O-rich film (bottom) 90

- Fig. 4.26** STM images of Pt / Fe<sub>3</sub>O<sub>4</sub>(111) for the Pt coverages of 0.8 ML (a, c) and 2.3 ML (b, d): annealed at 600 K for 5 min (a, b) and annealed at 850 K for 1 min (c, d) (STM: 100 x 100 nm<sup>2</sup>, 1.4 V, 1.0 nA (a) and 100 x 100 nm<sup>2</sup>, 1.4 V, 0.7 nA (b-d)) 92
- Fig. 4.27** Kinetics of CO<sub>2</sub> production in CO oxidation reaction on Pt / Fe<sub>3</sub>O<sub>4</sub>(111) for the coverages of 1.6 and 6.3 ML compared with the result for pristine Fe<sub>3</sub>O<sub>4</sub>(111) film / Pt(111) (GC results provided by Yingna Sun, PhD thesis, FU Berlin (2010)) 93
- Fig. 4.28** STM images of 2.3 ML Pt / Fe<sub>3</sub>O<sub>4</sub>(111) annealed in UHV at 850 K for 1 min (a) and subsequently exposed to 20 mbar O<sub>2</sub> at 450 K for 10 min (b-d): (c) and (d) show zoom of the Pt particle marked with circle in (b); profile line along A-B is shown in (e); schematic drawing of the transformation which occurs on the top facets of Pt particles upon O<sub>2</sub> treatment is shown in (f) (STM: 100 x 100 nm<sup>2</sup>, 1.4 V, 0.7 nA (a, b, d, d) and 50 x 50 nm<sup>2</sup>, 1.4 V, 0.7 nA, differentiated contrast (c)) 94
- Fig. 5.1** STM images of α-Fe<sub>2</sub>O<sub>3</sub>-“biphase”: large scale image showing terraces of hexagonal superstructure (a) and atomic resolution images showing periodicities of ~7.5 Å (b) and ~6.5 Å (c) (STM: 200 x 200 nm<sup>2</sup>, 1.4 V, 0.7 nA (a); 12 x 12 nm<sup>2</sup>, 1.4 V, 0.7 nA (b) and 12 x 12 nm<sup>2</sup>, 1.4 V, 0.7 nA, differentiated contrast (c)) 100
- Fig. 5.2** LEED patterns of α-Fe<sub>2</sub>O<sub>3</sub>-“biphase” as prepared (a) and after long-time annealing at high temperatures (> 900 K) (b) (LEED: 64 eV) 101
- Fig. 5.3** α-Fe<sub>2</sub>O<sub>3</sub>-“biphase” superstructure models and corresponding FFT images: lattices with periodicity ratio of 1:1.067 (a) and lattices with periodicity ratio 1:1 rotated by 3.75° with respect to each other (b) 102
- Fig. 5.4** STM image of ~1/28 ML Au / α-Fe<sub>2</sub>O<sub>3</sub>-“biphase” (STM: 20 x 20 nm<sup>2</sup>, 1.0 V, 0.7 nA, differentiated contrast) 102
- Fig. 5.5** STM images of α-Fe<sub>2</sub>O<sub>3</sub>-“biphase” as prepared (a) and after deposition of few monolayers of Au (b, c) (STM: 200 x 200 nm<sup>2</sup>, 1.4 V, 0.7 nA (a); 200 x 200 nm<sup>2</sup>, 2.0 V, 0.7 nA (b) and 50 x 50 nm<sup>2</sup>, 2.0 V, 0.7 nA (c)) 103
- Fig. 5.6** LEED patterns of α-Fe<sub>2</sub>O<sub>3</sub>-“biphase” film as prepared (a), exposed to 1 mbar of H<sub>2</sub>O for 10 min (b) and after subsequent heating to 1000 K (c) (LEED: 64 eV) 104

- Fig. 5.7** STM images of  $\alpha$ -Fe<sub>2</sub>O<sub>3</sub>-“biphase” film exposed to 1 mbar of H<sub>2</sub>O for 10 min and subsequently heated to 1000 K: topography (left) & current image (right) (STM: 20 x 12 nm<sup>2</sup>, 1.4 V, 0.7 nA) 105
- Fig. 5.8** AES spectrum of  $\alpha$ -Fe<sub>2</sub>O<sub>3</sub>-(1x1) film: carbon and (probably) molybdenum contamination peaks visible 106
- Fig. 5.9** LEED pattern and STM images of  $\alpha$ -Fe<sub>2</sub>O<sub>3</sub>-(1x1): extended terraces (a) and atomic resolution image showing 5 Å periodicity (b) (LEED: 64 eV; STM: 50 x 50 nm<sup>2</sup>, 1.4 V, 0.7 nA (a) and 8 x 8 nm<sup>2</sup>, 1.4 V, 0.7 nA (b)) 106
- Fig. 5.10** STM images of 6 Å Pt /  $\alpha$ -Fe<sub>2</sub>O<sub>3</sub>-(1x1): as deposited (a), after annealing at 600 K for 5 min (b) and after annealing at 850 K for 5 min (c) (STM: 100 x 100 nm<sup>2</sup>, 1.4 V, 0.7 nA) 107
- Fig. 5.11** STM image of Pt /  $\alpha$ -Fe<sub>2</sub>O<sub>3</sub>-(1x1) after high temperature annealing: atomic structure with 5-6 Å periodicity can be seen on top of one of the particles (red circle) (STM: 30 x 30 nm<sup>2</sup>, 1.4 V, 0.7 nA, differentiated contrast) 108

## **Appendix A:**

### **Curriculum Vitae (CV)**

For reasons of data protection,  
the Curriculum Vitae is not included in the online version.

## **Appendix B:**

### **List of publications & conference appearances**

#### **PUBLICATIONS**

10. M. Lewandowski, I. M. N. Groot, S. Shaikhutdinov, and H.-J. Freund, *Scanning tunneling microscopy evidence for the Mars-van Krevelen type mechanism of low temperature CO oxidation on an FeO(111) film on Pt(111)*, *Catalysis Today* (2011), accepted.
  
9. Y. Lei, M. Lewandowski, Y.-N. Sun, Y. Fujimori, Y. Martynova, I. M. N. Groot, R. Meyer, L. Giordano, G. Pacchioni, J. Goniakowski, C. Noguera, S. Shaikhutdinov, and H.-J. Freund, *CO + NO vs CO + O<sub>2</sub> reaction on monolayer FeO(111) films on Pt(111)*, *ChemCatChem* 3 (2011), p. 671-674.
  
8. M. Lewandowski, Y.-N. Sun, Z.-H. Qin, S. Shaikhutdinov, and H.-J. Freund, *Promotional effect of metal encapsulation on reactivity of iron oxide supported Pt catalysts*, *Applied Catalysis A: General* 391 (2011), p. 407-410.
  
7. L. Giordano, M. Lewandowski, I. M. N. Groot, Y.-N. Sun, J. Goniakowski, C. Noguera, S. Shaikhutdinov, G. Pacchioni, and H.-J. Freund, *Oxygen-induced Transformations of a FeO(111) Film on Pt(111): A Combined DFT and STM Study*, *Journal of Physical Chemistry C* 114 (2010), p. 21504-21509.
  
6. Y.-N. Sun, L. Giordano, J. Goniakowski, M. Lewandowski, Z.-H. Qin, C. Noguera, S. Shaikhutdinov, G. Pacchioni, and H.-J. Freund, *The Interplay between Structure and CO Oxidation Catalysis on Metal-Supported Ultrathin Oxide Films*, *Angewandte Chemie* 122 (2010), p. 4520-4523 & *Angewandte Chemie International Edition* 49 (2010), p. 4418-4421.
  
5. Y.-N. Sun, Z.-H. Qin, M. Lewandowski, E. Carrasco, M. Sterrer, S. Shaikhutdinov, and H.-J. Freund, *Monolayer Iron Oxide Film on Platinum Promotes Low Temperature CO Oxidation*, *Journal of Catalysis* 266 (2009), p. 359-368.



4. Y.-N. Sun, Z.-H. Qin, M. Lewandowski, S. Shaikhutdinov, and H.-J. Freund, *CO Adsorption and Dissociation on Iron Oxide Supported Pt Particles*, *Surface Science* 603 (2009), p. 3099-3103.
3. Z.-H. Qin, M. Lewandowski, Y.-N. Sun, S. Shaikhutdinov, and H.-J. Freund, *Morphology and CO adsorption on platinum supported on thin Fe<sub>3</sub>O<sub>4</sub>(111) films*, *Journal of Physics: Condensed Matter* 21 (2009), p. 134019-1-134019-6.
2. Y.-N. Sun, Z.-H. Qin, M. Lewandowski, S. Kaya, S. Shaikhutdinov, and H.-J. Freund, *When an Encapsulating Oxide Layer Promotes Reaction on Noble Metals: Dewetting and in situ Formation of an "Inverted" FeO<sub>x</sub>/Pt Catalyst*, *Catalysis Letters* 126 (2008), p. 12631-12635.
1. Z.-H. Qin, M. Lewandowski, Y.-N. Sun, S. Shaikhutdinov, and H.-J. Freund, *Encapsulation of Pt Nanoparticles as a Result of Strong Metal-support Interaction with Fe<sub>3</sub>O<sub>4</sub>(111)*, *Journal of Physical Chemistry C* 112 (2008), p. 10209-10213.

## CONFERENCE APPEARANCES

### European Conference on Surface Science (ECOSS-25)

27.07-01.08.2008, Liverpool, United Kingdom

M. Lewandowski, Z.-H. Qin, Y.-N. Sun, S. Shaikhutdinov, and H.-J. Freund

*Strong Metal-Support Interaction between Pt and Fe<sub>3</sub>O<sub>4</sub>(111)* (poster)

# Erklärung

Ich versichere en Eides statt, dass ich die vorliegende Arbeit selbständig verfasst und nur die angegebenen Hilfsmittel und Quellen benutzt habe.

Poznań, 15. Juli 2011